

FINAL TECHNICAL REPORT

Asia Pacific Research Initiative for Sustainable Energy Systems

Office of Naval Research

Grant Award Number N00014-18-1-2127

March 1, 2018 through December 31, 2022



March 2023

Table of Contents

EXECUTIVE SUMMARY	3
TASK 1: OUTREACH AND PROGRAM MANAGEMENT	7
TASK 2: ELECTROCHEMICAL TECHNOLOGIES	7
2.1 Membrane-Based Energy Systems.....	7
2.2 Testing and Modeling of Battery Systems	32
TASK 3: BIORENEWABLE RESOURCES	43
3.1 Constant Volume Carbonization for Waste Management.....	43
3.2 Marine Fuels.....	57
TASK 4: RESILIENT ENERGY SYSTEMS	58
4.1 Hawai‘i Grid Reliability and Resilience	58
4.2 Grid Technology Development	62
TASK 5: ADVANCED HEAT EXCHANGER DEVELOPMENT	91
TASK 6: ENERGY EFFICIENCY	92

Final Technical Report
Asia Pacific Research Initiative for Sustainable Energy Systems
Grant Award Number N00014-18-1-2127
March 1, 2018 through December 31, 2022

EXECUTIVE SUMMARY

This report summarizes work conducted under Grant Award Number N00014-18-1-2127, the Asia Pacific Research Initiative for Sustainable Energy Systems 2017 (APRISES17), funded by the Office of Naval Research (ONR) to the Hawai‘i Natural Energy Institute (HNEI) of the University of Hawai‘i at Mānoa (UH). The work conducted under APRISES17 comprises research, develop, testing, and evaluation (RDT&E) of a variety of distributed energy systems and novel energy technologies. APRISES17 also included significant effort directed toward power grid integration using Hawai‘i as a model for applicability throughout the Pacific Region. Areas of emerging energy technologies researched under APRISES17 included electrochemical energy systems, primarily fuel cells and battery systems; biorenewable resources with activities in novel biocarbons and marine fuels; resilient energy systems including analysis for the O‘ahu grid system and development of advanced smart microgrids; and energy efficiency technologies for the build environment. Makai Ocean Engineering, under subcontract to the University of Hawai‘i, also continued their ongoing efforts to develop high-performance, low-cost heat exchangers. A brief summary of results by major task follows.

Task 1, Outreach and Program Management, supported senior faculty to provide overall program management and coordination, developed and monitored partner and subcontract agreements, and developed outreach materials for both technical and non-technical audiences. All subawardees completed the contracted work.

Task 2, Electrochemical Technologies, included RDT&E in the areas of fuel cells, water purification technology, and Li-ion batteries. Substantial progress was made in each of these areas.

Under APRISES17, HNEI continued its collaboration with the Naval Research Laboratory (NRL) supporting development of NRL proprietary fuel cell technology for unmanned aerial vehicles. During this reporting period, HNEI provided consulting and computational modeling support to NRL’s program which focused on developing new fuel cell architectures aimed targeting the Navy’s growing interest in the development of attritable, lower cost technologies.

HNEI also continued its research to develop more robust fuel cell technologies, which included studies of the behavior of PEMFC under exposure of sulfur dioxide, exploring the applicability of platinum group metal free (PGM-free) electrocatalysts, and continued efforts on developing

advanced methods for fuel cell characterization. A number of peer-review publications were produced as a result of this work. HNEI also continued efforts focused on the development of novel transition metal carbide catalysis, minimizing the acid concentration in the electrolytes for vanadium flow batteries, and a novel water purification process. During this period, HNEI filed a U.S. provisional patent for the use of fuel cell materials and designs in membrane distillers for water purification. During the period of APRISES17, significant effort was expended on the relocation of HNEI's Hawai'i Sustainable Energy Research Facility (HiSERF) from Hawaiian Electric property to the UH campus. While this move was initiated due to a lease issue, the move allowed HNEI to upgrade and modify its laboratory equipment to further its fabrication and analysis capabilities and adapt to new challenges emerging in fuel cell research and development.

In the area of Battery Energy Systems, HNEI, under this award, finalized the testing and characterization of commercial Li-ion titanate batteries under representative grid conditions, continued development of non-invasive characterization methodologies for Li-ion batteries, and began evaluating Prussian blue analogues for desalination batteries. HNEI demonstrated that its diagnosis approach of quantifying thermodynamic degradation modes is effective. This work produced eight peer-reviewed publications and results were disseminated at various conferences and workshops.

Task 3, Biorenewable Resources, continued research supporting two subtasks.

HNEI's objectives, under Subtask 3.1, were to evaluate pressurized carbonization as a tool to treat and stabilize materials representative of waste streams from contingency bases; identify pressurized carbonization reaction conditions that produce transient plastic phase solid products; and characterize the products from pressurized carbonization of waste under different test conditions. Subtask 3.2 efforts included conducting comprehensive measurements of the composition and properties of biodiesel derived from waste frying oil and investigated the impacts of antioxidant concentration on its oxidative stability. Under this award, a modified American Society of Testing and Materials (ASTM) method was employed to study the oxidation process and its impacts on fuel properties. Results are summarized and will be published in a forthcoming manuscript.

Task 4, Resilient Energy Systems, included efforts to develop tools and provide analysis of reliability in Hawai'i's energy systems as the islands continue their transition from a system that is predominantly thermal generation using fossil fuels to one with the majority of the generation from variable sources such as wind and solar. Task 4 also included a range of projects focused on the development, testing, and integration of secure microgrid technologies into larger grid systems.

In 2019-2020, the Hawaiian Electric Company (HECO) received approval from the Hawai'i Public Utilities Commission for the development of utility scale 'dispatchable' renewable energy projects on each of the islands. The projects selected each involve large scale ground-mounted

photovoltaics with approximately 4 hours of storage behind the grid-connecting inverter. HNEI, in collaboration with Telos Energy, has been engaged in developing new tools and conducting analysis to better understand the impacts of these significant change to grid operations in Hawai‘i. Efforts under this award included: 1) developing novel stochastic methodology to assess impact, risk, and reliability on high renewable grids; 2) developing a new screening tool to quantify stability risk to the grid as thermal generation is replaced with solar; 3) assessing O‘ahu’s grid near term reliability due to AES Hawai‘i’s retirement and delays in new solar and storage projects; and 4) initiating a study to determine the minimum amount of “dispatchable firm” power that the O‘ahu grid system would require to ensure reliability during extended periods of low resource (solar and wind). This work was funded under APRISES17 with a cost share from the State of Hawai‘i and has been presented to HECO, the Hawai‘i Public Utilities Commission, and various stakeholders.

Technology development activities supported under this award included the Coconut Island DC microgrid; the Advanced Real-Time Grid Energy Monitor System, a platform for grid power monitoring, analytics, and controls; a Solar Forecasting system; the demonstration of an advanced Conservation Voltage Reduction system; and the construction of HNEI’s Advanced Power Systems Laboratory.

The Coconut Island DC Microgrid Project was initiated under previous APRISES funding with the objective of demonstrating the performance and resilience of a DC microgrid designed to serve critical loads within two buildings on Coconut Island, including reliable power to critical loads during interruptions of grid supplied power, and providing the island with clean electrified transportation options powered primarily by the sun. Under APRISES17 funding, HNEI completed wiring for the entire system, an electric power flow metering system was procured and installed, installed and tested a new DC to AC inverter, commissioned inverters and charge controllers, and contracted the microgrid controller installation.

Development of the Advanced Real-Time Grid Energy Monitor System (ARGEMS) project continued and was transitioned from conceptualization and fundamental hardware and core software development to use cases and applications of the system involving analytics, modeling, and controls for in-field deployment, test, and evaluation. Under this award, HNEI added and deployed software interfaces on the ARGEMS to monitor and control additional devices, improved the volt/var control algorithms, and improved the reliability and command line interface of the system. A U.S. patent for this system was awarded in October 2021.

Due to the importance of continued solar capacity growth in the state, HNEI sought to develop methods and technologies that reduce the uncertainty of solar power generation by researching the variability to capture and characterize solar resource and the development of solar forecasting methods and technologies. Under previous APRISES funding, HNEI developed an operational solar forecasting system for the Hawaiian region. During this period, a new methodology was developed to allow for improved modeling and prediction of irradiance under clear-sky conditions,

which is a crucial first step in solar resource prediction. A peer-reviewed paper was recently published that further discusses this methodology.

HNEI also continued efforts on the demonstration of an advanced Conservation Voltage Reduction (CVR) project in Okinawa, Japan. Under previous APRISES awards, control algorithms and communications between field meters and the CVR controller were validated in a hardware-in-the-loop test platform and the on-site construction was scoped and procured. Commissioning of the voltage regulator was delayed until March 2022 due to COVID-19 restrictions. The project faced several challenges due to failures of the pQube meters that were installed to measure the voltage at each transformer. This award funded the pQube meter exchange and heater installation and commissioned, tested, and operationalized the reactive power voltage management hardware and control systems installed at the TH-415 transformer connected to the 5 kW PV system. The operation of the advanced CVR system will be evaluated under future APRISES funding.

The buildout of HNEI's Advanced Power System Laboratory (APSL), a state-of-the-art facility for conducting hands-on research on renewable energy integration in a real-time simulated grid environment, continued under APRISES17. An electrical lab safety consultant conducted a thorough safety design review of the lab's design drawings and identified potential safety risks and proposed design changes for hazard mitigation, which have been integrated into the final construction. Upon completion of the design drawings, HNEI initiated the building permit application process and received approval for its construction. As of 2022, buildout of the laboratory is 90% complete with an expected full completion occurring in 2023.

Task 5, Advanced Heat Exchanger Development, continued to support the development of high-performance thin foil heat exchangers. Under subcontract to HNEI, Makai Ocean Engineering has been developing Thin Foil Heat Exchangers (TFHX) for use in seawater-refrigerant, air-water, and water-water applications. In this report period, Makai advanced the TFHX design, reduced the TFHX fabrication time and cost; and added empirical thermal, hydraulic, and structural/mechanical performance data to the TFHX database. This work allowed for the use of new materials to expand capabilities and implement quality control processes, while adding to Makai's expertise in the fundamental principles of laser welding and further understanding of the TFHX technology. Additional detail is provided in this report and in Makai's final technical report, available on the HNEI website.

Task 6, Energy Efficiency, continued efforts to evaluate energy use and indoor air quality with natural and mechanical ventilation mechanisms. HNEI utilized the two net zero energy buildings located on the University of Hawai'i at Mānoa campus that were funded under previous APRISES awards to conduct this study. Over a multi-year period, HNEI collected data to evaluate energy consumption for operating heating, ventilation, and air conditioning (HVAC) systems "on-demand", determine the impact on carbon dioxide concentrations from HVAC operating hours, and evaluate the impact of building users' post-pandemic awareness of natural ventilation

mechanisms. It was found that proper user training to concurrently utilize natural ventilation and HVAC systems was essential in allowing CO₂ levels to remain low.

This final report describes the work that has been accomplished under each of these tasks, along with summaries of task efforts that are detailed in journal and other publications, including reports, conference proceedings, presentations, and patent applications. All works produced through these efforts are available on HNEI's website on <https://www.hnei.hawaii.edu/publications/project-reports/aprises-17/>.

TASK 1: OUTREACH AND PROGRAM MANAGEMENT

As the prime recipient of the agreement from ONR, HNEI conducts research, development, testing, and evaluation across a range of alternative and enabling energy technologies; and is responsible for development and monitoring of partner and subcontract agreements. Under this task, senior HNEI staff developed and managed partner and subcontract agreements and coordinated development of outreach materials for both technical and non-technical audiences. Senior staff also engaged directly with other DOD organizations, such as the Navy Facilities Engineering Command (NAVFAC) to assess energy needs of bases in the Asia Pacific region in an effort to continue to build these partnerships, with a focus on near-term opportunities for application of emerging energy technologies into Hawai'i bases and elsewhere in the Asia Pacific region. Details of the various partner, subcontract, and outreach activities are included in the relevant task summaries below.

TASK 2: ELECTROCHEMICAL TECHNOLOGIES

Task 2 comprises two subtasks that included the development and testing of membrane-based energy systems, primarily fuel cells, and the evaluation and modeling of Li-ion batteries and battery systems. Each of these subtasks are described in more detail below.

2.1 Membrane-Based Energy Systems

Research in the area of membrane-based energy systems included continued support of the Naval Research's fuel cell technology development program for unmanned aerial vehicles; research to advance the design of proton exchange membrane fuel cell systems with materials tolerant to harsh environments; and development of low cost and durable transition metal carbide catalysts

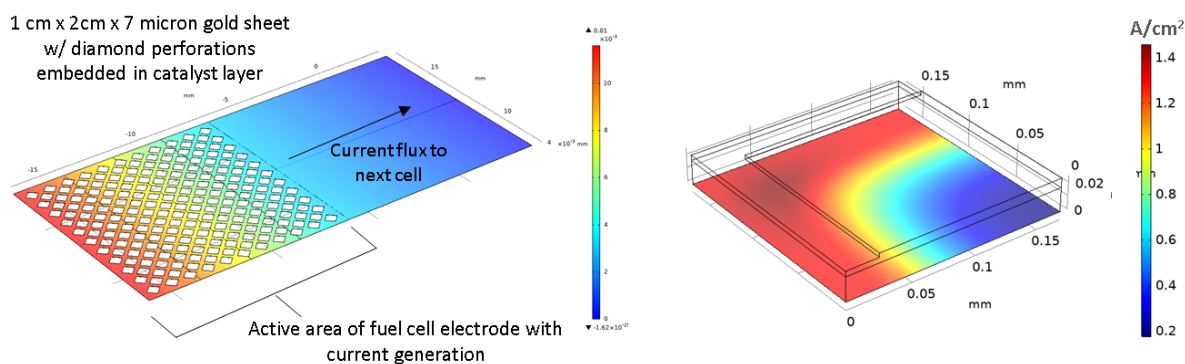
applicable to fuel cells, water electrolyzers, and vanadium redox flow batteries. A project to demonstrate the potential to improve the energy density, durability, and safety of the vanadium flow battery by minimizing the acid concentration in the electrolytes was also explored while studies to demonstrate the use of fuel cell materials for water purification and desalination was conducted. Additionally, significant time was spent on the relocation and upgrades of HNEI's Hawai'i Sustainable Energy Research Facility (HiSERF).

Key accomplishment and details of the work conducted in each of these areas are described below. Associated patents, publications, and presentations are referenced at the end of this section.

NRL Support

Under prior APRISES awards, HNEI has provided consultations, modeling, testing, and analysis in support of Naval Research Laboratory's (NRL) fuel cell technology development for unmanned aerial vehicles. With the HiSERF relocation (discussed in further detail later in this subtask) taking up significant time and manpower, under this award, HNEI provided only limited consulting and computational modeling support to NRL's current fuel cell development program. NRL's fuel cell program is now focused on producing new fuel cell architectures aimed at reducing overall system costs targeting the Navy's growing interest in the development of attritable technologies. Without testing capabilities, HNEI focused on analyzing the impact of metallic resistance and proton conductivity of various 3-d PEM fuel cell catalyst layer architectures being explored as embedded current collectors to replace the need for bipolar plates and help further optimize the overall structure, reduce the number of parts, and simplify parts registration. Representative modeling results from this effort are shown in Figure 2.1.1, which shows results looking at in-plane resistance changes based on the geometry of the current collector as well as the impact of perforation size and proton conductivity on the local current density distribution. Results were used in selecting optimal combinations of materials and geometries to evaluation in-situ at NRL.

As the work in collaboration with NRL is not approved for public release, neither data or discussion of results is included in this report. For more information on the attritable fuel cell efforts of NRL, please contact Richard Stroman at richard.o.stroman.civ@us.navy.mil. HNEI will continue to support NRL's efforts to develop attritable, low-cost fuel cell technologies under a separate award initiated in December 2022.



Example: voltage drop due to in-plane resistance changes based on geometry of embedded current collectors

Example: impact of perforation size and proton conductivity on the local current density distribution within the catalyst and gas diffusion layer

Figure 2.1.1. Sample results from modeling efforts using COMSOL 5.0 Multiphysics in support of NRL's attritable fuel cell program.

Membrane-Based Energy Technology

To better understand the limits of the current proton exchange membrane fuel cell (PEMFC) technology employing platinum-based electrocatalysts and help identify approaches for fuel cell systems and materials tolerant to harsh environments, HNEI studied behavior of low-Pt loaded PEMFC under exposure of sulfur dioxide, explored applicability of platinum group metal free (PGM-free) electrocatalysts for fuel cells and continued development of advanced methods for fuel cell characterization.

Low-Pt PEMFCs Under SO₂ Exposure: Sulfur dioxide (SO₂) has particular importance as an airborne contaminant due to its natural (volcanic activity) and anthropogenic sources of emissions, wide range of concentrations in the environment (from 5-20 ppb to several ppm [1-2]) and detrimental impact on PEMFC performance. To overcome remaining economic constraints on the wide-scale deployment of fuel cell technology, PEMFCs require additional reduction in the cost of their production, which can be achieved through economy of scales and by decreasing platinum content in the electrodes from 0.4 to 0.1 mg Pt cm⁻² or less. However, decreases in Pt loading have been shown to reduce performance and durability. In addition to the cost impacts, better understanding of environmental limitations of low-Pt PEMFCs is critical for deployment of the technology for ONR needs.

Figure 2.1.2 shows performance of commercially available membrane electrode assemblies (MEAs) with anode/cathode catalyst loading of 0.1/0.1 mg Pt cm⁻² under SO₂ poisoning using HNEI's segmented cell system. The segmented cell system allows us to obtain locally resolved voltage and current responses from the 10 segments of HNEI's hardware. The performance of MEAs is presented as profiles of individual segment voltage and normalized current densities.

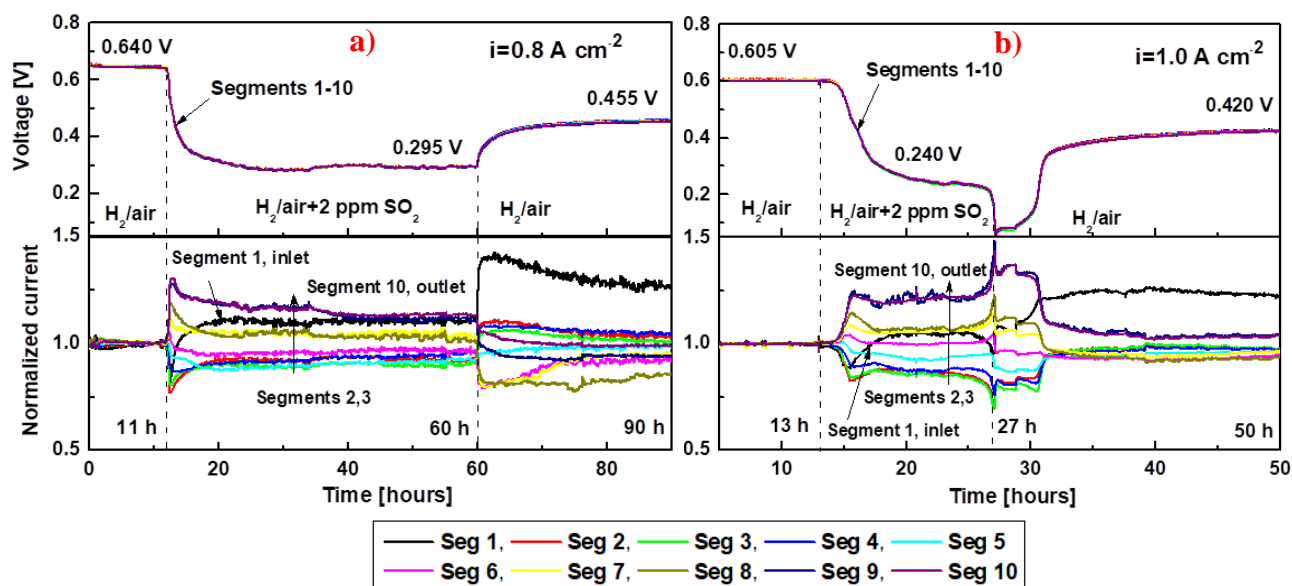


Figure 2.1.2. Cell voltage and normalized current density transients resulting from a segmented fuel cell temporarily contaminated by 2 ppm SO₂ in air for overall current densities of 0.8 (a) and 1 A cm⁻² (b).

The samples were operated at constant current densities of 0.8 and 1.0 A cm⁻² and were exposed to 2 ppm SO₂ in air stream. The obtained results demonstrate that SO₂ contamination led to significant voltage loss of 345 mV at 0.8 A cm⁻² (Figure 2.1.2a). Operating of the cell at 1.0 A cm⁻² caused first voltage loss from 0.605 V to 0.240 V and a further drastic voltage decrease below 0.1 V. Operation of the MEAs with pure air after contamination or self-recovery did not restore the initial performance due to formation of zero-valent sulfur on Pt surface and the performance difference was found to be ~185 mV for both operating currents.

The found performance was attributed to electrochemical properties of SO₂ and reactions taking place at the cathode. Our results and published literature suggested that at the beginning of poisoning, SO₂ adsorbed on the Pt surface, forming several types of Pt-SO₂ binding structures, which caused a decrease in the available electrochemical area (ECA) required for oxygen reduction [3] and a cell voltage loss. The adsorbed SO₂ species can be reduced to zero-valent sulfur at a low potential of 0.05-0.5 V or oxidized to sulfate/bisulfates (SO₄²⁻/HSO₄⁻) at high potential (>0.8 V) [4-6]. The operation of the low-Pt fuel cell at the studied current densities of 0.8-1.0 A cm⁻² resulted in an initial voltage of 0.6-0.64 V (Figure 2.1.2). SO₂ adsorption at this potential range led to the formation of partially reduced SO_x species and zero-valent sulfur. These S-containing species continued blocking the Pt surface and shifted the 4-electron oxygen reduction pathway to a less efficient 2-electron mechanism with intermediate formation of H₂O₂ [3]. All of these caused a constant decrease in cell voltage, which eventually reached values where the electrochemical reduction of SO_x to S⁰ proceeded (0.59-0.2 V). The formation of reduced SO_x species and elemental sulfur was determined by XPS and CV methods, which strongly supported the proposed SO₂ transformation pathway under normal operating fuel cell conditions.

A comparison of the sample performance before and after the SO₂ exposure and a reference sample aged at the same conditions without contamination clearly showed that SO₂ resulted in additional degradation of the catalyst material. The cathode ECA drop was 37-45% compared to the reference of 16%, while performance loss was up to 100 mV. Overall, we found and determined that the performance of low-Pt PEMFCs was more sensitive and less resistant to SO₂ compared to the high-Pt cathodes [7] due to a reduced initial performance and potential-dependent SO₂ electrochemistry. Operation of such fuel cell systems strongly requires implementation of additional filtration media and constant monitoring of incoming air quality.

More detail of this work is provided in the paper by Reshetenko *et al.* (2020) (see the Publications and Presentations section at the end of this subtask).

PGM-Free PEM Fuel Cells: Commercial PEMFC systems typically utilize Pt-based catalysts for hydrogen oxidation and oxygen reduction at anode and cathode, respectively. The replacement of Pt-based oxygen reduction catalysts with PGM-free materials has the potential to lower manufacturing cost and reduce dependence on precious metals. In addition, PGM-free cathode catalysts are tolerant to the main air pollutants like NO₂ and SO₂, which compromise Pt-based PEMFC operation [8].

PGM-free catalysts consist of non-precious transition metal (Fe, Co, Mn) coordinated by nitrogen inside a matrix of graphitic carbon (Me-N-C) and can be inexpensively manufactured at scale (Figure 2.1.3). These catalysts possess high intrinsic activity for oxygen reduction measured in electrochemical half-cell configuration. However, PGM-free electrocatalysts integrated in membrane electrode assembly (MEA) demonstrated lower performance compared to Pt based fuel cells. Their performance can be improved by designing and optimizing the cathodic catalyst layer (CCL) and MEA construction such that: 1) it efficiently provides oxygen access to Fe-N_x active sites (through catalyst morphology control); 2) it removes water from the CCL (by tuning the hydrophobicity of the PGM-free catalysts and the catalyst layer structure); and 3) it increases proton conductivity (by homogeneous mixing of catalysts and ionomer). Thus, the performance can be improved by synergistic efforts of materials design, fine tuning of the electrode layer, and comprehensive electrochemical analysis.

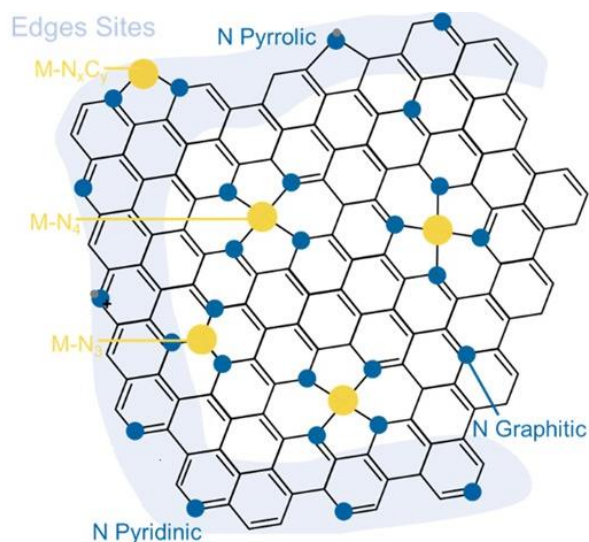


Figure 2.1.3. Schematic representation of PGM-free catalyst with $M-N_x$ active sites (Adapted from 2019, T. Asset et al., ACS Catal. 9, 7668).

In Reshетенko *et al.* (2022), several generations of PGM-free electrocatalysts were synthesized using sacrificial support method, rationally selected precursors, conditions, and treatments (Figure 2.1.4). The chosen catalyst synthesis led to formation of atomically dispersed $Fe-N_x$ moieties and increase its amount due to creation of additional defects in carbon matrix. The electrocatalysts are characterized by advanced textural properties: high surface area and large pore volume. Raman spectroscopy demonstrated that materials maintains substantial level of graphitization.

It should be noted that the PGM-free catalysts loading in MEAs is in the range of $2-4 \text{ mg}_{\text{cat}} \text{ cm}^{-2}$, which forms CCL with thickness up to $100 \text{ }\mu\text{m}$, whereas Pt-containing electrodes have catalyst content of $0.1-0.4 \text{ mg}_{\text{Pt}} \text{ cm}^{-2}$ with maximum thickness of $10-12 \text{ }\mu\text{m}$. In addition, PGM-free electrocatalysts are typically characterized by large primary catalyst particles with size higher than $1 \text{ }\mu\text{m}$, which affects their integration into the electrode structure and impacted development of three-phase boundaries and proton conductivity.

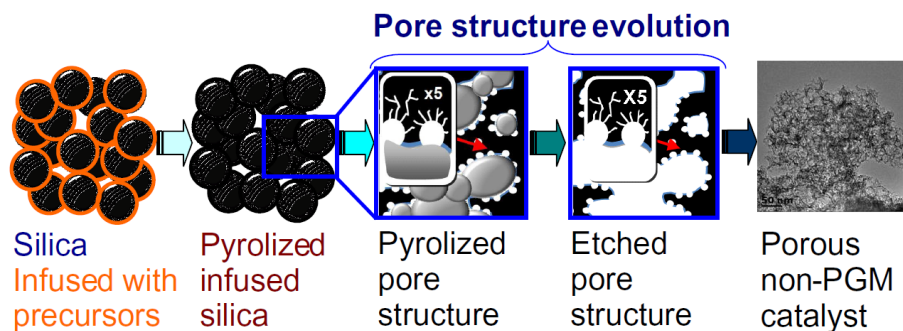


Figure 2.1.4. General schematic of used sacrificial support method for Fe-N-C catalyst synthesis.

In order to modify intrinsic catalyst properties and mitigate peroxide formation we studied impacts of Mn additives on the Fe-N-C morphology and performance. It was found that

introduction Mn in combination with variation of synthesis parameters led to formation of surface area of $1400 \text{ m}^2 \text{ g}^{-1}$ and 300-400 nm primary particles. Integration of the Fe-Mn-N-C catalysts into the electrode structure showed that CCL consisted of grains with size from several to $20 \mu\text{m}$, which were bounded together with ionomer and developed porous network penetrating the thick CCL (Figure 2.1.5).

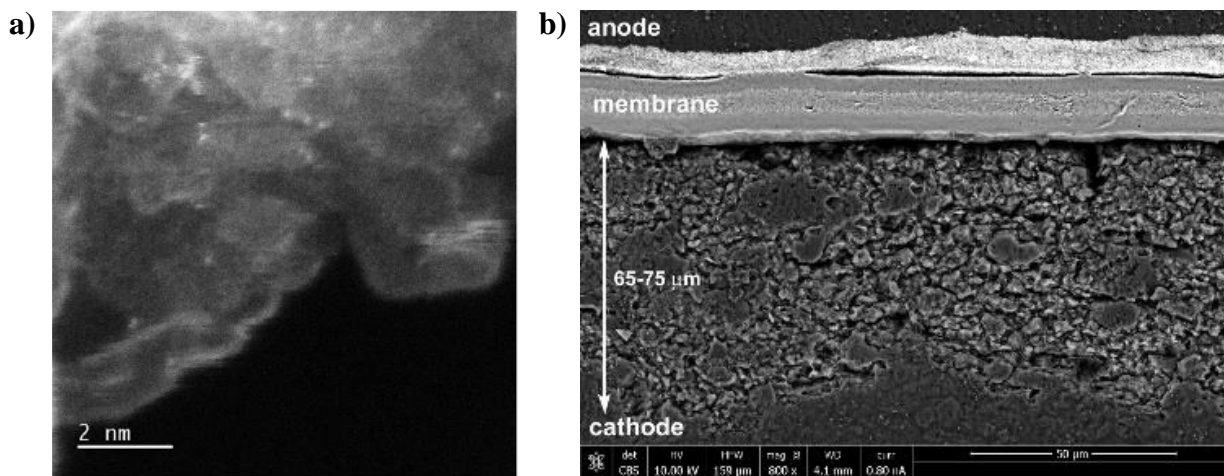


Figure 2.1.5. HRTEM (a) and SEM (b) images of Fe-Mn-N-C catalysts and MEA cross section. Atomically dispersed metal (Fe, Mn) centers are presented as bright dots at TEM images.

Using Focus Ion Beam SEM method, it was determined that Fe-Mn-N-C CCL were characterized by the highest porosity (19%) (Figure 2.1.6) which together with high hydrophobicity of the electrode improved water management and prevented flooding.

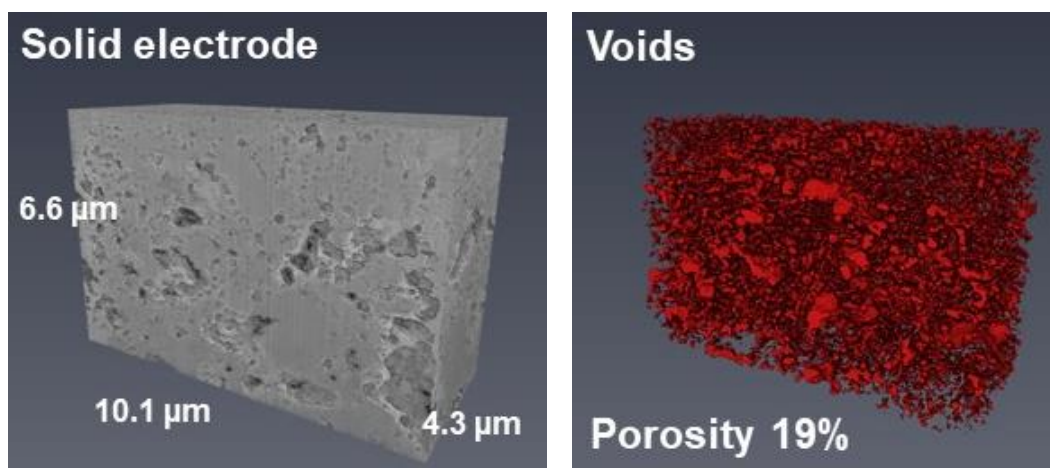


Figure 2.1.6. 3D reconstruction of solid electrode and voids for Fe-Mn-N-C electrocatalysts.

Electrochemical evaluation of the MEAs showed that the Fe-Mn-N-C catalysts revealed exceptional performance (Figure 2.1.7). Moreover, electrochemical impedance spectroscopy (EIS) analysis demonstrated that MEAs with Fe-Mn-N-C electrocatalyst were characterized by high proton conductivity and oxygen permeability which improves performance with high loaded

and thick electrodes. Based on the results of EIS modeling contribution of 2-electron oxygen reduction mechanism is negligible due excellent peroxide/radical scavenging properties of Mn.

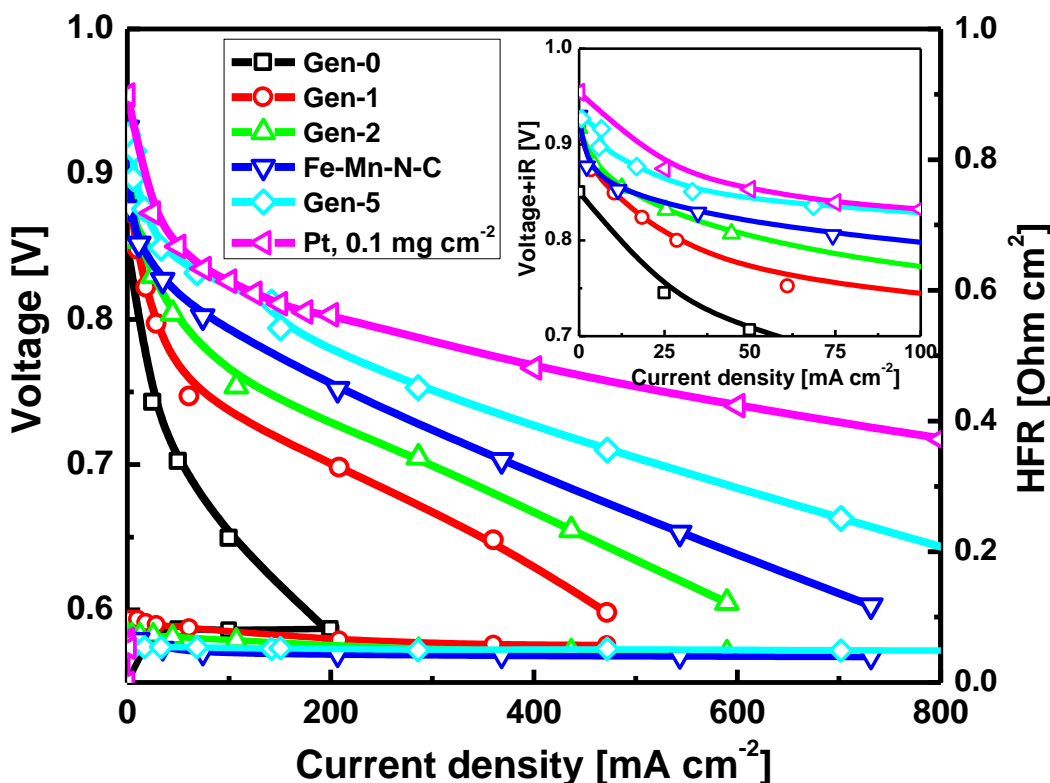


Figure 2.1.7. Polarization curves for different generation of PGM-free and Pt-based MEAs. An/Ca: H₂/O₂, 0.5 slpm, 100%RH, 150 kPa, T_{cell}=80°C.

In order to understand the performance it was evaluated more than 150 MEAs and studied impacts of membrane types, membrane thickness, ionomer EW, and its loading in the cathode electrode (30-60%); PGM-free catalyst content (0.5-6.0 mg cm⁻²) and electrode structure design. We developed testing protocols and procedures to obtain a full set of electrochemical diagnostics of the MEAs. The gained knowledge allowed us to improve the electrocatalyst and CCL design further and developed 5th generation of the material with performance approaching performance of Pt-containing MEAs at kinetic conditions (Figure 2.1.7). However, mass transport and durability of the PGM-free fuel cells still require further improvement and these are tasks for the future projects.

More detail of this work is provided in the papers by Reshetyenko *et al.* (2022), Akula *et al.* (2022), and Reshetyenko *et al.* (2019) (see the Publications and Presentations section at the end of this subtask).

Electrochemical Impedance Spectroscopy – Nafion Film Transport Properties in PEMFCs: Electrochemical impedance spectroscopy (EIS) is currently the only easily accessible tool which allows *in-situ* diagnostics of operating PEMFCs. Moreover, EIS is very sensitive method to

oxygen transport processes in a fuel cell. Recently, in Reshetenko & Kulikovsky (2019) in *RSC Advances*, we reported a model for cell impedance taking into account oxygen transport through the ionomer film. The model links in a 1d + 1d manner the oxygen diffusion equations along the cylindrical void pore and through the ionomer film surrounding the pore. In this work, the model is extended for processing of local impedance spectra, considering pore size distribution (PSD) in the electrode. To the best of our knowledge, this is the first impedance model of the operating low-Pt fuel cell considering PSD of the CCL.

We determine the ionomer film oxygen transport resistivity \mathcal{R}_N based on fitting of localized impedance spectra acquired from 10 segments of a low-Pt cell in segmented cell setup. The experimental PSD of the cathode has been approximated by pores of nine characteristic radii (Figure 2.1.8) [9]. Assuming film thickness of 10 nm, from each experimental run, we get ten local values of the product $K_H D_N$, where K_H and D_N are the Henry's constant for oxygen solubility and oxygen diffusivity in the ionomer film. Mean over the cell surface value of $K_H D_N$ and standard deviation allow us to calculate statistically significant \mathcal{R}_N for every cell current density fixed in the experiments. In the range of 100 to 800 mA cm⁻², it was determined that $\mathcal{R}_N \approx 0.4$ s cm⁻¹ is nearly independent of cell current density (Figure 2.1.9).

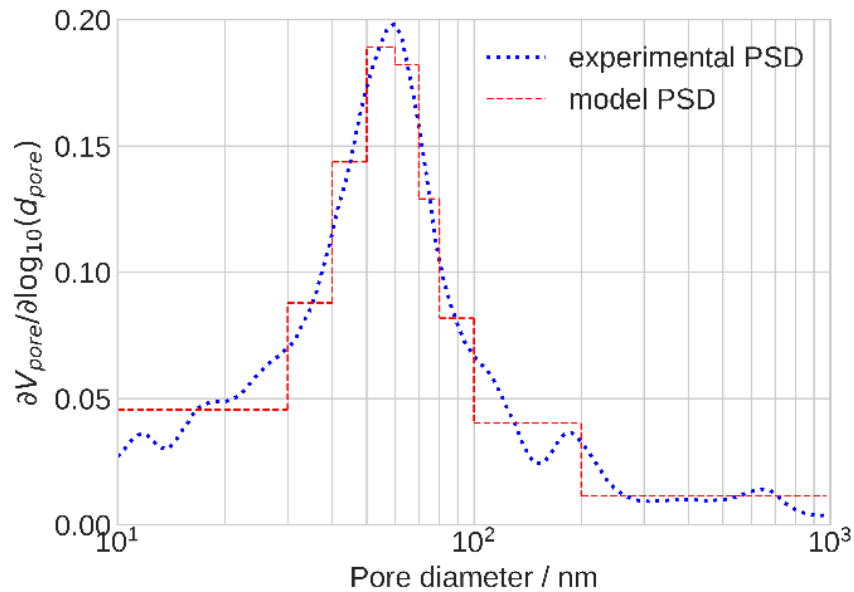


Figure 2.1.8. Experimental (dotted line) and approximate model (dashed line) pore size distributions in the cathode catalyst layer [Reshetenko & Kulikovsky (2019) in *RSC Advances*].

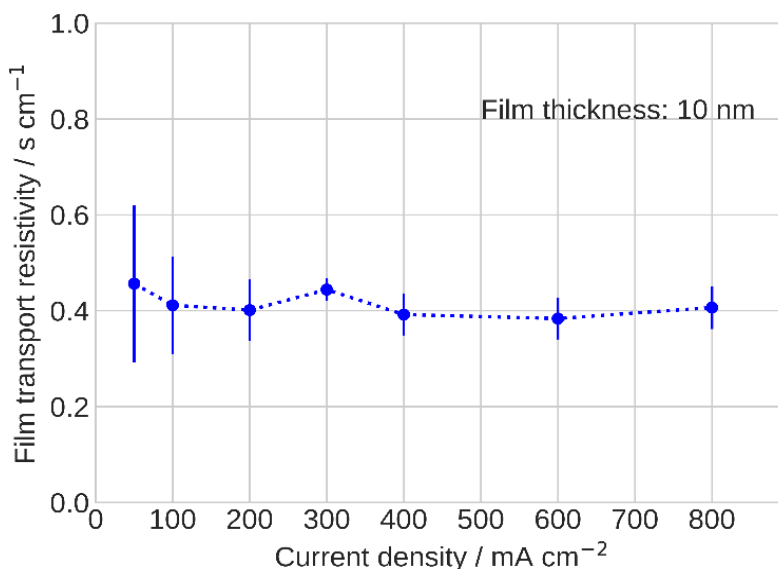


Figure 2.1.9. Ionomer film oxygen transport resistivity as function of the cell current density.

Effects of operating currents on oxygen transport resistance was firstly evaluated by D. Caulk and D. Baker using the limiting current method [10-11]. The authors reported that the oxygen transport resistance was constant for current density below 1 A cm^{-2} , after which it increased rapidly with current density until $1.6\text{-}2.0 \text{ A cm}^{-2}$, where it reached the second plateau. The observation was explained by the water production rate and its condensation to liquid at the cathode. The initial constant transport resistance corresponded to dry condition when all produced water could be removed from the cathode in vapor form. As the current density increased, water vapor pressure reached saturation and water started to condense in the CCL porous structure, leading to a growth of the transport resistance. At some point, the transport resistance reached the second plateau indicating on the maximum level of liquid saturation of the cathode electrode when the produced water could be removed mainly in liquid form. These results were confirmed by using *in-situ* neutron imaging [12] and synchrotron X-ray radiation [13] showing formation of liquid water in the CCL and linking these data with results on oxygen mass transport resistance obtained by the limiting current method.

In our case, we operated at current densities below 1.0 A cm^{-2} and we could assume that the produced water was transferred from the catalyst surface to the gas channel in vapor form and did not noticeably flood the CCL. Since initially the CCL was properly humidified and there were no conditions for flooding the ionomer film resistivity should not be affected significantly by the operating current. We may expect that a more accurate \mathcal{R}_N could be obtained from impedance measurements using a more detailed approximation of experimental PSD.

More detail of this work is provided in the papers by Reshetenko & Kulikovsky (2021), Reshetenko & Kulikovsky (2019) in *RSC Advances*, Reshetenko & Kulikovsky (2019) in *J. Electrochem.*, and Reshetenko & Kulikovsky (2022) (see the Publications and Presentations section at the end of this subtask).

Transition Metal Carbide Catalysts

Transition metal carbides (TMCs) are regarded as potential candidates to replace state-of-art platinum group metals (PGM) catalysts for electrochemical applications due to the similar d-band electronic structure to that of Pt, high abundance, and high activity. In our previous work, vanadium carbide (V_8C_7 phase) was synthesized by *in-situ* carburization of $VOSO_4$ with graphite (denoted VC_{graphite}) and XC72 (denoted VC_{XC72}) as the carbon source and support. Under this award, additional scanning electron microscopy/energy dispersive X-ray spectroscopy (SEM/EDS) was completed to determine morphology and composition. Figures 2.1.10 and 2.1.11 are SEM images of VC_{graphite} and VC_{XC72} , respectively. Cracks are present in Figure 2.1.11 SEM images due to the uneven drying of the vanadium carbide in 2-propanol suspension. As shown in Figures 2.1.10 and 2.1.11, the EDS spectra show that carbon (C) and vanadium (V) can be detected. The Si in the EDS spectra of VC_{XC72} is from the silicon wafer used as the substrate for the SEM sample. EDS mapping indicates that C and V elements are distributed uniformly on the carbon support in both the VC_{graphite} and VC_{XC72} . Based on the EDS results, VC_{graphite} is composed of 33 atom% vanadium and 67 atom% carbon, corresponding to 81.6 wt.% V_8C_7 on graphite. VC_{XC72} contains 29 atom% vanadium and 71 atom% carbon, corresponding to 76.5 wt.% V_8C_7 on Vulcan XC72.

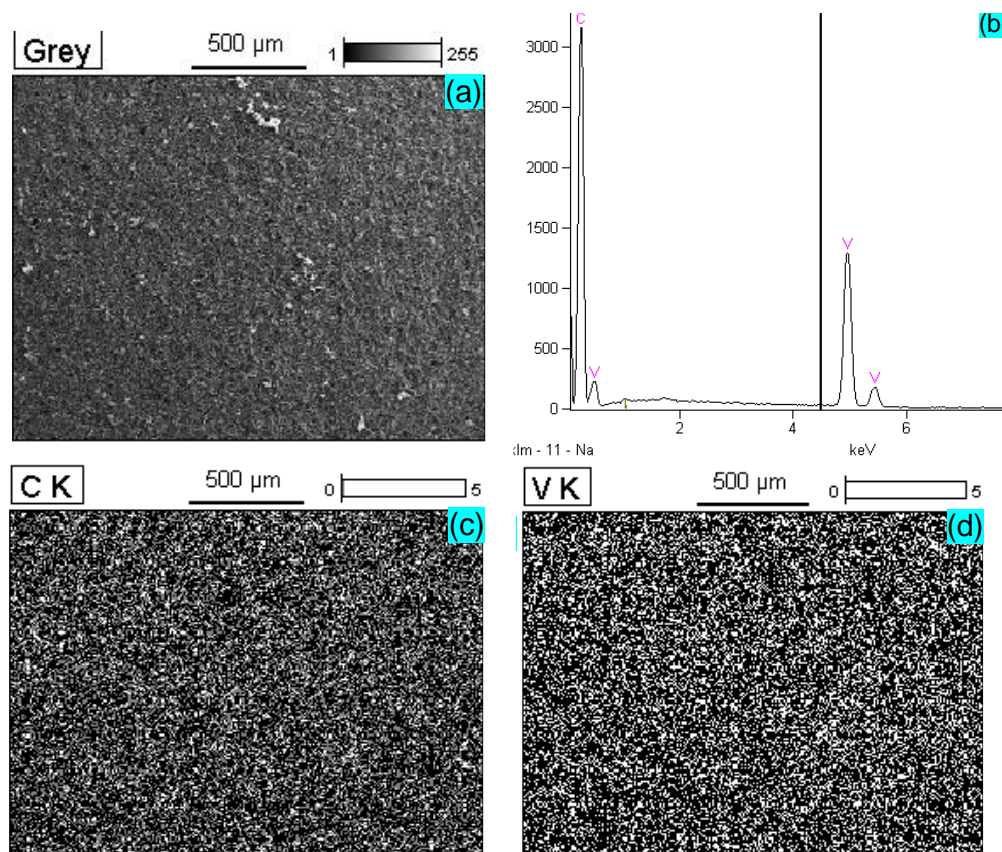


Figure 2.1.10. (a) SEM image, (b) EDS spectrum, and mapping of (c) carbon and (d) vanadium elements of VC_{graphite} .

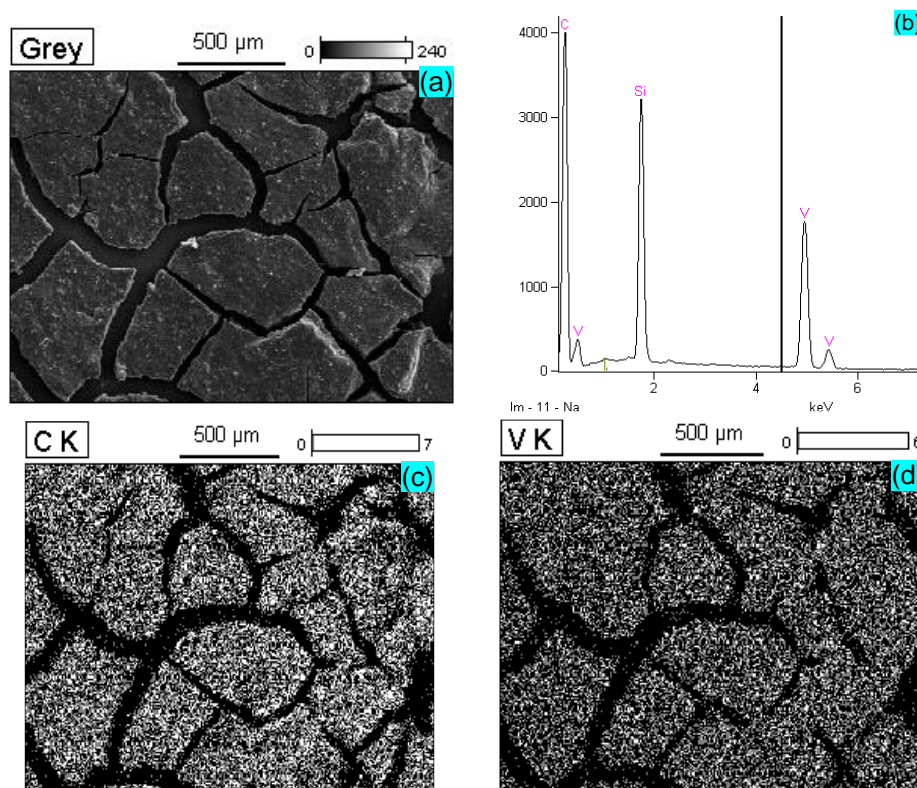


Figure 2.1.11. (a) SEM image, (b) EDS spectrum, and mapping of (c) carbon and (d) vanadium elements of VC_{x72}.

Molybdenum carbides were prepared from graphite (denoted as MoC_{graphite}) and TiC (Alfa Aesar) (denoted as MoC_{TiC}) as carbon sources and supports. As shown in Figure 2.1.12, Mo_xC_{graphite} is a mixture of MoC and molybdenum oxide phases. While MoC_{TiC} contains Mo₂C and molybdenum oxide phases. Both MoC_{graphite} and MoC_{TiC} were treated in sulfuric acid to remove the oxide.

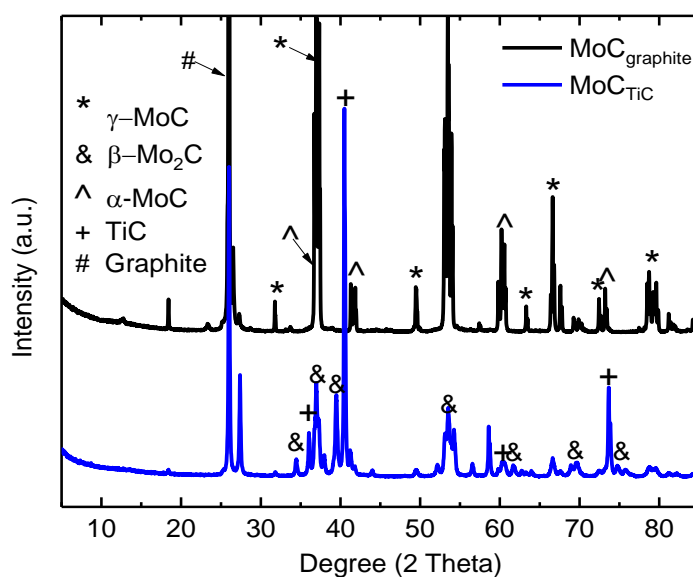


Figure 2.1.12. XRD patterns of MoC_{graphite} and MoC_{TiC}.

As shown in Figure 2.1.13, although the cathodic current remarkably increases for graphite, TiC, and MoC_{TiC}, a significant anodic current is not detected, indicating that the reversibility of these catalysts toward the V³⁺/V²⁺ redox reactions is poor. In contrast, anodic and cathodic currents substantially increase on MoC_{graphite}, indicating an improvement in catalytic activity and reversibility toward the V³⁺/V²⁺ redox reactions.

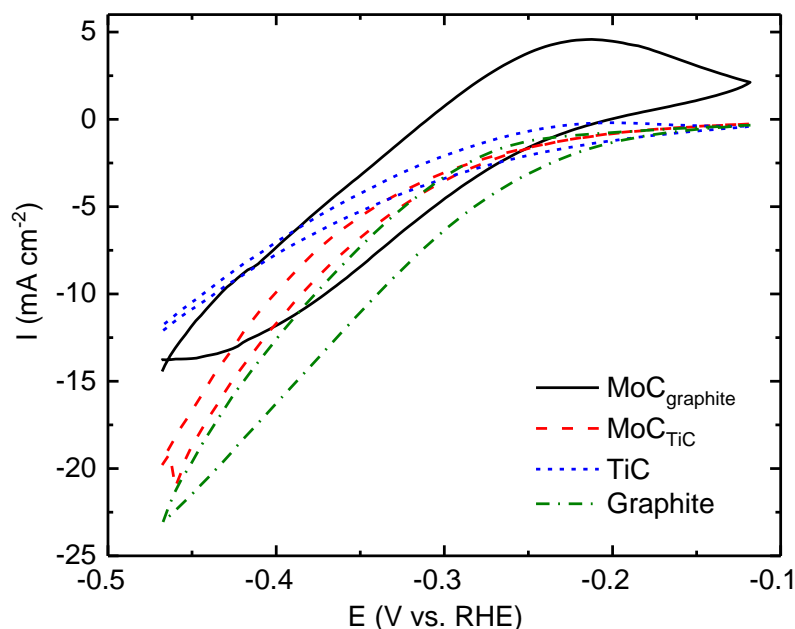


Figure 2.1.13. Cyclic voltammograms on various electrodes at 5 mV s⁻¹ in N₂-saturated 3 M H₂SO₄ + 1 M V³⁺/V²⁺ at 25°C.

Vanadium and molybdenum carbides dispersed on various supports were synthesized. Both vanadium and molybdenum carbides exhibited significantly better catalytic activities toward the negative electrode reactions than graphite, the incumbent catalyst for vanadium redox flow batteries. Synthesis and treatment process modifications are needed to get pure MoC or Mo₂C phase. The hydrogen evolution reaction will be used to conduct catalyst evaluations.

Vanadium Flow Battery with High Concentration Electrolytes

Under previous APRISES awards, vanadium flow battery (VFB) research was initiated with the objective to demonstrate the potential to improve the energy density, durability, and safety of the vanadium flow battery by minimizing the acid concentration in the electrolytes. A simple flow battery system with a 25 cm² single cell, an electrolyte composition determination method, and an in-situ pH, conductivity, and potentials monitoring system for both electrodes of VFB were established. The stabilities of all four electrolytes under low acid condition were investigated. The work indicated that all four vanadium electrolytes may be stable at low acid concentration down to mmol L⁻¹ grade. A new electrochemical reduction method was developed to produce a stable V³⁺ solution with a concentration up to 5.2 mol L⁻¹ and acid concentration low down to pH ~5.

However, with a high electrolyte concentration solution ($3 \text{ mol L}^{-1} \text{ V}$ solution without acid) and proton exchange membrane (Nafion[®]), a clogging occurred in the positive electrode of the single cell during tenth charge/discharge cycles, which resulted in a cell failure and a reversibility issue was indicated by asymmetric charge/discharge curves.

Under the APRISES17 award, electrochemical characterization was applied to study the clogging and reversibility issues. The clogging was found to be caused by the vanadium salt (valences of 5) precipitation in the very low acid environment; the reversibility issue came from the pore activity in the negative electrode and imbalance of the proton concentration (net proton migration through PEM) between both positive and negative electrolytes during the charging/discharging processes. Based those results, several modifications were made on the previous VFB single cell to attempt to solve the issues. A thermal activation method was established to treat the different type carbon and graphite felts as the electrodes for the high electrolytes and low acid concentration vanadium flow battery; the positive electrolyte was modified to start with a pH~1, $3 \text{ mol L}^{-1} \text{ V}$ solution; and the PEM was replaced by an anion exchange membrane (AEM). The single cell charge-discharge performance was investigated with the high pH negative solution and low pH positive electrolyte, which contain a certain concentration of sulfuric acid to avoid vanadium salt (valences of 5) precipitation. Different type of anion exchange membranes were applied to the vanadium flow battery. The cell performance shows the low overpotentials on for both positive and negative electrodes, which may be benefited from the high electrolyte concentrations. However, the reversibility of charging/discharging processes, the electrolytes' chemical stability, and the anion conductivity and proton permeability of the anion exchange membrane, the stability of the negative electrode, and the ionic conductivity of the negative electrolyte remain as challenges for the novel vanadium flow battery system.

Future work may include development of a novel reduction method for producing the high concentration V^{3+} solution without acid and the AEM VFB system. Data analyses and additional tests are also anticipated to quantify properties for flow batteries using high vanadium concentration electrolytes including cell potentials, vanadium species solubility, electrolyte pH and ionic conductivity, and materials stability that are needed to assess changes in energy density, coulombic efficiency, and durability.

Novel Water Purification Process

Under previous APRISES awards, efforts to develop a novel water purification seawater desalination process integrating proton exchange membrane fuel cell materials and designs were initiated. The novel water purification method is based on both membrane and thermal processes by applying a selective membrane and porous media and operated below 80°C . Similar to membrane distillation (MD), hot brine/wastewater is fed in one side of the membrane and permeate comes out from another side as freshwater; the salts, particles or other undesirable molecules are blocked and flow out as concentrate or waste. Compared to MD, the novel method employs a

dense selective membrane other than porous hydrophobic membrane. Separation process is suspected subject to a specific driving force of water activity but not the vapor pressure. The benefits of the novel method include: no phase change lowers energy consumption; operation below 80°C facilitates low-grade heat utilization; selective membrane increases ions rejection rate; and simple process reduces pretreatment requirements. The energy consumption and the productivity was estimated comparing to other water purification and desalination technologies, as in Figure 2.1.14. For the preliminary experiments, a DI water was used to optimize the water flux cross the membrane with different chamber structures. With optimized parameters, the maximum water recovery of the DI water was obtained ~50 %, the fraction of inlet water transferred to the permeate side, which might be limited by the minimum pump setting, which indicates that higher recovery and efficiency may be possible.

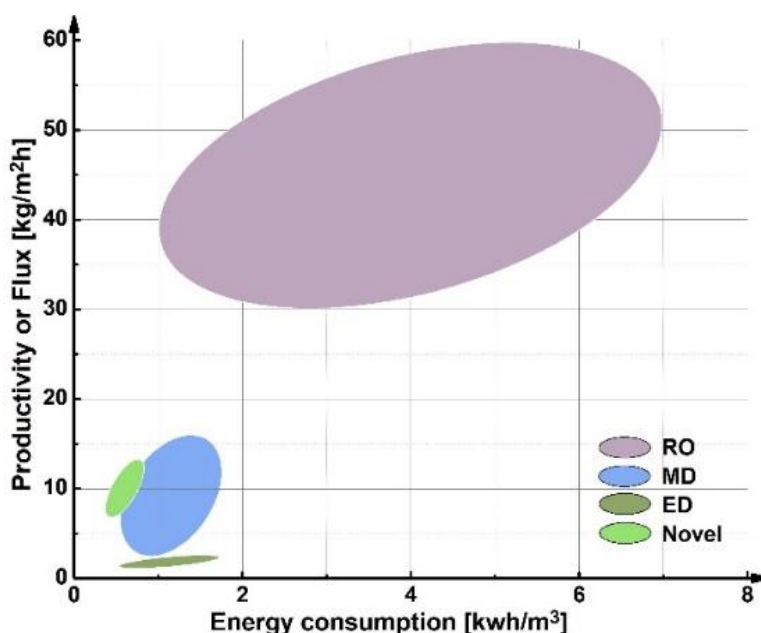


Figure 2.1.14. Comparison of water purification and desalination technologies: Reverse osmosis (RO), MD, Electrodialysis (ED), and Novel process.

Under APRISES17, the purification of a local wastewater and the desalination of local seawater were studied. The results are summarized in Figure 2.1.15, the total dissolved solid (TDS) in permeate is greatly below the freshwater standard (500 mg/l), significantly improved recovery (>30% with >99% ions rejection) and productivity (~8.6 or 9.7 kg/m²h for desalination and wastewater treatment) comparing to the state-of-the-art MD system. The best seawater and wastewater results showed a relatively stable water productivity above 8 L h⁻¹ m⁻² over several hours. The seawater sodium chloride concentration was reduced by more than 99% in almost all cases.

A United States provisional patent was filed for the use of fuel cell materials and designs in membrane distillers for water purification (additional information provided at the end of this

subtask). Based on the results, a proposal was submitted to a federal funding agency (Department of the Interior) and another proposal was submitted the Solar Desalination Prize (Department of Energy).

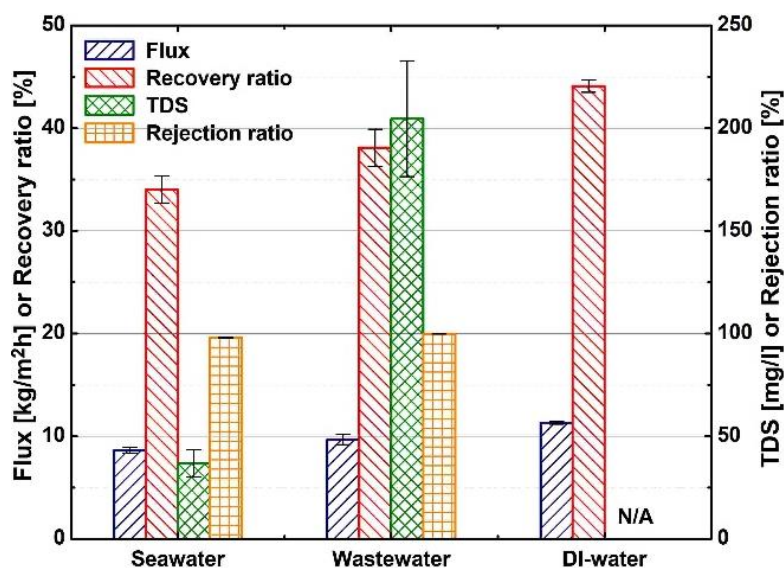


Figure 2.1.15. Purification performance of the novel method.

Under future APRISES funding, a passive system, sub-scale prototype will be designed and constructed to assess viability, gain operational knowledge to optimize design parameters. The design will rely on solar radiation to create the necessary and relatively small temperature gradient and drive water transport through the cell. The performance of the lab-scale prototype will be investigated with a low-grade heat or solar radiation; the components will be optimized for better performance and efficiency.

HiSERF Relocation

The Hawai‘i Sustainable Energy Research Facility (HiSERF), formerly the Hawai‘i Fuel Cell Test Facility, opened in 2003 on the Hawaiian Electric Company’s (HECO) main property in downtown Honolulu. The lease agreement provided over 4,500 sq. ft. of warehouse space for both office cubicles and lab operations, 4,000 sq. ft. parking lot space for supporting equipment and parking spaces, and 550 kW of available power. In February 2020, HECO abruptly ended our lease agreement. Although various negotiations were held to alter the lease agreement, HECO would not compromise and HNEI was forced to evict the premises by August 2020, in the middle of the pandemic. With campuses shutdown and new lab space not identified due to the slowdown, much of the equipment was moved into storage on the University’s campus. This included the entirety of the fuel cell testing capacity, and the majority of the standard sized cell and full pack battery testing capacity at HNEI. Throughout late 2020 and into 2021, HNEI worked with the University’s Space Committee to identify possible sites for relocation. Through a series of compromises and good timing with various retirements and subsequent lab closures, HNEI was able to secure three

new lab spaces for the Fuel Cell Systems Laboratory and the battery testing equipment was aggregated into the PakaLi Battery Laboratory's existing space. Table 2.1.1 lists the space allocation to re-establish HiSERF's fuel cell and battery testing capacity on the UH Mānoa campus.

Table 2.1.1. UH Mānoa space allocation for HiSERF relocation.

	Bldg./Room	Description	Size [sq. ft]	Space Allocation	Power [kW]
Fuel Cell Systems Laboratory	POST 06	<i>Materials Development</i> Catalysts and electrolyte materials synthesis and characterization	450	New	36 ^a
	HIG 416	<i>Cell Testing and Diagnostics</i> Fuel cell testing and advanced diagnostics development including multi-cell impedance, segmented electrode systems, and HIL/simulation based testing	750	New	77 ^b
	POST 20	<i>Cell, Stacks, and Systems</i> Fuel cell testing, stack and system evaluation, and membrane electrode assembly fabrication	1000	New	154 ^a
PakaLi Battery Laboratory	HIG 415A	Single cell and pack battery testing laboratory	450	Existing	205 ^b

a – existing power available

b – upgraded power

With the move back to campus, researchers housed at HiSERF were allocated new office space and with UH Facilities now providing HVAC, electrical, and other facility support, all of which took up significant space at HiSERF, HNEI was able to acquire more active lab space than was utilized on the HECO property. The Fuel Cell Systems Laboratory was able to acquire over 2,200 sq. ft. of new lab space, with the operations split into three labs. The 150 sq. ft. battery test room at HiSERF is combined into an existing 450 sq. ft lab space with smaller scale battery test equipment and significant ventilation and power upgrades are underway to improve operations and safety, having brought all battery testing into one location.

In 2021, HNEI began working with University of Hawai'i's Facility Maintenance Office to re-establish the infrastructure, testing, and diagnostic capabilities at the three new fuel cell laboratories and battery test room. This included HVAC, electrical, safety reviews, and contracting work to complete the necessary alterations to resume operations. By the end of 2022, HNEI had made significant progress in re-establishing the infrastructure, testing, and diagnostic

capabilities at the three new fuel cell laboratories with two of three labs operational having passed all safety requirements of the university. The 750 sq. ft. materials development lab is fully operational, while the 450 sq ft. cell testing and diagnostics lab is partially operational with one of three test stands running. The 1,000 sq. ft. cell, stack, and testing lab has completed nearly all infrastructure and equipment installation, but is awaiting a power upgrade before the test stations and gas supply infrastructure can be initialized. As of publishing this report, the final mechanical and electrical drawings for POST 20, HIG 415A, and HIG 416, which are grouped as one repair project, are being reviewed by UH Facilities and will go directly to bid as soon as the review is completed.

This move also offered an opportunity to reassess the electrochemical power systems program to improve or upgrade our capabilities to adapt to new challenges emerging in research and development, particularly the fuel cell program, which is currently focused on the development of fuel cells for operation in harsh environments. Splitting the capabilities among three labs allowed HNEI to consolidate equipment while also upgrading capabilities at different scales of research and help organize the research workflow more logically from materials all the way to stacks. This resulted in the fuel cell catalysis and electrolyte materials development equipment, housed at both HiSERF and in shared space on campus, being consolidated into the materials development lab in POST 06. Once new promising materials are integrated into membrane electrode assemblies (MEAs) they can be passed onto the cell testing and diagnostics lab in HIG 416 for evaluation and further refinement using several advanced diagnostics developed at HNEI. Having validated and optimized operation at the cell level, designs can be scaled up for applied research which occurs in the cell, stack, and systems lab in POST 20. A review of the upgraded capabilities and other required upgrades for the labs is as follows.

Fuel Cell Systems Lab - Materials and development (POST 06): Located in the basement level of the POST building, this lab is focused on the development of catalysts and electrolyte materials synthesis. Current efforts supported under ONR funding include the synthesis of graphene supported catalysts, carbide and vanadium compound catalysts, and complex solid electrolytes for fuel cells and batteries. POST 06 did not require any new university facility support as the room already had sufficient ventilation with two fume hoods and adequate power to support the micro-scale work. A general overview of the lab space is shown in Figure 2.1.16.

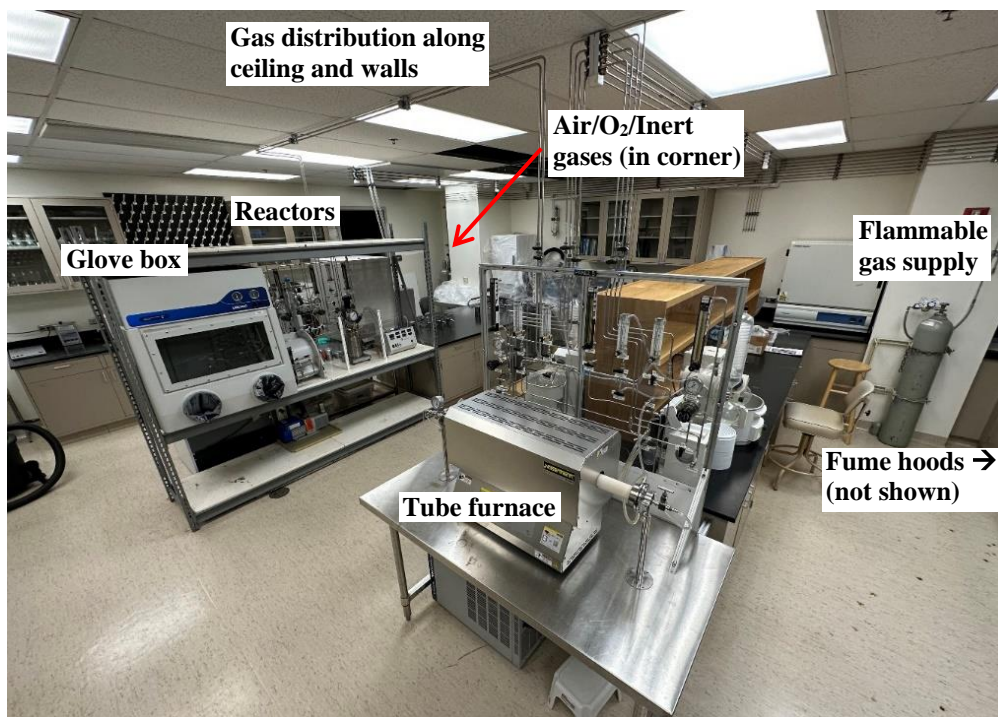


Figure 2.1.16. Overview of the POST 06 laboratory, including its equipment layout.

To improve the capabilities of the lab, several new pieces of equipment were acquired, either through new purchases or from retiring professors. These included a small glove box, high temperature and high pressure reactors, gas chromatograph, and differential scanning calorimeter as shown in Figure 2.1.17.

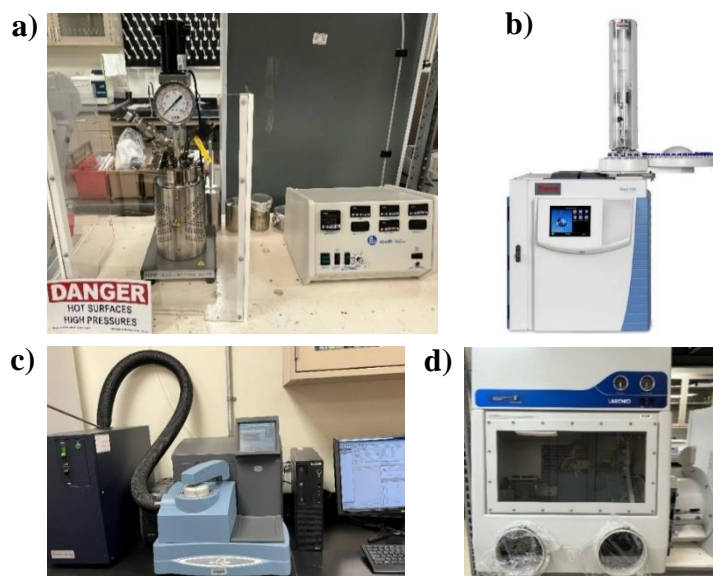


Figure 2.1.17. New materials development equipment added to POST 06 laboratory: a) Parr Stirred Reactor for high temperature (350°C) and high pressure (3000 psi) synthesis experiments, b) Thermo Scientific TRACE 310 gas chromatograph for off-gassing analysis, c) TA Instruments DSC 2000 Calorimeter, and d) vacuum glove box for materials required inert environments.

Upgrades to existing equipment were also completed under this funding to improve functionality and safety. As shown in Figure 2.1.18, a new gas delivery, exhaust, and coolant distribution panel was added to the 1300°C tube furnace to isolate the furnace from the gas sources and provide additional flexibility as the furnace serves multiple researchers. Additionally, one of the fume hoods was also outfitted with a custom gas delivery panel and additional safety measures to support the rotating ring disc electrode system used in the fume hood which is used to test new catalysts in various electrolytic environments.

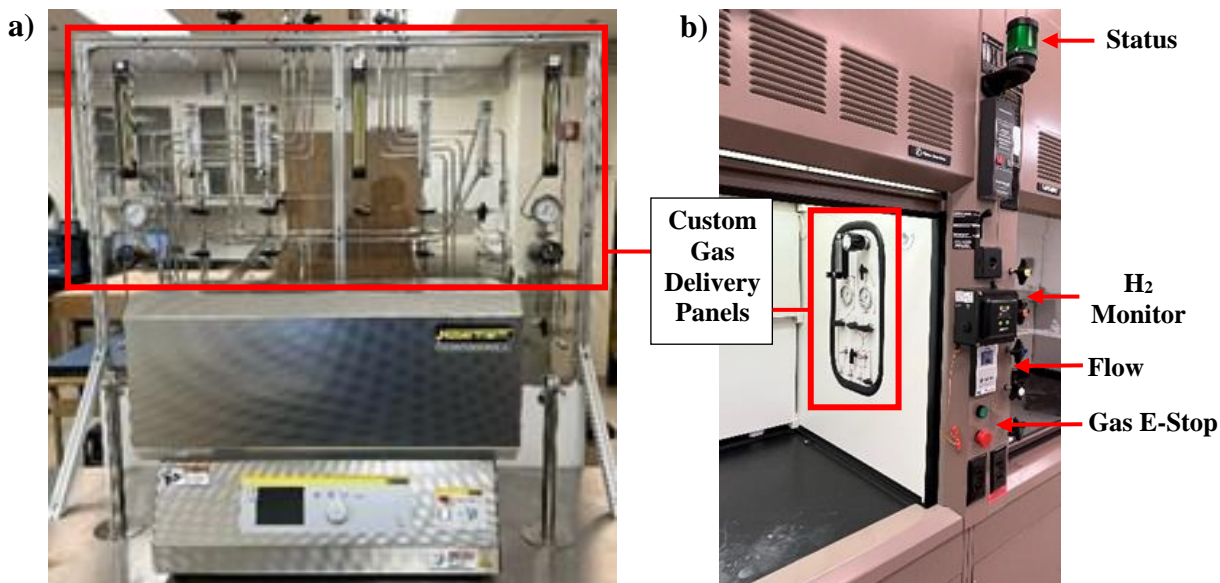


Figure 2.1.18. Customizations and upgrades to existing equipment: a) new gas delivery, exhaust, and coolant supply panel for the 1300°C tube furnace and b) upgraded fume hood with new integrated gas delivery panel for catalyst evaluations with improved safety features.

Fuel Cell Systems Lab - Cell testing and diagnostics (HIG 416): Located on the top floor of the HIG building adjacent to the bioprocessing and battery test labs, this lab is focused on the development of advanced diagnostic methods including multi-cell, simultaneous electrochemical impedance spectroscopy (EIS) with distribution of relaxation time (DRT) analysis, segmented electrode test cells and data acquisition systems, and hardware-in-the-loop/simulation driven testing capabilities. While this lab is primarily focused on diagnosing and assessing emerging materials in single cells, small stacks can also be tested. Three test stations are housed in the laboratory, as shown in Figure 2.1.19. To utilize the space, several upgrades were required including the replacement and upgrade of the existing electrical panels increasing available power from 30 kW to 77 kW, upgrading the ventilation system to support both the test stand exhaust, and a new fume hood added to the laboratory. The gas supply is primarily cylinder based except for the air supply from the building compressors where a gas cleanup system was added to provide zero-grade air to the fuel cell test stations.

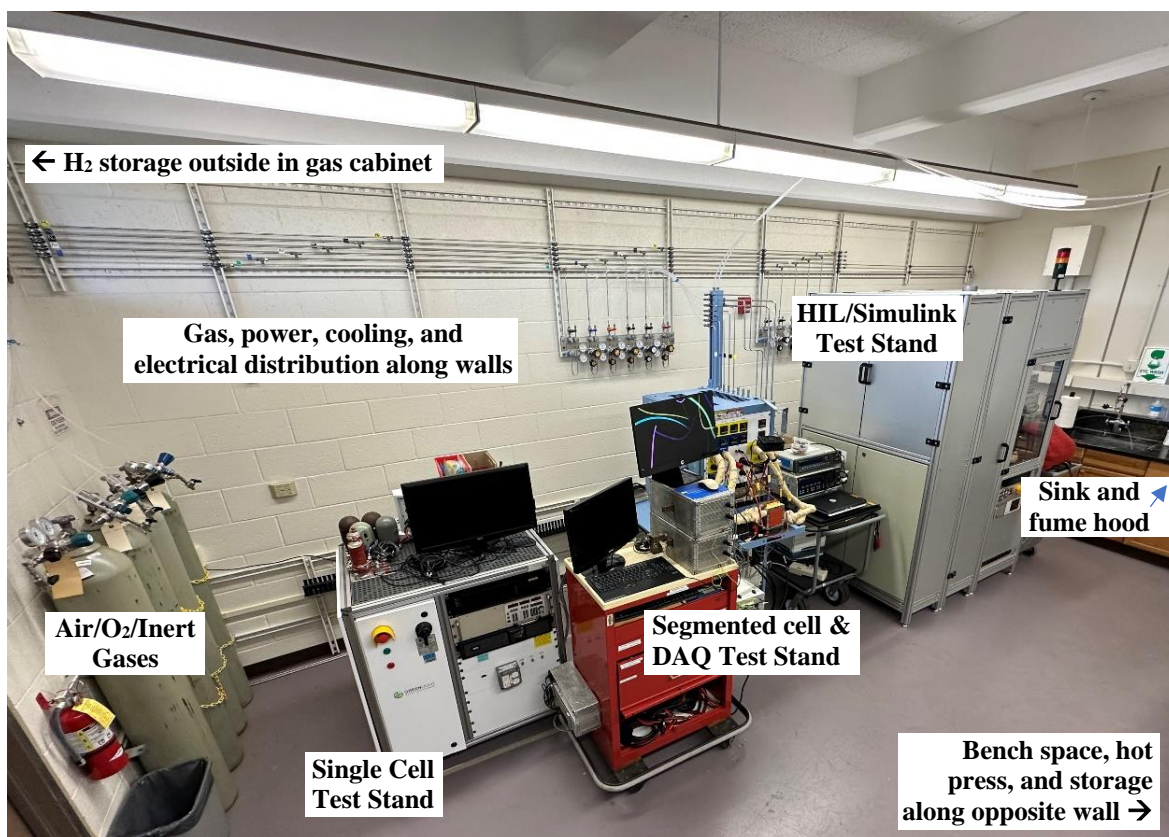


Figure 2.1.19. Test stand row and general layout of the HIG 416 laboratory.

Fuel Cell Systems Lab - Cell, Stack, and Systems (POST 20): Also located in the basement of the POST building and located two hallways down from POST 06 is the cell, stack, and systems lab. This lab houses the three United Technologies (UTC) fuel cell stands that were originally installed at HiSERF in 2003, although various upgrades were made throughout the years. A full rebuild of the mechanical process side of the stations was performed as part of the relocation. As each station had a high number of data acquisition channels available, each of the three stations (Figure 2.1.20a) has been upgraded or is in the process of being upgraded to operate two test articles each, doubling the capacity of these stations and bring the total fuel cell testing capacity to nine test articles (see Table 2.1.2) vs. seven at HiSERF. Additionally, as the HNEI/ONR fuel cells for harsh environments program is shifting towards HTPEM fuel cells, upgrades were made to accommodate the higher operating temperatures of 140-220°C for HTPEM vs. 50-90°C for LTPEM. To allow for both dual operation and advanced testing, new gas flow controller manifolds were built which have 17 mass flow controllers (MFC) on each station (Figure 2.1.20b); two sets of 6 are for the standard gases to run two fuel cells on each station and 5 additional channels for impurity gases used in contaminant challenges and dilutant gases for mass transport studies. To support operation of the test stations in POST 20, several pieces of supporting equipment from HiSERF were moved into the lab space including the Nel Hydrogen electrolyzer along with the oil-free scroll air compressor and cleanup system, and deionized water recirculation system. A new Parker Nitrosorce nitrogen gas generator was purchased and installed to replace

the liquid nitrogen supply which was used at HiSERF. The lab space was originally designed as a thin film lab, so there was sufficient ventilation available in the room and no additional mechanical work through UH facilities was required. New electrical work was required. Although the room has two 225, 208 3p power panels available, significant rewiring and conduit work was needed to hookup all the new equipment which required working with UH Facilities and outside contractors. The contracting work is still in progress.

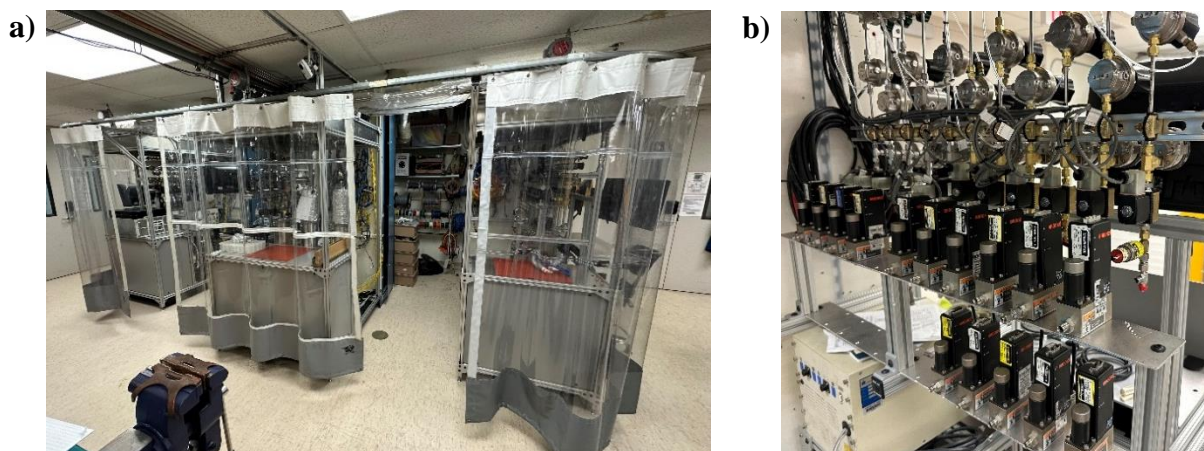


Figure 2.1.20. a) The test stand row and b) upgraded MFC racks for running two-cells per station with impurity injection and dilution gases for mass transport studies in the POST 20 laboratory.

Table 2.1.2. Fuel Cell Systems Laboratory Fuel Cell Test Stations.

Bldg./Room	Test Stand Description	Size [kW]	Cell Types
HIG 416	1. Greenlight Power G50 Station	0.8	Single cells, short stacks
	2. Segmented Electrode Station	0.5	Segmented single cells
	3. HIL Station	1.0	Single cells, small area stacks
POST 20	4. HNEI/UTC Test Station 1, Channel 1	0.3	Single cells
	5. HNEI/UTC Test Station 1, Channel 2	0.3	Single cells
	6. HNEI/UTC Test Station 2, Channel 1	0.8	Single cells, short stacks
	7. HNEI/UTC Test Station 2, Channel 2	2.5	Stacks
	8. HNEI/UTC Test Station 3, Channel 1	0.3	Single cells
	9. HNEI/UTC Test Station 3, Channel 2	0.3	Single cells

Note: all stations highly reconfigurable for other applications, e.g. flow-batteries or electrolysis

As part of the efforts to improve the workflow and scope of HNEI's fuel cell research program, additional capabilities were added to the laboratory, primarily centered around the ability to fabricate fuel cell MEAs. A custom ultrasonic spray coating system and ventilated enclosure was designed and built based upon a design from the Naval Research Laboratory (Figure 2.1.21). Additional equipment, such as a laser cutter, hot press, drying equipment, and electrode slurry preparation equipment were also added to the lab. To support the fabrication efforts, a Keyence VK-8700 laser confocal scanning microscope was acquired from another lab as it was not in use.

This tool will be highly beneficial for evaluating surface roughness of materials for interfacial resistance studies as well as thickness measurements of various components in-house that normally requires SEM level microscopy which takes significantly longer. Typical component thicknesses of MEAs being studied under the harsh environment program are on the order of 30-50, 70-120, and 300-400 μm , as shown in the cross section schematic in Figure 2.1.22. To validate the microscope's ability to image at these levels, a 1 mil (25.4 μm) thick Kapton film was sliced and scanned. Clearly shown in Figure 2.1.22 is an SEM-like image demonstrating the sub-micrometer resolution which is more than sufficient to replace the use of SEM. Furthermore, analysis time is greatly reduced with an overall time of less than 10 minutes for mounting the piece for imaging, scanning, and completing a quick thickness check.

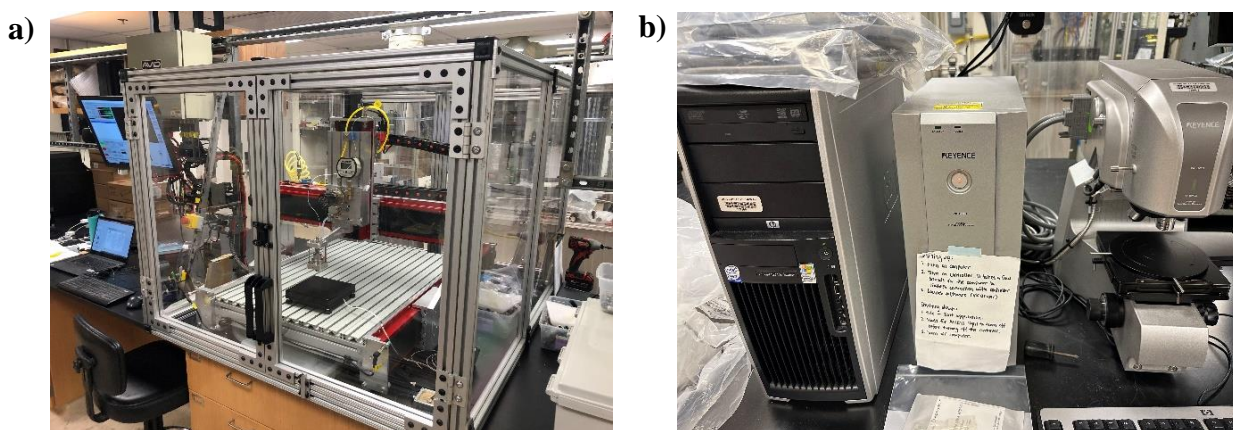


Figure 2.1.21. a) New custom ultrasonic spray coating system w/ventilated enclosure and b) newly acquired Keyence VK-8700 Laser Confocal Scanning Microscope.

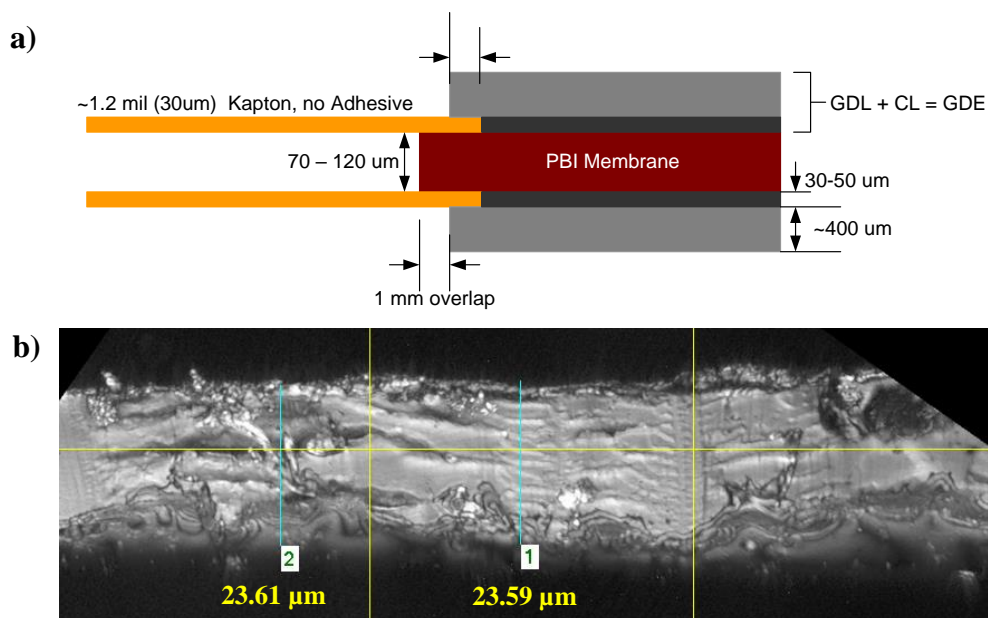


Figure 2.1.22. a) Cross section schematic of components of HTPEM MEA with approximate thickness dimensions and b) laser scanned cross section of 1 mil Kapton film.

With the upgraded lab spaces, HNEI's fuel cell program can now shift from what was primarily testing and evaluation at HiSERF, to a solutions provider with a full scale research and development program. Under future APRISES awards, HNEI will continue to support the Fuel Cells for Harsh Environments program underway. In the materials lab, work will continue on the development of durable catalysts, contaminant prevention measures, such as in-situ catalytic conversion layers, and new solid electrolyte development. In the cell diagnostics lab, efforts are underway to adapt diagnostics for proton exchange membranes to anion exchange membranes which offer unique contaminant tolerant features. Work in the cell, stack, and systems lab is now focused on the contaminant tolerant, high temperature PEM fuel cell development as part of the Harsh Environments program as well as a new project focused on cost reduction and attritability through new fuel cell architectures.

Patents

1. St-Pierre, J., Zhai, Y., & Qi, J. Novel membrane distillation process for water purification based on composites of solid ionomer membranes and porous transport media, United States provisional patent 62/940,833, November 26, 2019.

Publications and Presentations

Peer-Reviewed Publications

1. Reshetenko, T., Serov, A., Kulikovskiy, A., & Atanasov, P. (2019). Impedance spectroscopy characterization of PEM fuel cells with Fe-N-C-based cathodes. *Journal of The Electrochemical Society*, 166(10).
2. Reshetenko, T., & Kulikovskiy, A. (2019). Nafion film transport properties in a low-PT PEM fuel cell: Impedance spectroscopy study. *RSC Advances*, 9(66), 38797-38806.
3. Reshetenko, T., & Kulikovskiy, A. (2019). On the origin of high frequency impedance feature in a PEM fuel cell. *Journal of The Electrochemical Society*, 166(15).
4. Reshetenko, T., Laue, V., Krewer, U., & Artyushkova, K. (2020). Study of degradation and spatial performance of low PT-loaded proton exchange membrane fuel cells under exposure to sulfur dioxide in an oxidant stream. *Journal of Power Sources*, 458, 228032.
5. Reshetenko, T. V., & Kulikovskiy, A. (2021). Impedance spectroscopy measurements of ionomer film oxygen transport resistivity in operating low-PT PEM fuel cell. *Membranes*, 11(12), 985.
6. Reshetenko, T., Odgaard, M., Randolph, G., Ohtaki, K. K., Bradley, J. P., Zulevi, B., Lyu, X., Cullen, D. A., Jafta, C. J., Serov, A., & Kulikovskiy, A. (2022). Design of PGM-free cathodic catalyst layers for advanced PEM fuel cells. *Applied Catalysis B: Environmental*, 312, 121424.
7. Akula, S., Mooste, M., Zulevi, B., McKinney, S., Kikas, A., Piirsoo, H.-M., Rähn, M., Tamm, A., Kisand, V., Serov, A., Creel, E. B., Cullen, D. A., Neyerlin, K. C., Wang, H.,

Odgaard, M., Reshetenko, T., & Tammeveski, K. (2022). Mesoporous textured Fe-N-C electrocatalysts as highly efficient cathodes for proton exchange membrane fuel cells. *Journal of Power Sources*, 520, 230819.

8. Reshetenko, T., & Kulikovsky, A. (2022). Physics-based impedance spectroscopy characterization of operating PEM fuel cells. In J. L. Liu, T-H. Yan, and S. Bashir (Eds.) *Advanced Nanomaterials and Their Applications in Renewable Energy* (Second Edition, pp. 111-157). Elsevier Science.

Conference Proceedings and Presentations

1. Reshetenko, T., Serov, A., Kulikovsky, A., & Atanassov, P. (2019, October 13-17). *Comprehensive characterization of PGM-free PEM fuel cells using AC and DC methods*. 236th ECS Meeting, Atlanta, GA, United States.
2. Reshetenko, T. & Ben, B. L. (2019, October 13-17). *Analysis of mass transport phenomena in PEMFC cathode electrode: effects of operating conditions*. 236th ECS Meeting, Atlanta, GA, United States.
3. Qi, J., Zhai, Y., & St-Pierre, J. (2020, October 4-9). *Synthesis of Transition Metal Carbide Catalysts for Vanadium Redox Flow Batteries*. PRiME 2020 Meeting, Virtual.
4. Reshetenko, T., Ben, B. L., Laue, V., Krewer, U., & Artyushkova K. (2021, December 16-21). *Spatial low-Pt PEMFCs performance and durability under cathode exposure to common air contaminants*. PacificChem Conference, Honolulu, HI, United States.
5. Reshetenko, T., Randolph, G., Ben, B. L., & Rezantes, A. (2022, July 24-29). *Mass transport resistances in PEM fuel cell electrodes*. Gordon Research Conference, Smithfield, RI, United States.
6. Reshetenko, T., Ben, B. L., Laue, V., Krewer, U., & Artyushkova, K. (2022, September 5-7). *Operation of PEM fuel cells exposed to harsh environments*. Invited lecture, GDE symposium, Mardeburg, Germany.
7. Reshetenko, T., Ben, B. L., Laue, V., Krewer, U., & Artyushkova, K. (2023, February 7-9). *PEM fuel cells performance in real-world environmental conditions*. Hydrogen and Fuel Cell Seminar, Long Beach, CA, United States.

References

- [1] Annual summary – Hawai‘i Air quality data, 2015, https://health.hawaii.gov/cab/files/2016/12/aqbook_2015.pdf.
- [2] Sutton, A. J., Elias, T., & Navarrete, R. (1994). Volcanic gas emissions and their impact on ambient air character at Kilauea Volcano, Hawai‘i, Open-File Report 94-569. <https://digital.library.unt.edu/ark:/67531/metadc707134/>
- [3] Garsany, Y., Baturina, O. A., & Swider-Lyons, K. E. (2007). Impact of sulfur dioxide on the oxygen reduction reaction at PT/Vulcan Carbon Electrocatalysts. *Journal of The Electrochemical Society*, 154(7).

- [4] Loučka, T. (1971). Adsorption and oxidation of sulphur and of sulphur dioxide at the Platinum Electrode. *Journal of Electroanalytical Chemistry and Interfacial Electrochemistry*, 31(2), 319-332.
- [5] Contractor, A. Q., & Lal, H. (1978). The nature of species adsorbed on platinum from SO₂ Solutions. *Journal of Electroanalytical Chemistry and Interfacial Electrochemistry*, 93(2), 99-107.
- [6] Baturina, O. A., Gould, B. D., Korovina, A., Garsany, Y., Stroman, R., & Northrup, P. A. (2011). Products of SO₂ adsorption on fuel cell electrocatalysts by combination of Sulfur K-Edge Xanes and Electrochemistry. *Langmuir*, 27(24), 14930-14939.
- [7] Reshetenko, T., Laue, V., Krewer, U., & Artyushkova, K. (2019). Poisoning effects of sulfur dioxide in an air stream on spatial proton exchange membrane fuel cell performance. *Journal of Power Sources*, 438, 226949.
- [8] Reshetenko, T., Serov, A., Artyushkova, K., Matanovic, I., Stariha, S., & Atanassov, P. (2016). Tolerance of non-platinum group metals cathodes proton exchange membrane fuel cells to air contaminants. *Journal of Power Sources*, 324, 556-571.
- [9] Yu, H., Bonville, L., & Maric, R. (2018). Analysis of H₂/air polarization curves: The influence of low PT loading and fabrication process. *Journal of The Electrochemical Society*, 165(5).
- [10] Caulk, D. A., & Baker, D. R. (2010). Heat and water transport in hydrophobic diffusion media of PEM fuel cells. *Journal of The Electrochemical Society*, 157(8).
- [11] Caulk, D. A., & Baker, D. R. (2011). Modeling two-phase water transport in hydrophobic diffusion media for PEM fuel cells. *Journal of The Electrochemical Society*, 158(4).
- [12] Owejan, J. P., Trabold, T. A., & Mench, M. M. (2014). Oxygen transport resistance correlated to liquid water saturation in the gas diffusion layer of PEM fuel cells. *International Journal of Heat and Mass Transfer*, 71, 585-592.
- [13] Muirhead, D., Banerjee, R., George, M. G., Ge, N., Shrestha, P., Liu, H., Lee, J., & Bazylak, A. (2018). Liquid water saturation and oxygen transport resistance in polymer electrolyte membrane fuel cell gas diffusion layers. *Electrochimica Acta*, 274, 250-265.

2.2 Testing and Modeling of Battery Systems

The battery research conducted under the Testing and Modeling of Battery Systems subtask included three activities: 1) completion of the testing and characterization of commercial Li-ion titanate batteries under grid representative conditions, 2) continued development of non-invasive characterization methodologies for Li-ion batteries with a focus on data driven methods, and 3) the initiation of the evaluation of Prussian blue analogues for desalination batteries. Testing was conducted at HNEI's PakaLi Battery Laboratory on the University of Hawai'i at Mānoa campus. Cell performance was modeled using tools developed under previous APRISES funding. Key accomplishments and details of the work conducted were fully published or presented at

international conferences and are all summarized below. The associated eight publications and eighteen communications (presentations and posters) are referenced at the end of this section.

Battery Durability Under Power Systems Operation

Battery energy storage systems (BESS) are expected to play a crucial role in the resiliency of future electricity grids that utilize high penetrations of intermittent renewable technologies. The use of BESS still poses challenges in how to best utilize batteries to maximize performance and durability while assuring safe usage of the systems. Under this subtask, HNEI finalized the testing of single cells to generate analytic models that provided a detailed understanding of the state-of-health and safety of the battery under use. The results of the laboratory study were then compared with results gathered from the deployed system both at the battery management system and through module swapping. This task led to two peer-reviewed publications under APRISES17 (Baure & Dubarry, 2020 and Dubarry *et al.*, 2021).

In Baure & Dubarry (2020), we investigated commercial generation 2 lithium titanate batteries under conditions designed to represent the various usages associated with different modern grid applications as well as calendar aging (Figure 2.2.1). The cells exhibited remarkably low capacity loss after more than 450 days of cycle-aging testing. However, a careful analysis of the changes in their electrochemical behavior enabled the automatic quantification of the hidden degradation modes (i.e., degradation that does not induce capacity loss) and forecast their impact over a 20-year lifespan. It was shown that, for the cells tested at 35°C and at low state of charges (SOCs), capacity loss could accelerate after only six years of deployment. Under all the other conditions, if the temperature remained below 35°C, the capacity loss is limited to less than 20% capacity loss at the single cell level at the 20-year mark. These results provide confidence in the endurance of the two deployed MW BESS systems using this battery technology on the island of O‘ahu and Moloka‘i.

This study also demonstrated that the HNEI diagnosis approach consisting of quantifying the three main thermodynamic degradation modes is effective as they were affected differently by the testing conditions and that their individual quantification was essential for accurate prognoses, automated or not.

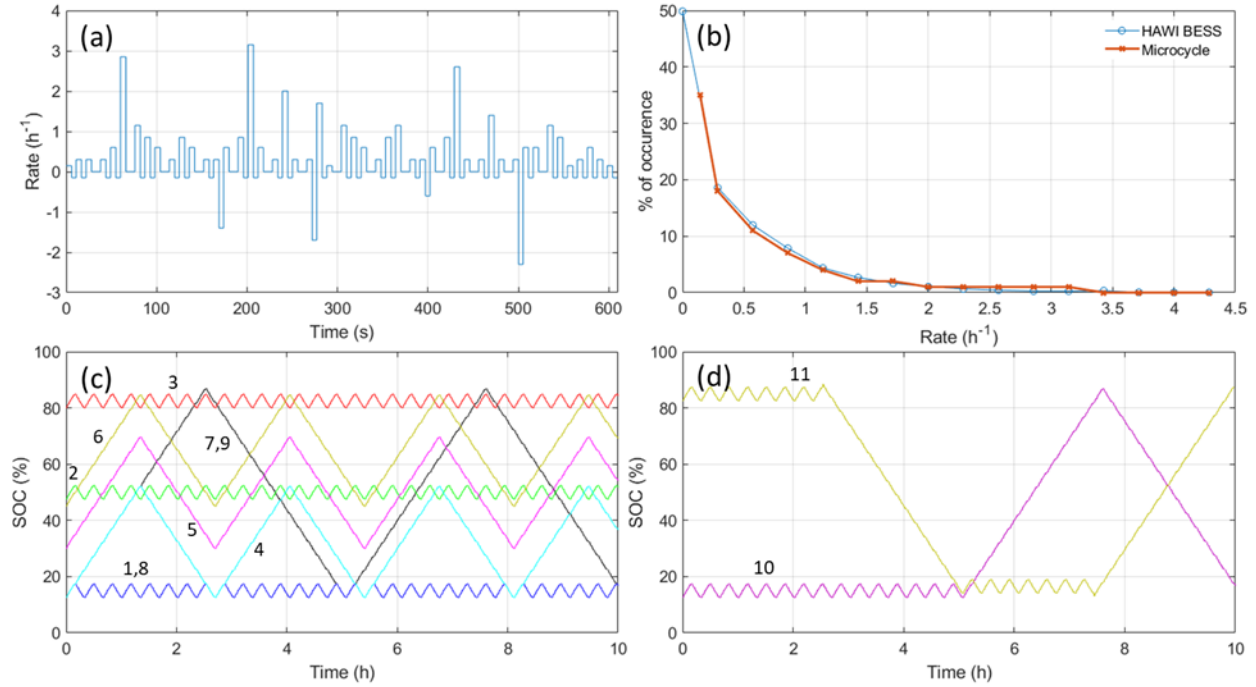


Figure 2.2.1. Plots of (a) the microcycle used in this work, (b) the comparison of the 6 years of BESS average power usage vs. the microcycle, (c) the nine single-segment, and (d) two mixed duty cycles tested in this work.

The second study (Dubarry *et al.*, 2021) carefully studied more than seven years of usage of a grid-tied BESS system on the Island of Hawai'i comprising of generation 1 lithium titanate batteries. The BESS has been well used and it provided significant storage capability for the grid. Its performance was still within specifications after seven years and the only maintenance performed was the replacement of two modules that appeared to suffer from the disconnection of 1 of the 7 cells in parallel within a module. Despite some temperature inhomogeneities, with modules running consistently 5°C or hotter than others, the capacity of the BESS was not affected much with a difference of around 1% capacity loss between the hottest and the coolest modules. However, the temperature induced a slightly different degradation pattern that might induce accelerated degradation for the hotter modules later in life. The overall capacity loss on the deployed modules was estimated to be between 5 and 10% after seven years of usage compared to 15% estimated at the BESS level. This calculation was only obtainable from swapped modules after 2,500 days of usage. The internal module capacity estimation was vastly overestimated by between 10 and 25%, despite our best efforts. We believe that inaccuracies in the capacity measurement and the lack of information on the balancing prevented the correct estimation. This could prove problematic for future deployments and better solutions need to be enacted to ensure accurate estimation. This could include better safeguards for capacity estimation and the option to stop balancing, or monitor it better while performing reference tests. Nonetheless, the BESS performed well and, according to a forecast established using the method established in Baure & Dubarry (2020) for generation 2 cells, its useful lifespan should exceed 15 years on the grid with a capacity loss below 30% (Figure 2.2.2).

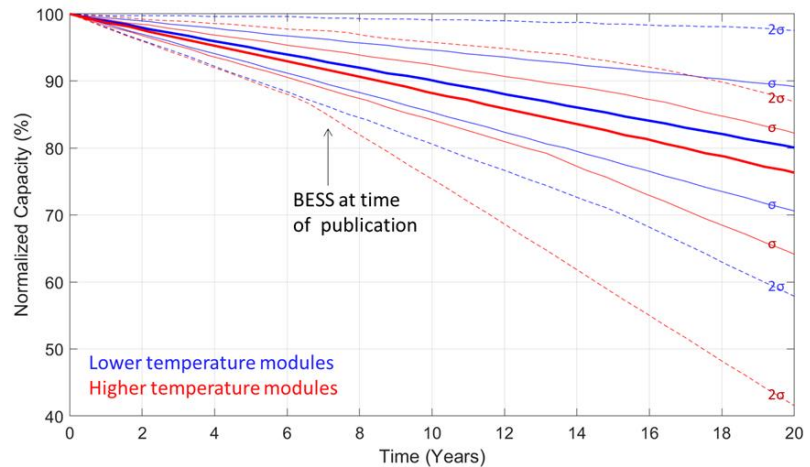


Figure 2.2.2. Forecast of capacity loss based on degradation modes extrapolation with $\pm 3\%$ of the estimation performed around day 1000 on 3 modules believed to be representative of the BESS.

Development of Battery Non-Invasive Characterizations

Accurate lithium battery diagnosis and prognosis are critical to cost-effective operation of electric vehicles and grid-tied storage systems. They are both complex due to the intricate, nonlinear, and path-dependent nature of battery degradation. Data-driven models are anticipated to play a significant role in the behavioral prediction of dynamical systems such as batteries. However, they are often limited by the amount of training data available. Through the project period of APRISES17, we generated the first big data comprehensive synthetic datasets to train diagnosis and prognosis algorithms (Dubarry & Beck, 2020 and Dubarry & Beck, 2021) and we used those datasets to train a novel image-based machine learning algorithm (Costa *et al.*, 2022). The proof-of-concept datasets are over three orders of magnitude larger than what is currently available in the literature. With these benchmark datasets, results from different studies could be easily equated, and the performance of different algorithms can be compared, enhanced, and analyzed extensively. This work expended critical capabilities of current AI algorithms, tools, and techniques to predict scientific data.

In the Dubarry & Beck (2020), we presented a proof-of-concept methodology to generate big data training datasets for intercalation batteries using a mechanistic approach that combines both modeling and experimental techniques to provide a universal tool for the creation of synthetic voltage curves practically indistinguishable from real data. This approach offers the benefits of the broad applicability of the model to various cell chemistries, designs, and operating modes, as well as the high fidelity as inherited from the detailed extraction of the experimental data. The methodology could be applied to the generation of training datasets encompassing the entire degradation spectrum as well as different operating conditions such as rate and temperature. Scenarios leading to lithium plating with adjustable reversibility could be added and the addition of random noise on the data could be considered to make the datasets even more realistic and consider the impact of real-life testing machines' precision and accuracy.

As a proof-of-concept, we generated and analyzed three diagnosis datasets each containing more than 700,000 individual voltage vs. capacity curves and three prognosis datasets with more than 130,000 individual degradation paths for three of the main commercial battery chemistries (Dubarry & Beck, 2021). Our investigation showcased that using the diagnosis techniques developed by HNEI offer accuracies below 1% up to cycle 400 for capacity loss estimations and more than 300,000 different degradations (Figure 2.2.3). Further, using HNEI techniques for prognosis, end-of-life was forecasted with accuracies better than what is achievable with state-of-the-art methodologies. It also showcased that end-of-life is highly dependent on the degradation paths and that new methodologies must be validated on diverse datasets to be considered validated.

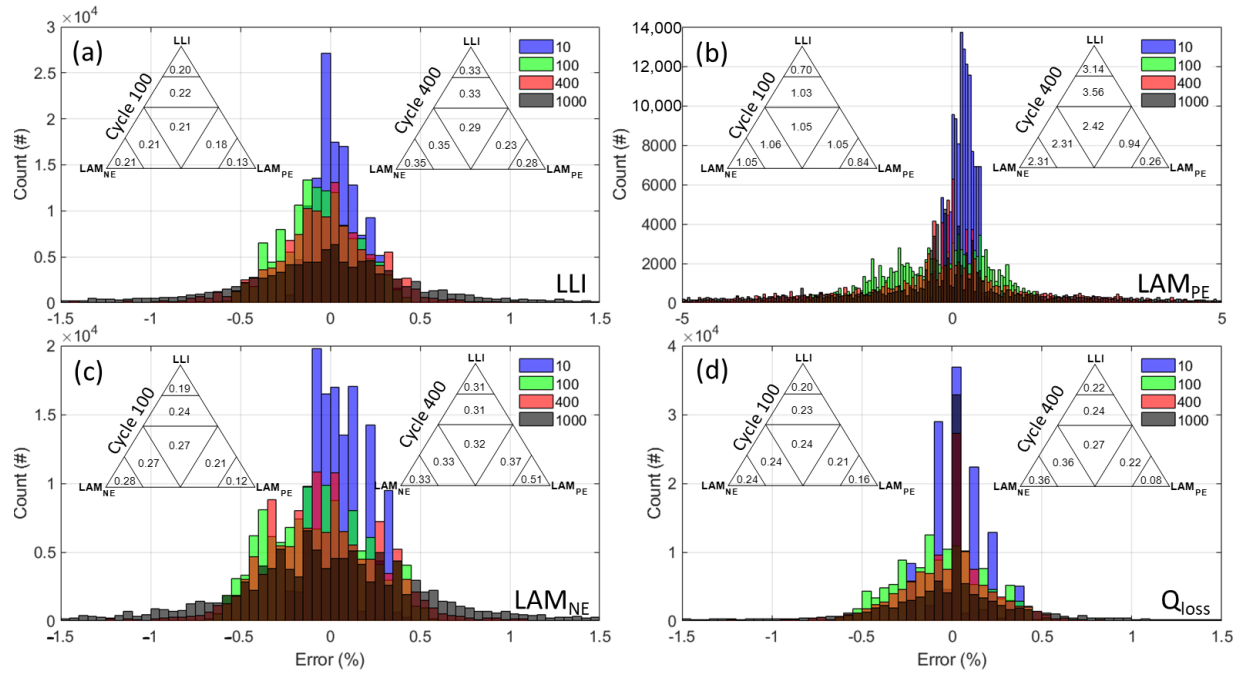


Figure 2.2.3. Mean diagnosis errors for the >125,000 duty cycle as a function of cycle number for (a) loss of lithium inventory, (b) loss of active material on the positive electrode, (c) loss of active material on the negative electrode, and (d) the capacity loss for the graphite / LiFePO₄ cell. Inset ternary diagrams represents the standard deviation between the diagnosis and the real value for different degradation paths at cycle 100 and 400.

In addition to the HNEI in-house diagnosis and prognosis techniques, we also collaborated with the University of Oviedo (Spain) to use the synthetic datasets to train a novel machine learning algorithm based on dynamic time warping (DTW) that represents battery data as images with the aim of enabling the use of powerful artificial intelligence models in this domain (Figure 2.4.4) (Costa *et al.*, 2022). The synthetic voltage curves were used to train a convolutional neural network (CNN) that successfully predicts the main degradation mechanisms on the three commercial cells of different chemistries mentioned above. The superiority of this approach was demonstrated when compared to other state-of-the-art methods, in part driven by the adaptive nature of the algorithm to different cell configurations. The model was also tested on real cells, where the diagnosis corresponds to a large extent with previously existing studies on the subject.

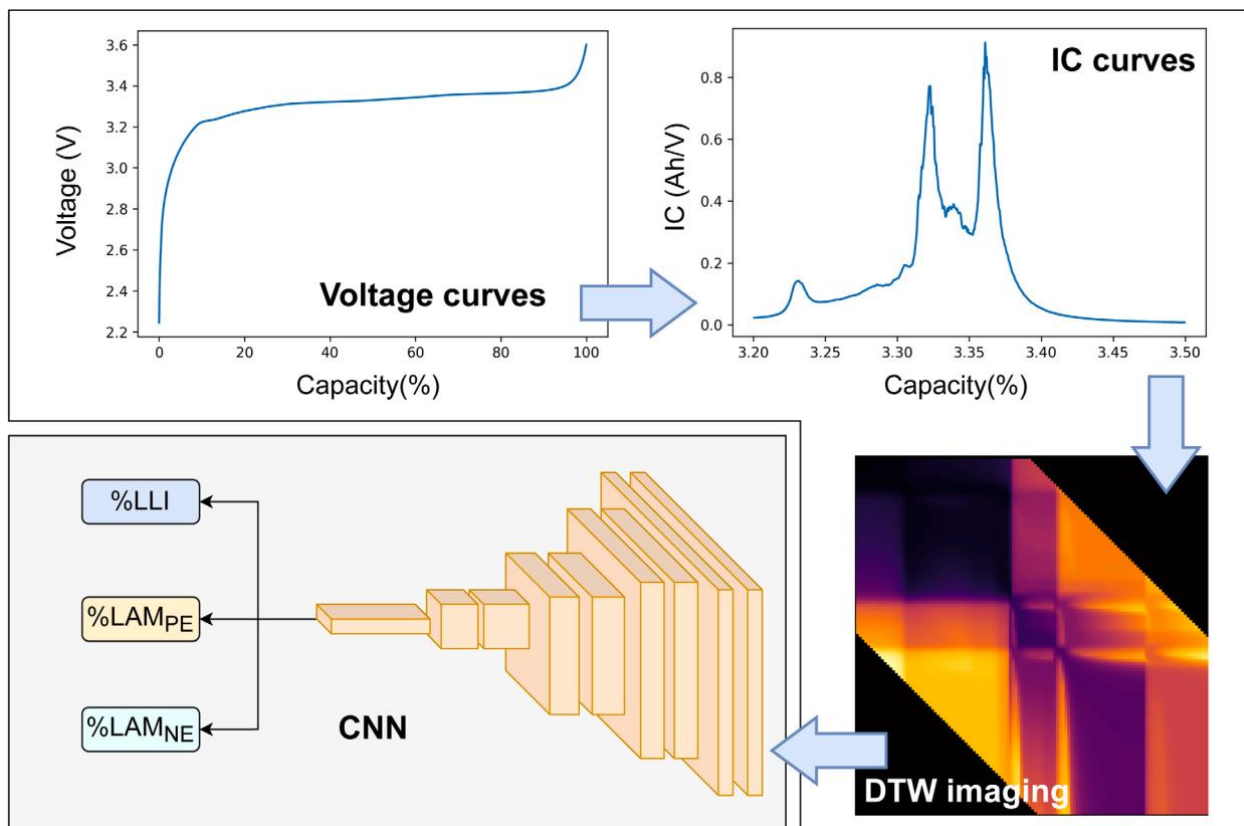


Figure 2.2.4. Pipeline of the proposed solution. In the preprocessing step, the voltage curves are derived and fed to the proposed algorithm to compute their representation as an image. Subsequently, the processed IC images are treated by a CNN that numerically quantifies the percentage of each degradation mode.

Although there is still a lot of work to be done to optimize the technique, results are extremely promising and should accelerate the development of accurate algorithms. The proof-of-concept datasets used in these works were limited to thermodynamic degradations at constant temperature for single-component electrodes and more complicated cases will be investigated under subsequent APRISES-funded projects. Finally, we would like to point out that our intent is no way to remove the need for experimental testing all-together. On the contrary, experimental testing is still essential, and the only way, to decipher which conditions cater to specific degradation paths and its input is, therefore, fundamental to decipher the applicability of batteries for a given application. Our methodology can be used alongside to develop the needed algorithms once a cell is selected.

Desalination Batteries

Traditional desalination techniques separate pure water from a saline solution by using either thermal-, or pressure-based chemical potential gradient. Despite major technological improvements over the past half-century, energy consumption remains a major issue for desalination facilities. The aim to reduce the energy used for desalination led to the development of new technologies such as capacitive deionization (CDI), an electrochemically driven

desalination technology that extracts ions from saline water through the application of electric potential across two conductive porous electrodes. However, capacity deionization is usually limited by the low salt adsorption capability of the electrodes and by poor durability. A possible improvement is to replace the current carbon-based electrodes by materials that can store Na-ions by intercalation rather than adsorption. Such materials are commonly used for Na-ion batteries, a cousin of the Li-ion batteries, that are recently becoming available. Herein, we started and investigated sodium intercalation electrodes as a replacement for the activated charcoal electrodes used in typical capacitive deionization devices. Among the proposed materials for desalination batteries, hexacyanoferrate Prussian blue analogue materials (PBAs) are especially interesting because of their open framework structure that allow insertion of Na ions with high reversibility and rapid kinetics. For this work, and to increase the technology readiness level (TRL), we investigated different practical and scale-up aspects simultaneously, notably electrode material, electrode architecture, and cell design.

Performance and durability results of our best material are presented in Figure 2.2.5. Our best material started with a salt adsorption capability above 120 milligram (mg) per gram (g) at low rate and above 80 mg/g at rates above 100 mg/g/minute (min). This is far above classic CDI material performance at around 10 mg/g at a rate of 30 mg/g/min. After 1,000 cycles, our material still maintained a salt adsorption capability around 50 mg/g at rates above 100 mg/g/min. While this promising, some significant challenges remain. First, the performance at low salt concentration is poor. Second, there seems to be a high impact of the synthesis, washing, drying, storage condition, and electrode architecture on performance. This limits reproducibility of the results which is a big issue for potential scale-up. These challenges will be investigated in APRISES18 onwards.

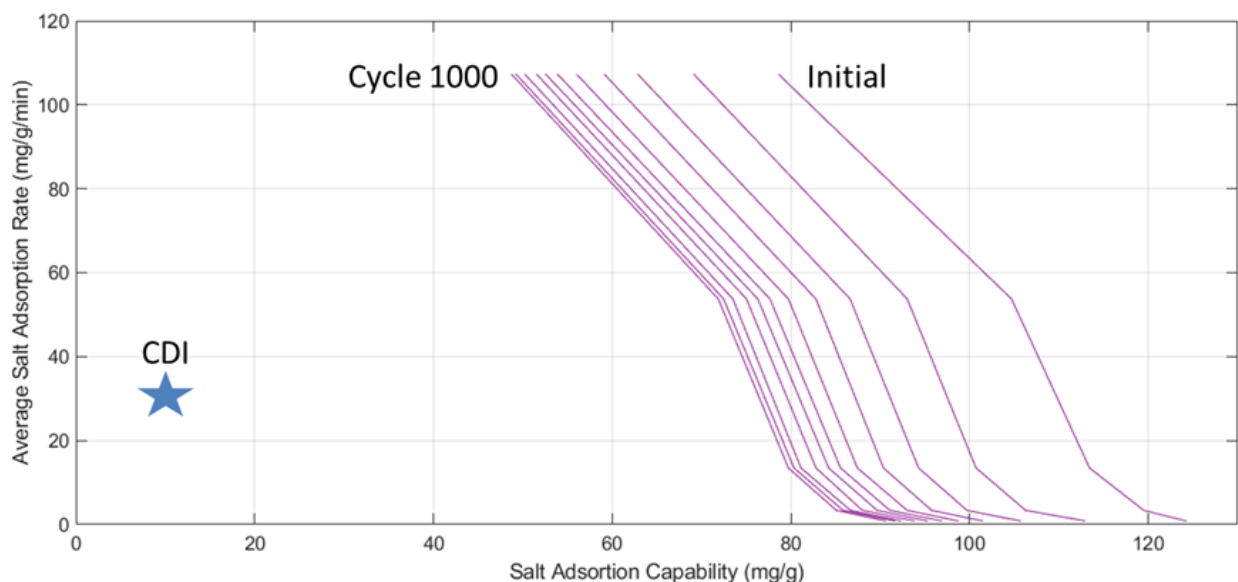


Figure 2.2.5. Performance and durability of our best material.

Other Works Produced

In addition to the research presented above, APRISES17 funding was also used to publish a review and two perspective articles.

In anticipation of the work on inhomogeneities that will be reported under APRISES18, a literature review was conducted on the topic (Beck *et al.*, 2021). Battery degradation is a fundamental concern in battery research, with the biggest challenge being to maintain performance and safety upon usage. From the microstructure of the materials to the design of the cell connectors in modules and their assembly in packs, it is impossible to achieve perfect reproducibility. Small manufacturing or environmental variations will compound big repercussions on pack performance and reliability. This review covered the origins of cell-to-cell variations and inhomogeneities on a multiscale level, their impact on electrochemical performance, as well as their characterization and tracking methods, ranging from the use of large-scale equipment to in-operando studies (Figure 2.2.6).

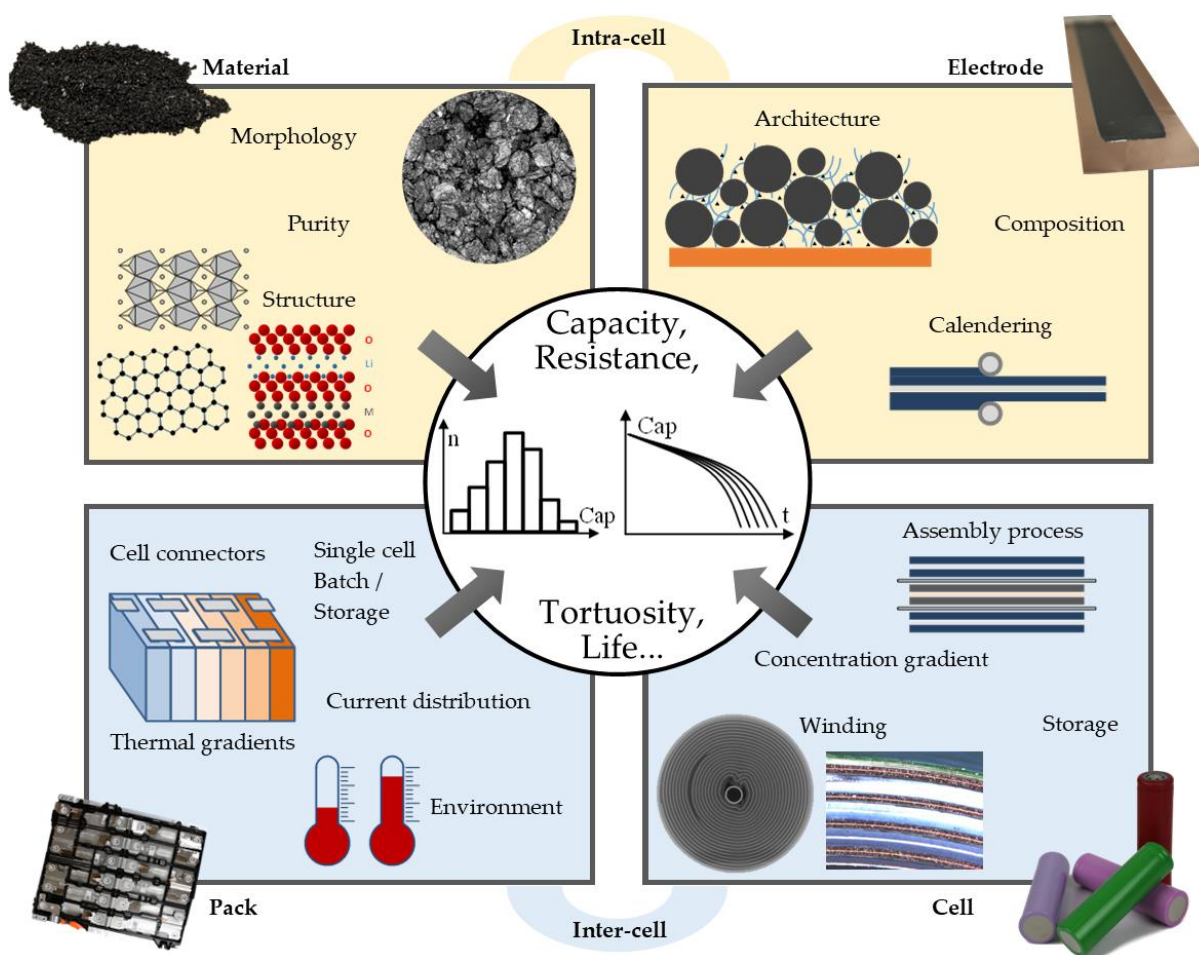


Figure 2.2.6. Summary of topic covered in our review on battery inhomogeneities.

Looking at the perspective articles, one was on battery testing in general (Dubarry & Baure, 2020) and the second was focused exclusively on incremental capacity analysis (Dubarry & Anseán, 2022). Laboratory battery testing is a much more complex task than it appears. Properly defined and executed plans expedite a deeper understanding of the performance and state of health (SOH) of commercial batteries. Inadequate validation can delegitimize a good study. Dubarry & Baure (2020) presented best practices for simple and effective testing of batteries based on the protocols developed in-house for the past decade of work under APRISES funding and other sources. For the most part, execution only requires a multichannel potentiostat/galvanostat without the need for other complex instrumentation. This will allow characterization of not only the cell-to-cell variations but also evolution of SOH throughout the lifetime of the cells. Although this publication was centered on single cell testing, the same approach can also be used for modules or packs if safety controls are in place so that no single cell can be overcharged or overdischarged. While Dubarry & Baure (2020) discussed the importance of the analysis of the voltage response of the cell; another perspective article, Dubarry & Anseán (2022), was necessary to fully cover the topic of incremental capacity analysis, a technique proven to be an effective and versatile tool for in-situ diagnosis of Li-ion batteries. This publication presented best practices with detailed examples for the majority of the battery chemistry available to date. Key takeaways to ease its application are summarized below in Table 2.2.1.

Table 2.2.1. Key takeaways noted in Dubarry & Anseán (2022).

<i>Process</i>	<i>Remarks</i>
<i>Test preparation</i>	<ul style="list-style-type: none"> - Limit environmental and procedural errors - Ensure environmental consistency throughout testing (temperatures and physical location)
<i>Battery testing</i>	<ul style="list-style-type: none"> - Reference testing at constant current at low C-rates (C/25) and regular intervals (typically every 100 cycles, 1 month or 2-4% capacity loss) - Data sampling at 1 to 2 mV or 2,000 points per step
<i>Data processing</i>	<ul style="list-style-type: none"> - Filter data to reduce noise and to set a fixed voltage interval step (generally 2 mV) - Smooth filtered voltage data if necessary. Check for possible distortions - Proceed with the derivation of the voltage data ($IC = \Delta Q / \Delta V$). - Verify correctness of IC curve (no peak movement or intensity changes)
<i>Electrochemistry</i>	<ul style="list-style-type: none"> - Incremental Capacity is chemistry dependent. Refer to literature for expected peaks - Identify and number all peaks on the derived IC curves according to the reactions in the PE and NE
<i>Degradation modes</i>	<ul style="list-style-type: none"> - Fundamental understanding of the degradation modes, LLI, LAMs, ORI and FRD is required for cell diagnosis. Refer to literature - Fundamental understanding of the clepsydra analogy
<i>Cell parameters</i>	<ul style="list-style-type: none"> - Resistance estimation of the tested cells. Current-step methods can be applied - Determination of the limiting electrodes - Estimation of the initial loading ratio (LR) and offset (OFS) via electrode matching, emulations, or using common values from the literature

Degradation maps	<ul style="list-style-type: none"> - Review of the degradation maps for the tested chemistry. Maps can be self-generated or extracted from literature (see supplementary material for most common commercial chemistries) - Use of the look-up tables for IC peak evolution with degradation modes - Extraction of most sensitive FOIs for the tested cell technology
Cell diagnosis	<ul style="list-style-type: none"> - Evaluate ORI - Evaluate the degradation mode that causes capacity loss (identifying limiting electrodes and compare to degradation maps and tables) - Evaluate remaining thermodynamic degradation modes via FOI analysis - DVA could be best strategy to get LAM_{NE} - Evaluate kinetic limitations if peak shapes unexplainable
Other considerations	<ul style="list-style-type: none"> - Blends must be separated for analysis - IC during charge or discharge, use most relevant for application. Peaks always broader towards end-of-regime - Peak area analysis is useful only if IC peaks go back close to zero before next peak starts - If reversible plating, new feature should be visible. If not, likely irreversible and increasing LLI

Publications and Presentations

Peer-Reviewed Publications

1. Baure, G., & Dubarry, M. (2020). Battery durability and reliability under Electric Utility Grid Operations: 20-year forecast under different grid applications. *Journal of Energy Storage*, 29, 101391. <https://doi.org/10.1016/j.est.2020.101391>.
2. Dubarry, M., & Baure, G. (2020). Perspective on commercial Li-ion battery testing, best practices for simple and effective protocols. *Electronics*, 9(1), 152. <https://doi.org/10.3390/electronics9010152>.
3. Dubarry, M., & Beck, D. (2020). Big Data Training Data for artificial intelligence-based Li-ion diagnosis and prognosis. *Journal of Power Sources*, 479, 228806. <https://doi.org/10.1016/j.jpowsour.2020.228806>.
4. Dubarry, M., & Beck, D. (2021). Analysis of synthetic voltage vs. capacity datasets for big data li-ion diagnosis and prognosis. *Energies*, 14(9), 2371. <https://doi.org/10.3390/en14092371>.
5. Beck, D., Dechent, P., Junker, M., Sauer, D. U., & Dubarry, M. (2021). Inhomogeneities and cell-to-cell variations in lithium-ion batteries, a review. *Energies*, 14(11), 3276. <https://doi.org/10.3390/en14113276>.
6. Dubarry, M., Tun, M., Baure, G., Matsuura, M., & Rocheleau, R. E. (2021). Battery durability and reliability under Electric Utility Grid Operations: Analysis of on-site reference tests. *Electronics*, 10(13), 1593. <https://doi.org/10.3390/electronics10131593>.
7. Costa, N., Sánchez, L., Anseán, D., & Dubarry, M. (2022). Li-ion battery degradation modes diagnosis via convolutional neural networks. *Journal of Energy Storage*, 55, 105558. <https://doi.org/10.1016/j.est.2022.105558>.

8. Dubarry, M., & Anseán, D. (2022). Best practices for incremental capacity analysis. *Frontiers in Energy Research*, 10. <https://doi.org/10.3389/fenrg.2022.1023555>.

Conference Proceedings and Presentations

1. Dubarry, M. (2021, January 12-13). *Battery Durability and Reliability Under Grid Operations*. Alaska Energy Storage Workshop, Virtual.
2. Love, C. T., Carter, R. E., Kingston, T.A., Atkinson III, R., Parmananda, M., Dubarry, M., Fear, C., & Mukherjee, P. P. (2021, May 30 - June 3). *Directionality of Thermal Gradients in Li-Ion Batteries Dictates Diverging Failure Modes*. 239th Electrochemical Society Meeting, Chicago, IL, United States.
3. Dubarry M., & Beck D. (2021, May 30 - June 3). *A New Insight into Blended Electrodes*. 239th Electrochemical Society Meeting, Chicago, IL, United States.
4. Dubarry M., & Beck D. (2021, May 30 - June 3). *Big Data for Li-Ion Diagnosis and Prognosis*. 239th Electrochemical Society Meeting, Chicago, IL, United States.
5. Dubarry M., & Beck D. (2021, October 10-14). *A New Insight into Blended Electrodes*. 240th Electrochemical Society Meeting, Orlando, FL, United States.
6. Carter, R. E., Kingston, T. A., Atkinson, R. W., Parmananda, M., Dubarry, M., Fear, C., Mukherjee, P. P., & Love, C. T. (2021, October 10-14). *Electrode Specific Degradation Tailored By the Directionality of Thermal Gradients in Li-Ion Batteries*. 240th Electrochemical Society Meeting, Orlando, FL, United States.
7. Sahin, N., Morton, J., & Dubarry, M. (2021, October 10-14). *Optimization of Prussian Blue Analogues for Na-Ion Desalination Batteries*. 240th Electrochemical Society Meeting, Orlando, FL, United States.
8. Dubarry, M., & Beck, D. (2021, December 7-9). *Big Data for Li-Ion Diagnosis and Prognosis*. Advanced Automotive Battery Conference/Battery Intelligence Symposium, San Diego, CA, United States.
9. Kingston, T. A., Love, C. T., Carter, R. E., Atkinson III, R., Parmananda, M., Dubarry, M., Fear, C., & Mukherjee, P. P. (2021, November 1-5). *Altering the Degradation Mode in Li-ion Batteries Through Directional Application of an Interelectrode Thermal Gradient*. International Mechanical Engineering Congress & Exposition, Virtual.
10. Dubarry, M., & Beck, D. (2022, May 8-13). *Big Data for Li-Ion Diagnosis and Prognosis*. Material Research Society Spring Meeting, Honolulu, HI, United States.
11. Sahin, N., Morton, J. & Dubarry, M. (2022, May 8-13). *Optimization of Prussian Blue Analogues for Na-Ion Desalination Batteries*. Material Research Society Spring Meeting, Honolulu, HI, United States.
12. Dubarry, M., & Baure, G. (2022, May 8-13). *Lithium Titanate Battery Durability and Reliability Under Electric Utility Grid Operations*. Material Research Society Spring Meeting, Honolulu, HI, United States.
13. Dubarry, M., & Beck, D. (2022, June 5-10). *Big Data for Lithium-Ion Battery Diagnosis and Prognosis*. Gordon Battery Conference, Ventura, CA, United States.

14. Dubarry, M., & Beck, D. (2022, June 5-10). *Recent Advances in the Intercalation Battery Mechanistic Modeling Approach*. Gordon Battery Conference, Ventura, CA, United States.
15. Dubarry, M., (2022, July 17-21). *Battery energy storage system modeling: A combined comprehensive approach*. IEEE Power & Energy Society General Meeting, Denver, CO, United States.
16. Dubarry, M., & Beck, D. (2022, October 9-13). *Mechanistic Li-Ion Battery Modeling, What's Next?*. 242nd Electrochemical Society Meeting, Atlanta, GA, United States.
17. Dubarry, M., Costa, N., & Matthews, D. (2022, October 9-13). *Data-Driven Diagnosis of PV connected Batteries*. 242nd Electrochemical Society Meeting, Atlanta, GA, United States.
18. Dubarry, M. (2022, December 5-8). *Big Data in Diagnostics Data-Driven Direct Diagnosis of PV Connected Batteries*. Advanced Automotive Battery Conference/Battery Intelligence Symposium, San Diego, CA, United States.

TASK 3: BIORENEWABLE RESOURCES

This section presents two research subtasks focused on the use of biorenewable resources to serve Navy needs, including fuels, waste treatment, and novel materials. Fuels are omnipresent across the Navy's operating environments and maintaining fuel quality and performance as new fuels are introduced to supply systems is of the utmost importance. Needs for waste treatment span a range from forward Marine units to base-scale installations. Biorenewable resources provide unique feedstocks for developing new materials for advanced applications to support the warfighter. Details of each research subtask are provided in the following sections.

3.1 Constant Volume Carbonization for Waste Management

Solid waste and biosolids present management challenges for forward contingency bases and larger scale installations. Environmental impacts may be reduced by converting waste to stabilized solids that can be safely disposed for biological degradation or more readily converted to useful forms of energy. The constant volume carbonization (CVC) process [1-4] has potential to accomplish both goals with low emissions. The purpose of this task is to evaluate the CVC process for use in stabilizing and homogenizing solid waste and/or biosolids representative of waste streams relevant to the Navy. HNEI's main objectives were:

1. Evaluate pressurized carbonization as a tool to treat and stabilize materials representative of waste from contingency bases;

2. Identify pressurized carbonization reaction conditions that produce transient plastic phase solid products; and
3. Characterize the products from pressurized carbonization of waste under different test conditions.

Materials and Methods: Characteristics of waste streams at contingency bases described elsewhere [5-7] were used to create two synthetic waste recipes that could be readily reproduced for CVC experiments (Table 3.1.1). The recipes included five ingredients: food waste, mixed paper, plastic, wood, and rubber. The standard recipe was based on an average waste stream from the force provider waste studies and the polystyrene recipe contained higher polystyrene content compared to the standard recipe. Plastics are common in force provider waste streams and present a challenge in higher concentrations.

Table 3.1.1. Composition of the standard (ST) and polystyrene (PS) recipes for waste simulation.

Material	Standard Recipe Composition (wt. %)	Polystyrene Recipe Composition (wt. %)	Material Description
Food Waste	35	32	25% Gravy Train® Beef Dry Dog Food, 75% deionized water
Mixed Paper	30	27.3	Cellulose particles from paper food trays
Plastic	15	22.5	Polystyrene particles from plastic forks
Wood	15	13.7	Norwegian birch wood particles
Rubber	5	4.5	Rubber particles from tires
Total	100	100	

The schematic of the experimental CVC test bed is shown in Figure 3.1.1. The reactor design is based on a 12.5 mm stainless steel tubing with Swagelok fittings with a reactor body length of 255 mm. Common CVC reaction temperatures ranging from ~290 to 550°C are imposed on the sealed reactor by immersing it in a temperature-controlled sand bath (Techne, model SBL-2D). The reactor is loaded with ~12 g of the feedstock, flushed with nitrogen, sealed, leak checked, and then placed in the sand bath. After a prescribed reaction time, the reactor is removed and allowed to cool to ambient conditions. CVC products are recovered from the cold reactor in a fume hood and component masses (solid, free liquid, evaporative loss, and gas) are determined. The solid mass is characterized by observation and proximate (moisture, volatile matter, fixed carbon, ash following ASTM D1762) analysis (LECO Corporation, St. Joseph, MI Thermogravimetric Analyzer (TGA) 801). Selected solid samples were analyzed using a PerkinElmer 8000 to produce detailed thermal analyses and identify differences in chemical structure.

Two sets of experiments were conducted: 1) a fractional factorial design (two levels, four factors) experiment using the ST and PS waste recipes, and 2) a series of experiments using two

components, birch and polystyrene, at varying ratios identified as the BPS tests. The former was used to provide initial information on the impacts of independent reactor variables on CVC product distribution. Based on earlier work, initial (pretest) reactor N₂ pressure (0.0 and 1.7 MPa), CVC reaction temperature (350 and 500°C), and reaction time (30 and 90 minutes) were selected in addition to the two waste recipes. In all cases, the feedstock (ST and PS ingredients) were prepared in 1 to 2 mm particles prior to the reactor test. Conditions are identified by date and by the combination of reactor conditions as summarized in Table 3.1.2 below.

Table 3.1.2. Fractional factorial design (two level, four factor) for CVC experiments.

Date-#	Recipe	Initial Pressure	Temperature	Reaction Time
220826-2	ST	0.0	350	30
220915-1	ST	1.72	350	90
220922-1	PS	0.0	350	90
220928-1	PS	1.72	350	30
220915-2	ST	0.0	500	90
220922-2	ST	1.72	500	30
220928-2	PS	0.0	500	30
220929-1	PS	1.72	500	90

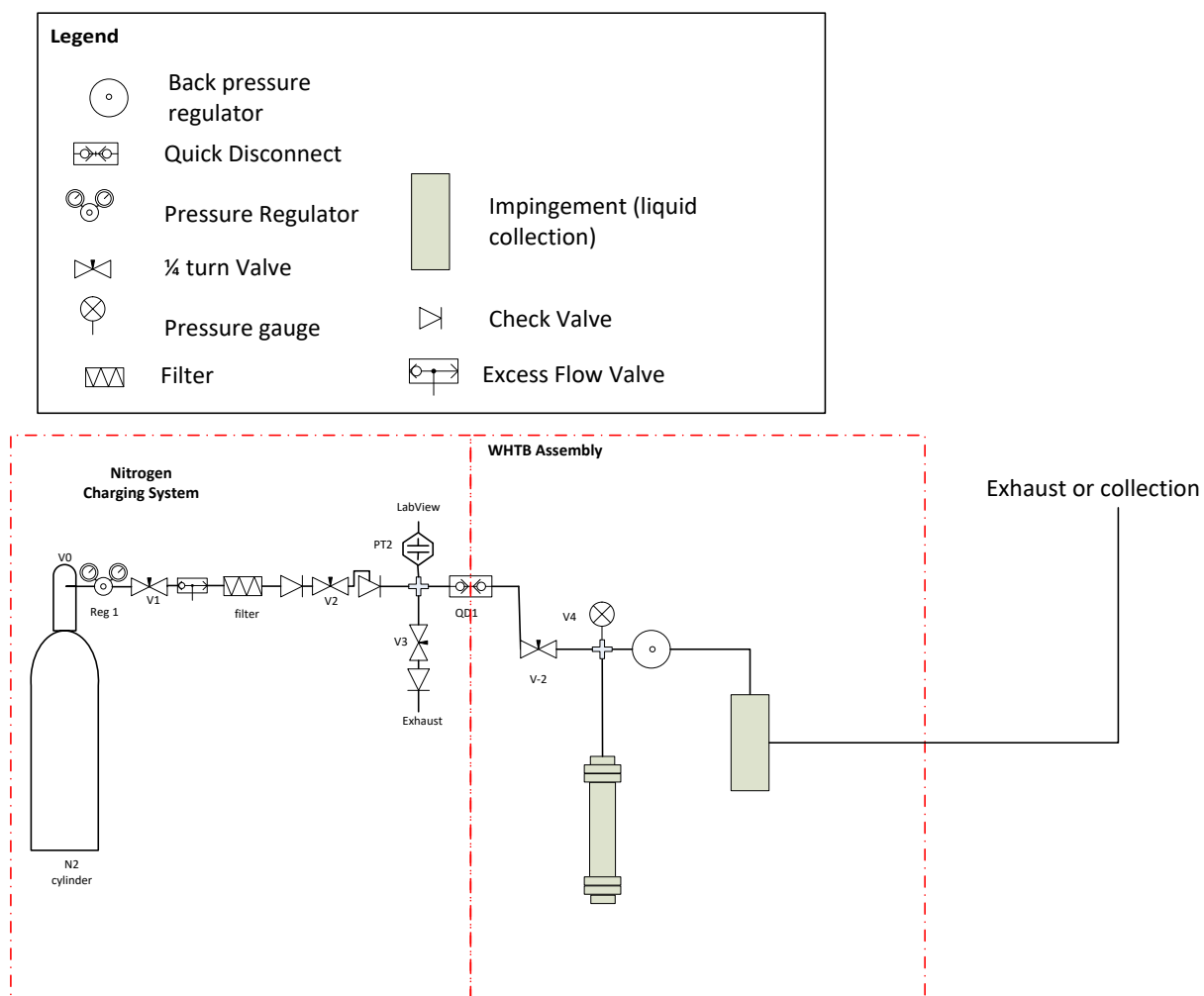


Figure 3.1.1. Schematic diagram of the constant volume carbonization test bed.

Results

This section presents the results of the fractional factorial design experiments using ST and PS feedstocks and the two component birch-polystyrene (BPS) experiments.

Fractional Factorial Design Experiments: Figure 3.1.2 presents images of the CVC solid products from the fractional factorial experiments. The solids appear uniformly colored for each sample indicating that the CVC reaction conditions were effective in thermally degrading the mixture of polymers. Color differences are noticeable between samples, indicating that the varied test conditions may have produced differences in the solid products. The sample images also provide evidence that the 1 to 2 mm feedstock particles have become aggregated during the CVC reaction. While the particle sizes may have been reduced by the effort needed to recover the sample from the reactor, the aggregated structure is a desirable characteristic.

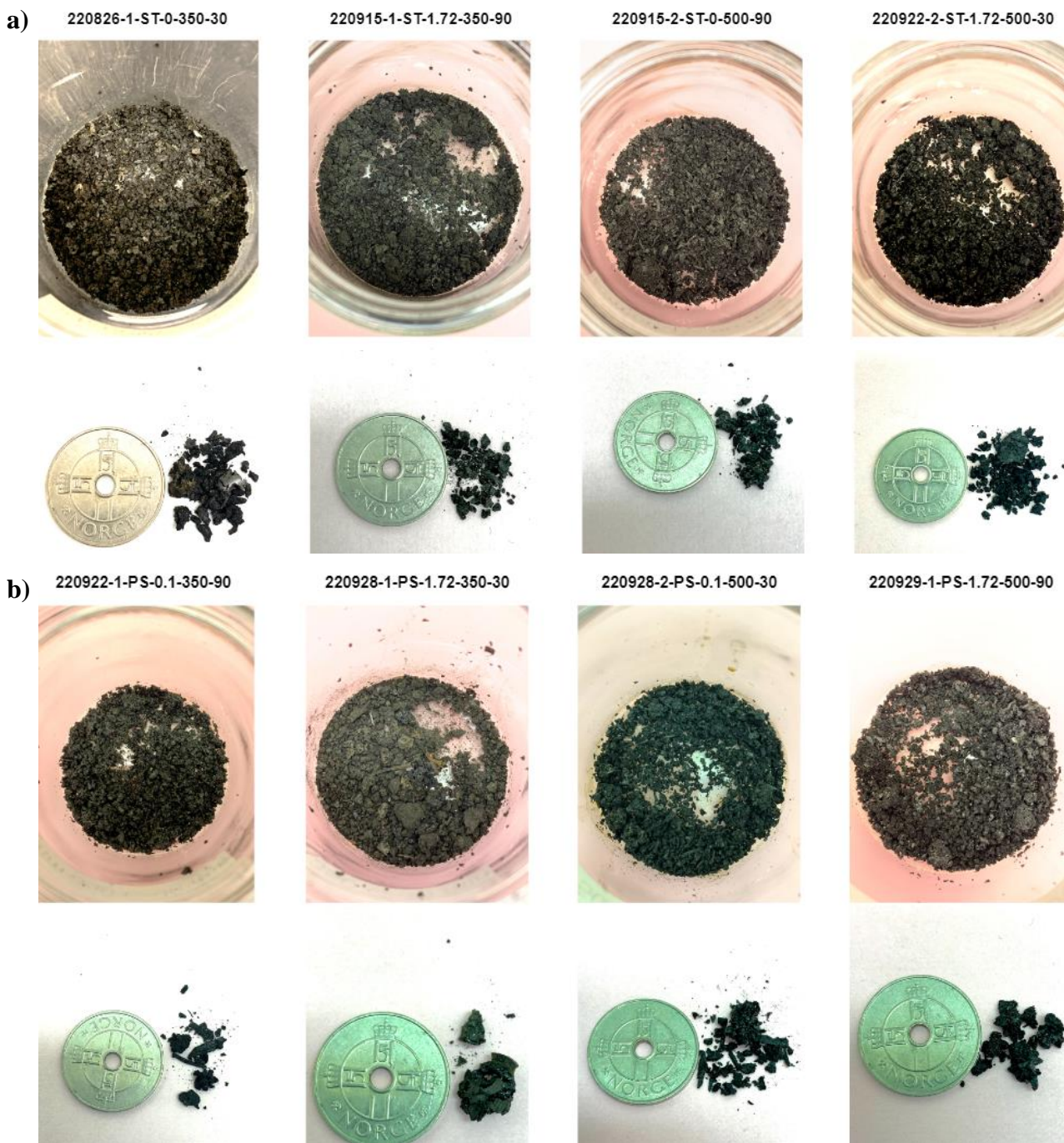


Figure 3.1.2. Images of solid products from the fractional factorial CVC experiments. Coin outer diameter is 22 mm and the center hole is 4 mm. (a) ST waste recipe and (b) PS waste recipe.

Figure 3.1.3 summarizes the product component yield distribution for the fractional factorial experiments. Reaction temperature exhibits the greatest impact on yield distribution, with higher temperature producing less solid product as the synthetic waste components undergo more extensive depolymerization. In these preliminary experiments, the gas yield was not determined quantitatively, but would account for a large part of the “undetermined” fraction.

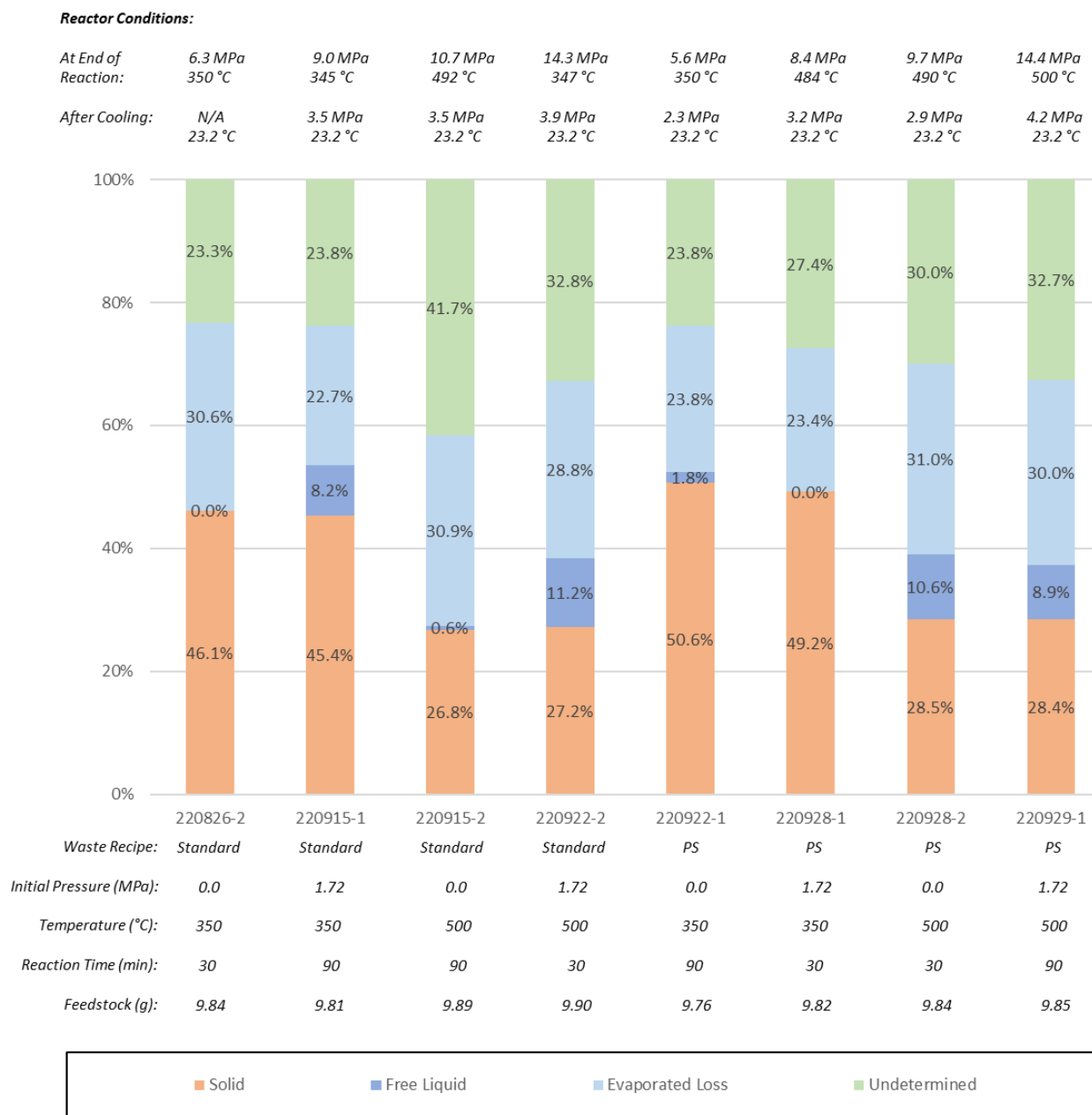


Figure 3.1.3. Summary of CVC product component distributions for the fractional factorial design experiments.

The two reaction times selected for the experimental design show little influence on the CVC product distribution. The data suggest that the heat transfer and kinetic phenomena inherent in the reactor system have approached quasi-equilibrium by the 30 minute mark of each individual test. Extended reaction times may influence the final product distribution and composition, but the addition of 60 minutes is not sufficient to make this apparent.

The two initial reactor pressures (0 and 1.72 MPa) showed little impact on solid yield, but had influence on the formation of a free liquid phase product. The higher pressure produced elevated

free liquid from the ST feedstock, at both reaction temperatures, but the same trend was not apparent for the PS feedstock, where the free liquid phase shows clearer dependence on reaction temperature. These results indicate that the feedstock, temperature, and pressure variables are not affecting the product distribution independently but interactively. This is further supported by difference between feedstocks under similar reaction conditions. At the lower reaction temperature, the PS feedstock produced a greater solid yield and this may be due to the greater polystyrene content of the PS feedstock and the higher depolymerization temperature of the polystyrene compared to the other PS recipe components.

The proximate analysis results for CVC solid products from the fractional factorial design experiments are presented in Figure 3.1.4. The higher reaction temperatures that produced lower solid yields in Figure 3.1.3 are also responsible for elevated fixed carbon contents in those samples and this is consistent with enhanced depolymerization. The PS solids also contain less fixed carbon and more volatile matter than their ST counterparts.



Figure 3.1.4. Summary of proximate analyses of the solid CVC products from the fractional factorial design experiments.

Birch-Polystyrene Two Component Experiments: Figure 3.1.5 presents images of the CVC solid products from the two component BPS experiments. The sample images are uniformly colored indicating that both components participated in the reaction to form a composite product. The images also provide evidence that the 1 to 2 mm feedstock particles have become aggregated during the CVC reaction. Upon opening the reactor after the test, samples may be adherent to the inner walls and particle sizes may have been reduced by the effort to remove them. Nonetheless, the aggregated structure is a desirable characteristic for a stabilized waste product.

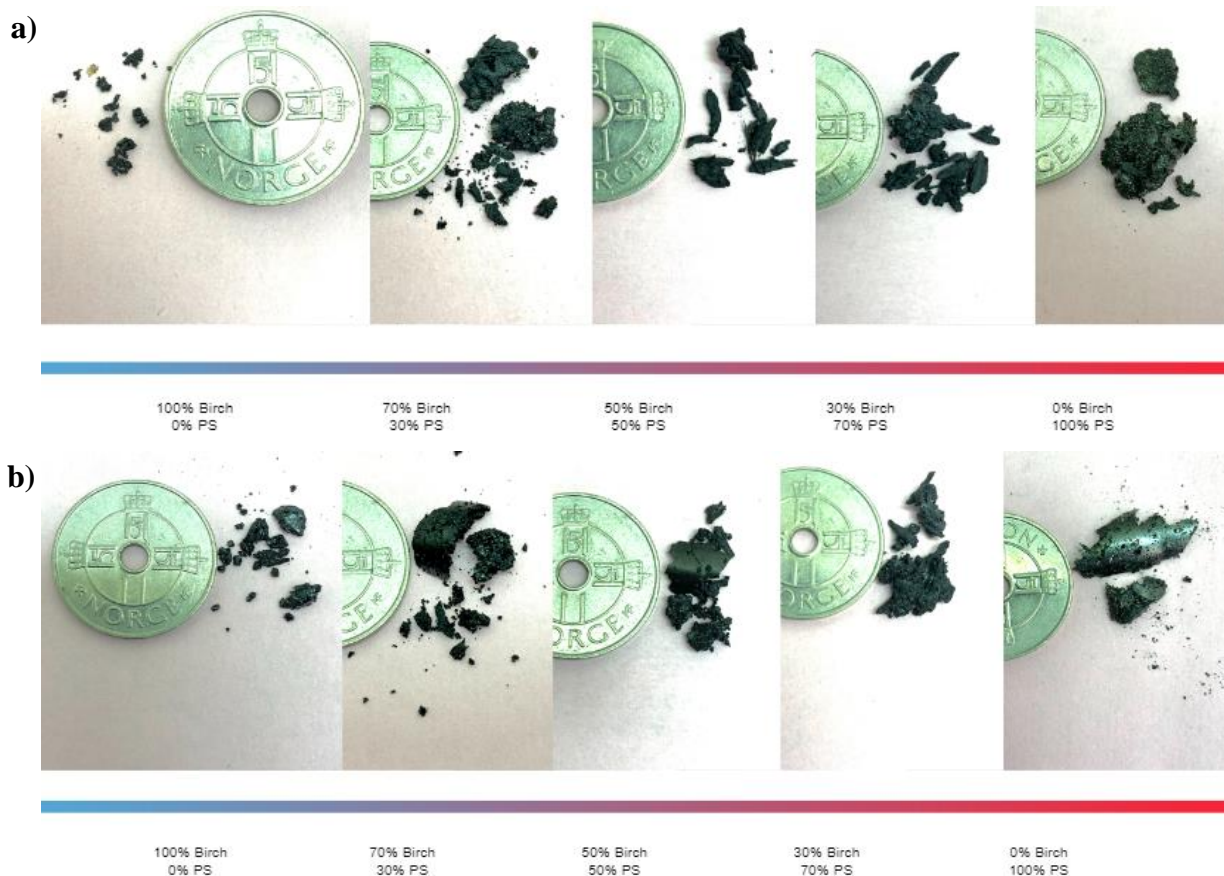


Figure 3.1.5. Images of CVC solid products from the BPS test series with varied mixture ratios of the two components. Experimental conditions are 500°C reactor temperature, 30 minute reaction time, and initial reactor pressures of (a) 0 MPa and (b) 1.72 MPa. Coin outer diameter is 22 mm and the center hole is 4 mm.

Figures 3.1.6 and 3.1.7 summarize the product component yield distribution for the BPS experiments. The CVC test series was performed with a series of birch and polystyrene mixtures (B100PS0, B70PS30, B50PS50, B30PS70, B0PS100 where B=birch and PS=polystyrene and the numbers are the component mass percentage in the feedstock mixture) at 500°C for 30 min with two initial reactor pressures, 0 and 1.72 MPa. Birch and polystyrene single component tests (B100PS0 and B0PS100) provide limiting case expectations for the product distributions. B100PS0 results show little variation between the two pressures, although the degree of solid product aggregation is much higher for the 1.72 MPa condition. The two B0PS100 tests show

differences in response to pressure, with the higher pressure resulting in less solid product formation, and both pressures produce an abundance of free liquid, 70 to 90% of the feedstock mass. The three mixtures of birch and polystyrene show solid product yields more closely aligned with the B100PS0 product distribution, regardless of initial pressure, and little free liquid. This indicates that even modest amounts of birch in the mixture can shift the CVC product characteristics toward solid formation with minimal free liquids.

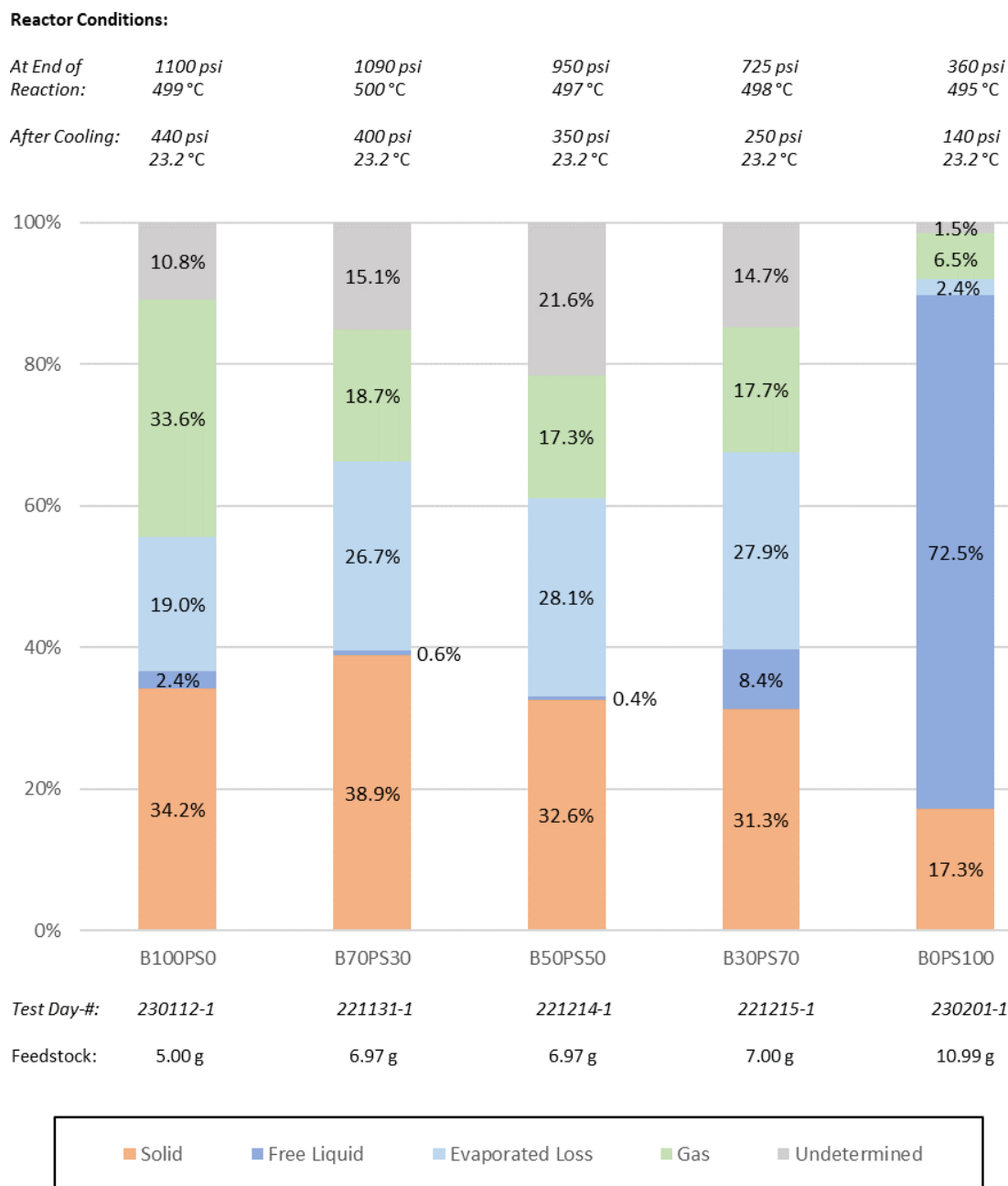


Figure 3.1.6. Summary of CVC product component distributions for the BPS experiments using birch and polystyrene mixtures (B100PS0, B70PS30, B50PS50, B30PS70, B0PS100 where B=birch and PS=polystyrene and the numbers are the component mass percentage in the feedstock mixture) at 500°C for 30 min with initial reactor pressure of 0 MPa.

Reactor Conditions:

<i>At End of Reaction:</i>	1390 psi 500 °C	1700 psi 490 °C	1465 psi 500 °C	1220 psi 500 °C	905 psi 499 °C
<i>After Cooling:</i>	570 psi 23.2 °C	600 psi 23.2 °C	535 psi 23.2 °C	440 psi 23.2 °C	360 psi 23.2 °C

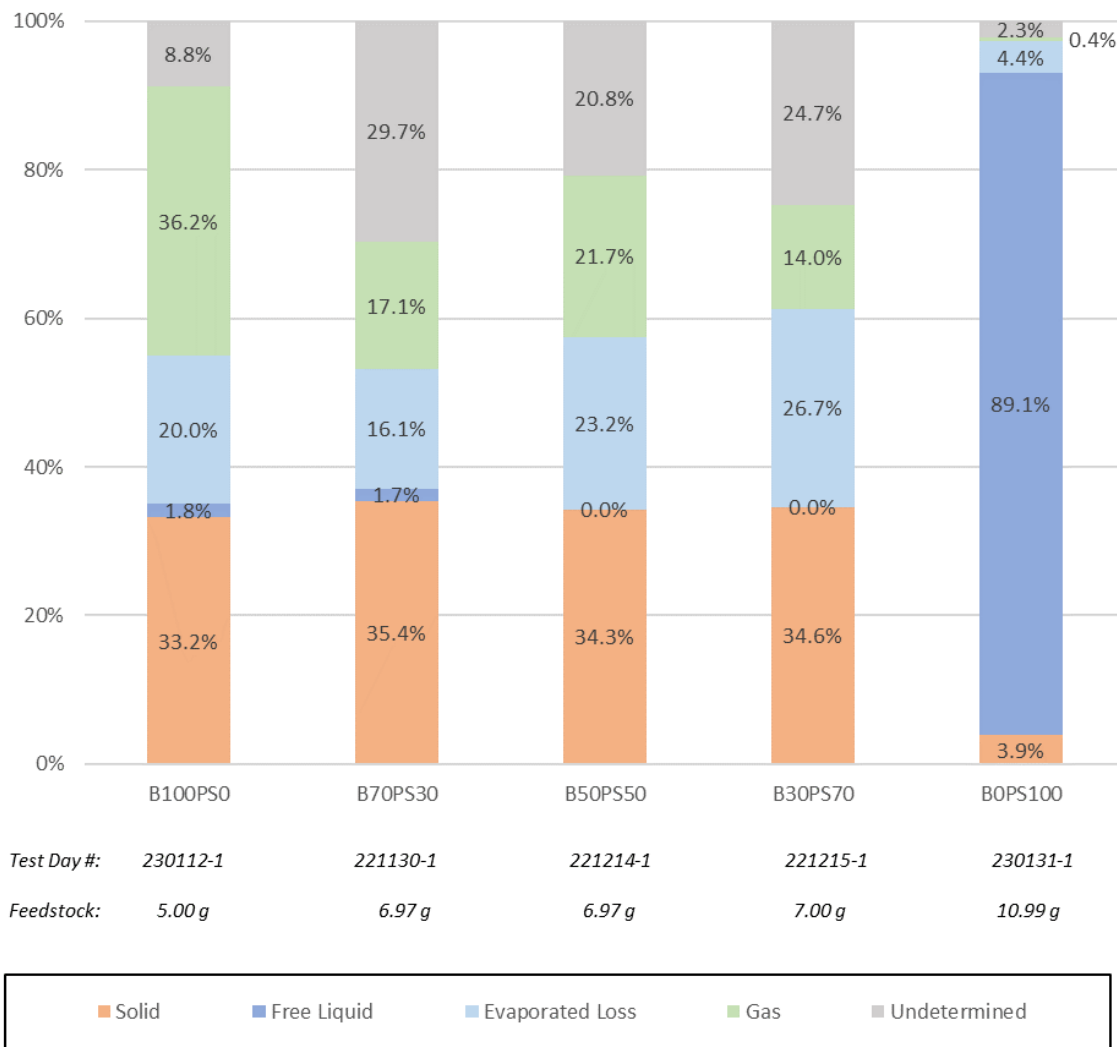


Figure 3.1.7. Summary of CVC product component distributions for the BPS experiments using birch and polystyrene mixtures (B100PS0, B70PS30, B50PS50, B30PS70, B0PS100 where B=birch and PS=polystyrene and the numbers are the component mass percentage in the feedstock mixture) at 500°C for 30 min with initial reactor pressure of 1.72 MPa.

Figure 3.1.8 presents the proximate analysis results for the BPS experiment series. Higher polystyrene content in the feedstock results in reduced amounts of fixed carbon in the CVC product, but not in direct proportion to its percentage in the mixture, e.g. the increase from 30 to 50% polystyrene content results in only a 4% decrease in fixed carbon content. The higher initial reactor pressure produced a higher fixed carbon content (~4% absolute) for the B70PS30 and B50PS50 cases. These results show that process control points may be used to affect stabilized CVC product characteristics.

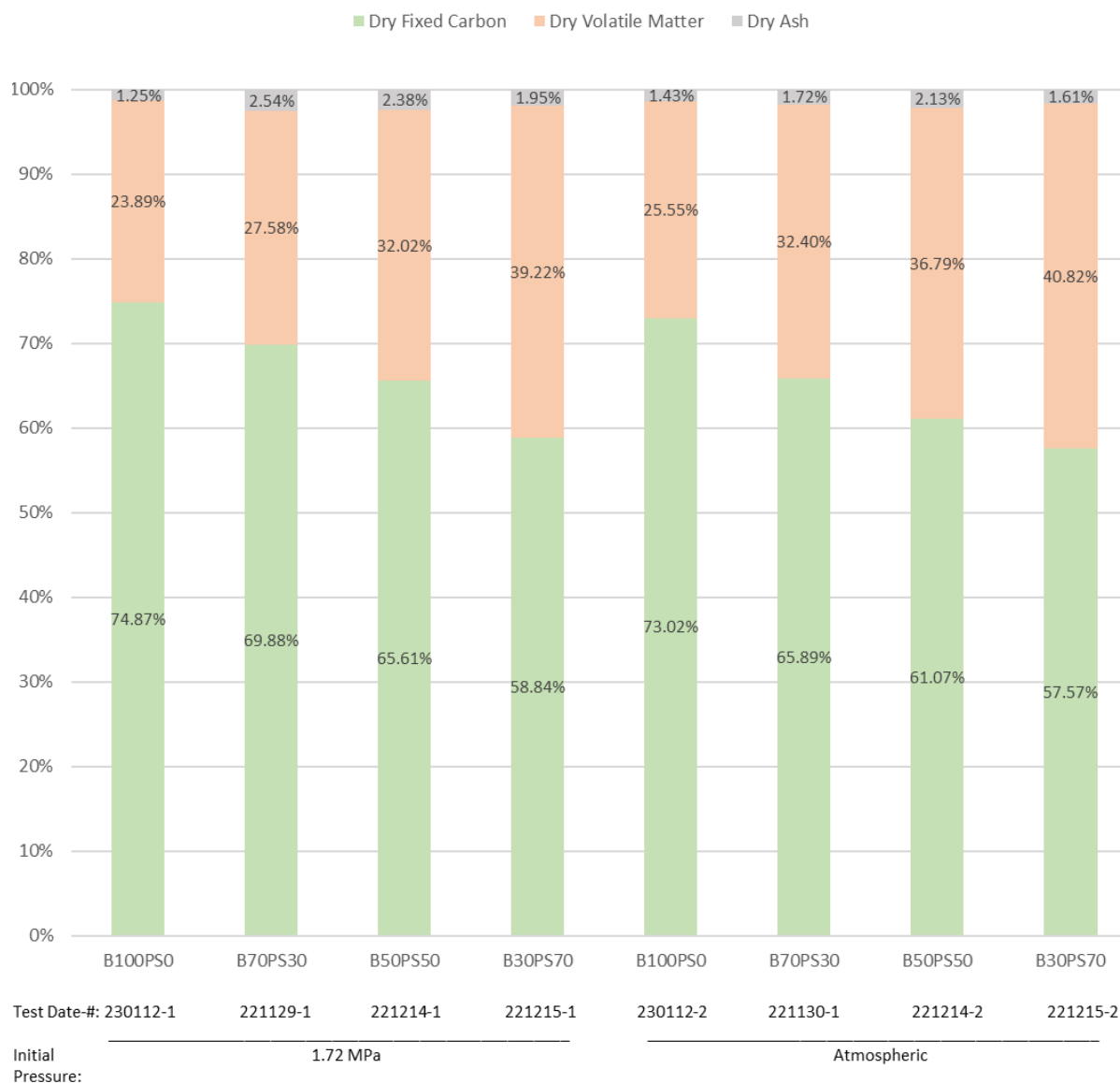


Figure 3.1.8. Summary of proximate analyses of the solid CVC products from the BPS experiment series using birch and polystyrene mixtures (B100PS0, B70PS30, B50PS50, B30PS70, B0PS100 where B=birch and PS=polystyrene and the numbers are the component mass percentage in the feedstock mixture) at 500°C for 30 min.

Figures 3.1.9 and 3.1.10 present thermograms (TG) and derivative thermograms (DTG) for the birch and polystyrene parent material feedstocks. Birch exhibits two mass loss components typical of the depolymerization of hemicellulose (~310°C peak DTG) and cellulose (377°C peak DTG) fractions present in biomass. Polystyrene exhibits a single depolymerization event in a window from 310 to 465°C with peak weight loss at 428°C.

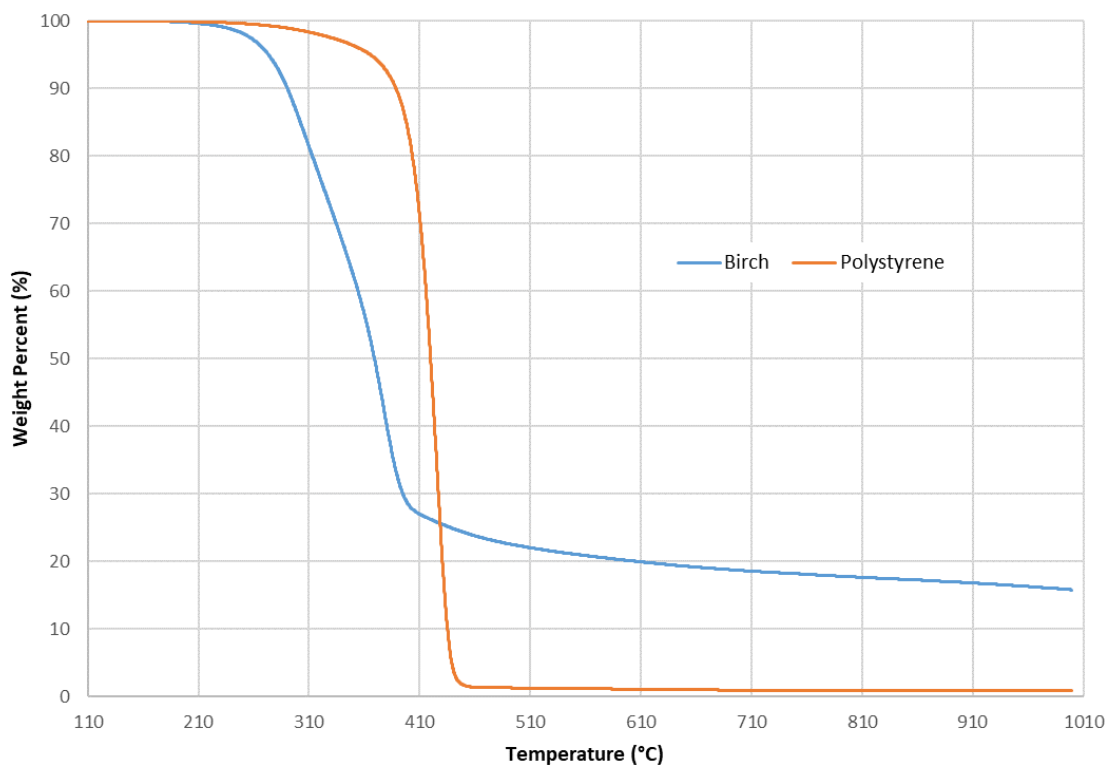


Figure 3.1.9. Thermograms of birch and polystyrene as single components.

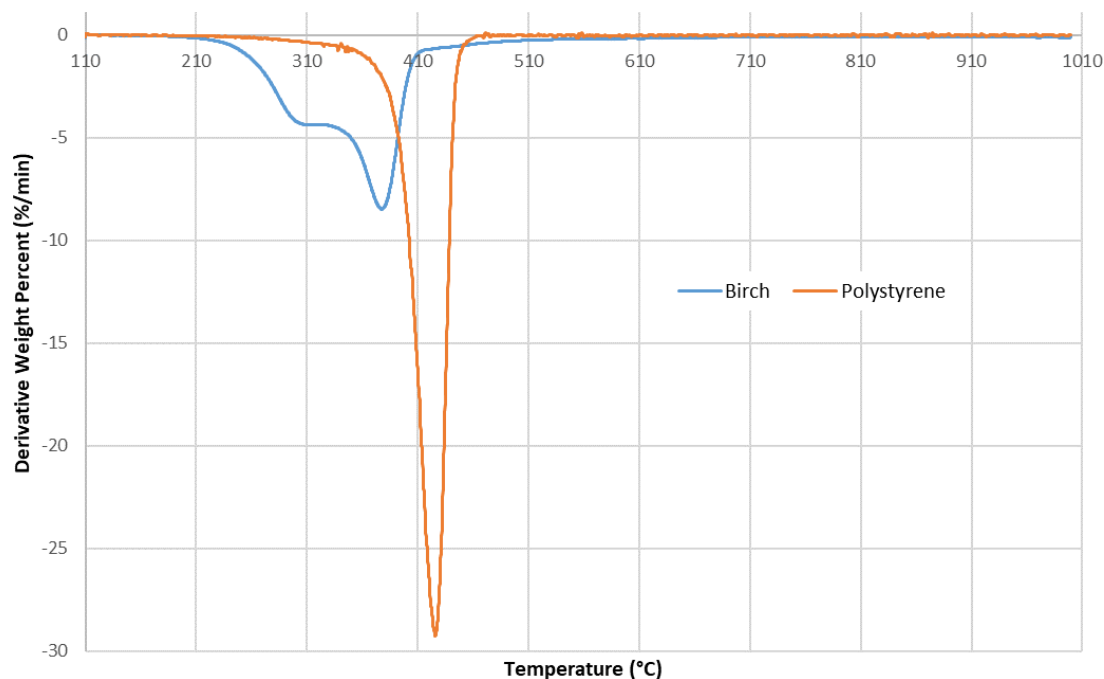


Figure 3.1.10 Derivative thermograms of birch and polystyrene as single components.

Figures 3.1.11 and 3.1.12 present thermograms and their derivatives for the CVC solid products from the BPS test series. Consistent with the proximate analysis in Figure 3.1.8, increasing levels of PS in the feedstock produced CVC solids with increasing volatile matter and the volatile matter

fraction depolymerization is greater at lower temperatures. Maximum rates of mass loss occur at temperatures below 310°C and at a single peak at ~610°C. The lower temperature range has a single maximum of ~190°C for birch and shifts to multiple DTG peaks at higher temperatures with increasing polystyrene feedstock fractions. All CVC samples excepting the B0PS100 share a common DTG maximum at 610°C.

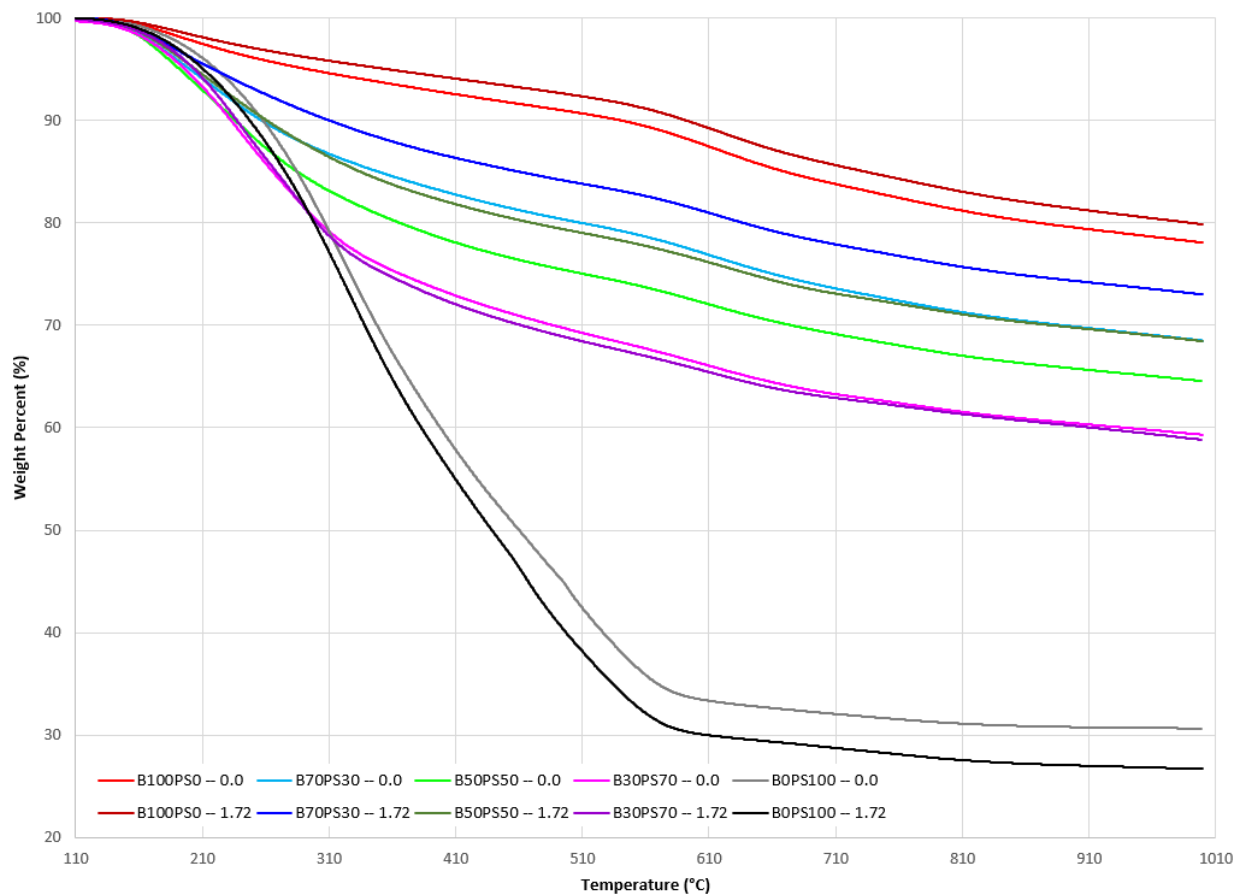


Figure 3.1.11 Thermograms of CVC reaction solids from the BPS experiment series using birch and polystyrene mixtures (B100PS0, B70PS30, B50PS50, B30PS70, B0PS100 where B=birch and PS=polystyrene and the numbers are the component mass percentage in the feedstock mixture and 0.0 and 1.72 are initial reactor pressures in MPa) at 500°C for 30 min.

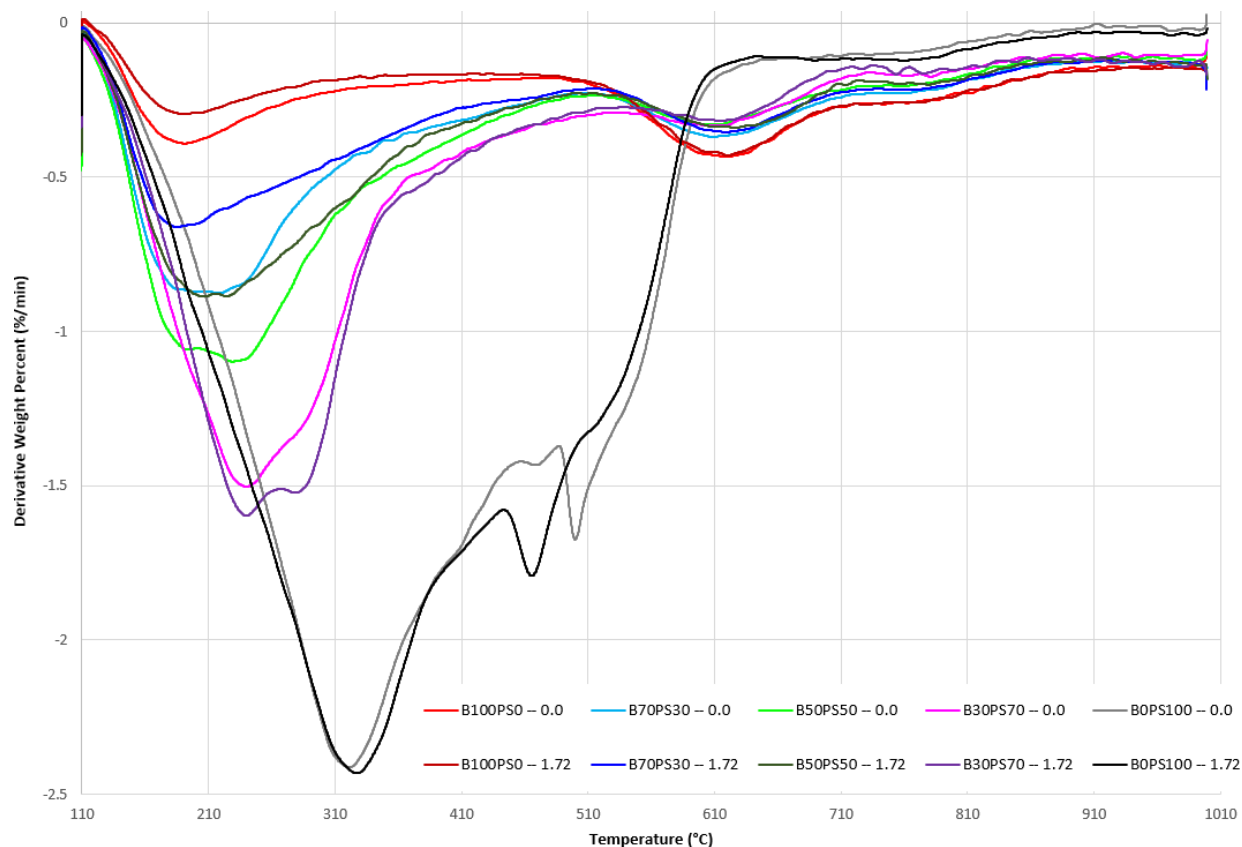


Figure 3.1.12 Derivative thermograms of birch and polystyrene from the BPS experiment series using birch and polystyrene mixtures (B100PS0, B70PS30, B50PS50, B30PS70, B0PS100 where B=birch and PS=polystyrene and the numbers are the component mass percentage in the feedstock mixture and 0.0 and 1.72 are initial reactor pressures in MPa) at 500°C for 30 min..

Perhaps the most important finding from these tests is that the DTG peaks characteristic of the polystyrene parent material and the B0PS100 are not present in the CVC solids from birch-polystyrene mixtures. This suggests that under CVC conditions, the two materials have interacted to form composites with different structures than the parent feedstocks. Initial reactor pressure also has some influence on this structure, with differences in peak mass loss appearing with changes in feedstock mixture ratio and pressure. Future work will use hyphenated TGA-mass spectrometry to better understand the structure of the CVC solids.

In summary, CVC experiments using model waste mixtures show that pressurized pyrolysis can produce a stabilized, aggregated solid product with minimum amounts of free liquid product. The CVC process clearly resulted in a physical transformation of the parent material and modified the polymeric structures of the waste mixture components. Signatures of polystyrene and its degradation products were not present in CVC solids derived from mixtures of polystyrene and birch wood. These findings suggest that the CVC process as a waste management technique warrants further research to understand 1) the underlying physical and chemical mechanisms and 2) how process controls can be used for improve product characteristics.

References

- [1] Legarra, M., Morgan, T., Turn, S., Wang, L., Skreiberg, Ø., & Antal Jr., M. J. (2018). Carbonization of biomass in constant-volume reactors, *Energy & Fuels*, 32, 475-489.
- [2] Legarra, M., Morgan, T., Turn, S., Wang, L., Skreiberg, Ø., & Antal Jr., M. J. (2019). Effect of processing conditions on the constant-volume carbonization of biomass, *Energy & Fuels*, 33, 2219-2235.
- [3] Williams, S., Higashi, C., Phothisantikul, P., Wesenbeeck, S. V., & Antal, M. J. (2015). The fundamentals of biocarbon formation at elevated pressure: From 1851 to the 21st century, *Journal of Analytical and Applied Pyrolysis*, 113, 225-230.
- [4] Van Wesenbeeck, S., Higashi, C., Legarra, M., Wang, L.; & Antal, M. J. (2016). Biomass pyrolysis in sealed vessels. Fixed-carbon yields from avicel cellulose that realize the theoretical limit, *Energy & Fuels*, 30, 480-491.
- [5] Ruppert, W., et al. (2004). *Force provider solid waste characterization study*, Hughes Associates Inc. Baltimore, MD.
- [6] Margolin, J.A., et al., (2015). *Test Standards for Contingency Base Waste-to-Energy Technologies*, Army Research Lab, Adelphi, MD.
- [7] Cui, H. and S. Turn, *Fuel properties and steam reactivity of solid waste streams from contingency bases*. Waste Management, 2018. 78: p. 16-30.

3.2 Marine Fuels

One of the critical issues in for marine fuels is maintaining fuel quality over extended periods of time. Antioxidants have been developed and blended with fuels to improve storage stability. This work conducted comprehensive measurements of the composition and properties of biodiesel derived from waste frying oil (B100 WFO) and investigated the impacts of antioxidant (AO) concentration on its oxidative stability. Biodiesel was used as a model fuel because of its availability from the manufacturer before commercial antioxidants were added and after commercial antioxidants were added. This allowed the preparation of samples across a range of antioxidant concentrations. B100 WFO with antioxidants added was found to have similar physicochemical properties to B100 derived from waste cooking oil and catfish oil. It also demonstrated better oxidative stability due to the AO addition and its lower content of polyunsaturated fatty acid methyl esters (FAMES). Modified ASTM D525 method was employed to study the oxidation process of B100 WFO with 0-0.24%v/v commercial BioExtend™ 30 AO and its impacts on fuel properties. BioExtend™ 30 protected B100 WFO from both degradation and polymerization reactions as demonstrated by the viscosity, density, and cold flow property measurements after 16 and 48 h stress tests, and a higher concentration of AO commensurately extended fuel storage stability.

A manuscript summarizing this work has been submitted to a special issue of the journal *Fuel* organized by the International Association for Stability, Handling and Use of Liquid Fuels (IASH). Articles in the archival literature will be available on HNEI's website upon publication.

TASK 4: RESILIENT ENERGY SYSTEMS

Task 4, Resilient Energy Systems, comprised multiple projects in two areas of research. Under Subtask 4.1, HNEI and its industrial partner, Telos Energy, developed tools and provide analysis of Hawai'i's resource and grid reliability issues. This work focused on providing improved understanding of the impacts of Hawaiian Electric Company's plans to implement utility scale solar-plus storage projects as replacement for the existing thermal generation units. Under Subtasks 4.2, HNEI built upon previous funding and engaged key entities in Hawai'i and the Asia-Pacific region to develop enabling technology for integrating new technology and reliable control at the grid edge, and to conduct comprehensive analysis and planning for the energy systems and critical infrastructure on O'ahu and other Hawai'i Islands to meet DOD's reliability, security, and resiliency needs. The work described in these five subsections was primarily done by HNEI's Grid System Technologies Advanced Research Team (Grid**START**).

4.1 Hawai'i Grid Reliability and Resilience

Prior to 2018, analysis looking at the integration of renewables into the Hawai'i grids was heavily focused on understanding the ability to increase the penetration of variable renewable generation systems without significant curtailment. Prior work utilizing U.S. Department of Energy and Hawai'i State funding included a number of studies (available on the HNEI website) involving both on-island and off-island wind and solar as well as one-way and two-way transmission between the islands.

The focus of renewable energy development in Hawai'i changed significantly when, in January 2019, the Hawaiian Electric Company (HECO) received regulatory permission for seven solar-plus-storage projects comprising over 250 MW of solar and more than one GWh of storage ("Stage 1"). These projects for 'dispatchable variable renewable' generation were made possible by the significant reduction in the cost of grid-scale energy storage, specifically Li-ion batteries.

In early 2020, HECO then selected an additional 16 projects totaling 460 MW of solar and an additional 3 GWh of storage for development ("Stage 2"). With these additions to their grids, the state of Hawai'i and HECO moved to the national forefront of tackling problems associated with high percentages of variable renewable generation.

Figure 4.1.1 shows the expected system-wide production of electricity by resource for the three HECO company systems assuming full buildout of these Stage 2 systems. While there have been delays due to both local technical and global supply chain issues, ongoing planning indicates that the HECO service area will go beyond the penetration levels shown.

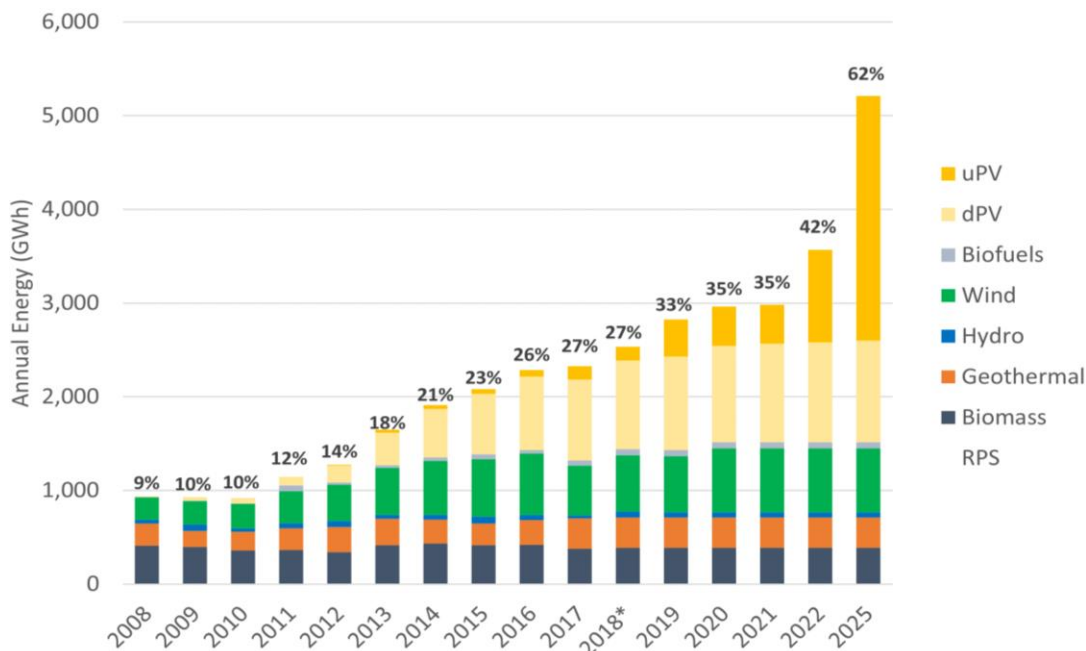


Figure 4.1.1. HECO's expected electricity production, assuming the full buildout of their planned Stage 2 solar + storage projects.

While the availability of cost-effective grid-scale storage alleviated many of the curtailment issues, the geographic isolation of the islands' electricity grids and lack of interconnection between islands makes Hawai'i's challenges of variable renewable integration more pronounced than mainland experience. Specifically, reliability issues, both resource capacity and grid stability can be exacerbated by the relative few, large generating units that make up the thermal generation component of the energy mix. In response to this concern, HNEI and its primary partner in these efforts, Telos Energy, have been actively engaged in developing tools and conducting analysis to better understand the impacts of these significant change to grid operations in Hawai'i.

During the initial period of this award, these efforts focused on the development of new tools to address grid reliability and stability when faced with the stochastic variability of the solar resource. The criticality of these efforts were enhanced due to the, at that time, pending 2022 retirement of the AES coal plant on O'ahu. These activities were cofounded under this award with cost share from the State of Hawai'i. Outcomes from the work have been used by the utility and by the Hawai'i Public Utilities Commission in their decision making. These efforts, summarized briefly below, are described in more detail in a series of project summaries grouped and available at <https://www.hnei.hawaii.edu/publications/project-reports/aprises-17/>.

Stochastic Modeling for High Renewable Grids: As the amount solar and storage integration increases in Hawai‘i, accurately capturing the impact of weather variability and uncertainty is critical. In addition, with the relatively small number of generating units on Hawai‘i’s grid, correlated outages and maintenance of the remaining thermal generation can significantly decrease reliability. The objective of this activity conducted by HNEI, in collaboration with Telos Energy, was to develop novel methodologies and tools to properly evaluate system risk and the likelihood of capacity shortfalls in high percentage renewable grids by probabilistically simulating solar variability, generator outages, and storage availability. A novel methodology to capture the impact of solar variability, generator outage, and storage availability on the reliability of high percentage renewable grids was developed. The methodology captures inherent solar variability, outlier weather events, and the impact of generator outages. A 21-year dataset of solar irradiance and production profiles as well as detailed probability distributions of generator outages and maintenance schedules were developed to allow application of this methodology to the Hawai‘i grids. This new analysis technique helps answer key questions for power system planning that are missed by traditional resource adequacy analysis such as:

- How much solar, storage, and thermal capacity is required to maintain grid reliability?
- What is the effect of increased forced outages and maintenance schedules on reliability?
- How much legacy thermal capacity can be retired?
- How do multi-day low solar and extreme weather events affect reliability?

Integrated Stability and Cost Production Analysis: As the Hawai‘i grids transition to high penetrations of solar plus storage to meet generation needs, conventional stability tools that typically utilize a limited number of snapshots of operations expected, from experience, to show worst-case conditions (i.e. an evening peak load) cannot capture the range of grid conditions that are important to evaluate stability on high percentage-renewable grids. The objective of this activity was to develop a new tool to survey grid stability for every hour over the entire range of operations expected throughout the course of a year. Evaluating grid risk at every hour of the year enables grid planners to understand both the magnitude and duration of risk to the grid, providing valuable context for informing mitigation decisions. A second objective of this activity was to integrate both stability and cost production into one tool, with a significant improvement over traditional tools that cannot co-optimize production cost and grid stability.

The HNEI team has successfully developed a new screening tool that quantifies the stability risk to the grid using a probabilistic approach across all 8,760 hours of grid operation instead of just at preselected conditions of expected risk. This technique yields probability distributions of the frequency excursions for grid events such as loss-of-generation. This new tool provides a more comprehensive means for assessing stability of the Hawai‘i grids as conventional thermal generation is retired and replaced by variable renewables systems. The accuracy of this new tool was calibrated using the full dynamic model of the O‘ahu grid and validated against the typical transmission planning.

Grid Reliability with AES Retirement and O‘ahu Grid Reliability: The AES Hawai‘i coal plant, the largest power plant on O‘ahu, was retired on September 1, 2022. This retirement decreased the amount of dispatchable fossil capacity available to the utility by more than 10%. Throughout 2021 and 2022, the HNEI-Telos Energy team conducted extensive reliability analysis of the retirement to brief HECO, the Hawai‘i Public Utilities Commission (HPUC), and the Governor’s Power Past Coal Task Force on the impacts of this retirement in light of project delays and cancellations of several of the proposed solar plus storage projects. The objective of this study was to evaluate the ability of proposed solar + storage resources to provide the required energy needed while also maintaining grid reliability amid the changes to the thermal generation mix. This work continues today, as is expected to have important implications for power system planning and policy for O‘ahu, and in particular, informing stakeholders on the implications of future fossil fuel plant retirements.

Stochastic analysis, developed earlier in the award, were used to assess capacity reliability risks associated with the AES retirement, updates for utility plans, and possible impacts due to delays in solar project schedules and noted increases in HECO’s generator outage rates (-), the recent failure of Kahe 4 (-), project delays (-), and a reduction in load that occurred with the onset of COVID-19 (+). Analysis shows that with the retirement of AES in September with only one replacement resource available (Mililani I, 39 MW), O‘ahu would experience a modest supply deficit until other Stage 1 and 2 solar + storage resources went online.

Fortunately, although largely past COVID, the O‘ahu peak load remains approximately 100 MW lower than pre-pandemic levels. Subsequent to the end of this APRISES award but during the preparation of this report, updates on reliability expectations were presented to both HECO and to the HPUC. This reduced load is sufficient to mitigate much of the O‘ahu reliability risk through the end of 2022 and into early 2023. With the ever-changing delivery schedules due to both local issues, such as interconnection requirement studies, permitting, and global shipping delays, this work is ongoing and will continue until sufficient resources are deployed to ensure capacity needs for the island are met.

Clean Firm Energy Needs: In addition to concerns regarding resource adequacy as the O‘ahu grid transforms from one which is predominantly thermal generation to one that relies in a large part on variable renewables and battery energy storage to meet demand, there has recently been ongoing discussion and legislative efforts to examine the need for “clean firm energy” to ensure grid reliability (adequate capacity) is maintained. This activity was undertaken to inform both ongoing procurement by the utility and proposed legislation for “firm renewable energy”, better characterized as “dispatchable firm” energy. This analysis sought to determine the minimum amount of firm power that the system would require at various levels of wind, solar, and storage additions. The study is also intended to inform decisions on whether to integrate more variable renewable energy today, considering that these decisions may shut the door on future options. This information can be used to determine characteristics of future systems, to inform decisions on oil-

fired power plant retirements, procurement of new resources, and to quantify robustness issues that might result from a system with variable renewable energy and storage alone.

The results of this study are helping to frame the ongoing discussions, debates, and planning related to the role of firm renewable energy. The findings indicate that on O‘ahu, even with very high penetration of energy from variable renewable energy and storage grid (e.g. over 70% by energy), there is very likely to be a need for firm capacity of 600-750 MW. While the need for capacity remains high, the use of these systems decreases significantly as the penetration of the variable generation increases. In this future clean high-variable energy system, these resources would run sparingly. However, when they do run, it could be for multiple consecutive days at a time. This detailed analysis of firm energy is helping to identify potential resources to provide this unique grid service and help inform recommendations for policymakers, regulators, and grid planners related to the long-term role of firm renewables. As was the situation for the resource adequacy studies, subsequent to the end of this APRISES award but during the preparation of this report, updates on reliability expectations were presented to both HECO and to the HPUC. Work in this area will be continued under future APRISES awards

Further detail on these efforts are available in the “*APRISES 17 Hawai‘i Resilient Systems Projects*” document available at <https://www.hnei.hawaii.edu/publications/project-reports/aprises-17/>.

4.2 Grid Technology Development

Under this subtask, HNEI built upon previous funding and engaged key entities in Hawai‘i and the Asia-Pacific region to develop enabling technology for integrating new technology and reliable control at the grid edge, and to conduct comprehensive analysis and planning for the energy systems and critical infrastructure on O‘ahu and other Hawai‘i Islands to meet DOD’s reliability, security, and resiliency needs. The work described in these five subsections was primarily done by HNEI’s Grid System Technologies Advanced Research Team (Grid**START**).

Coconut Island Microgrid

Coconut Island, also known as Moku O Lo‘e, is a 28-acre (113,000 m²) island in Kāne‘ohe Bay, off the island of O‘ahu and is home to the Hawai‘i Institute of Marine Biology (HIMB), which is part of the University of Hawai‘i. The island is an ideal site for a renewable energy technology-based test bed, particularly representative of an isolated location vulnerable to energy disruption yet serving critical power needs essential to research and educational initiatives.

HIMB has set a goal of making Coconut Island and its research facilities a model for sustainable systems. The island is an inherent microgrid served via an undersea electrical connection tied to a single distribution circuit owned and operated by the local utility on O‘ahu. Its tropical marine features, persistent onshore winds, and exposure to highly corrosive salt spray make it an attractive and unique test bed for microgrid technology. These conditions represent the micro-climate challenges that may be encountered in coastal installations of interest to the Navy.

The Coconut Island DC Microgrid Project was established through previous APRISES funding with the project objective of demonstrating the performance and resilience of a DC microgrid. The project aims to serve loads within two buildings on the island, providing reliable power to critical loads during interruptions and offering clean electrified transportation options that are primarily powered by the sun. Other project goals include:

- Demonstrate innovative new clean energy technologies;
- Reduce island energy dependence upon the local utility and the existing aged undersea electrical service tie, enhancing energy resilience for the selected critical loads;
- Provide a research platform to study DC microgrid resources and loads; e.g., energy storage and supporting technology and DC power appliances, in a tropical coastal environment;
- Increase island energy sustainability; and
- Provide solar electric powered land and sea-based transportation options for HIMB.

The project integrates a DC distribution system into two existing buildings on the island, the Marine Mammal Research Project (MMRP) building and the adjacent Boat House, both of which are depicted in Figure 4.2.1. The energy needs of these two buildings were historically served exclusively by AC power supplied through one of the utility-owned electric service transformers located on the island.



Figure 4.2.1. Location of Coconut Island and the DC Microgrid project site.

Major project activities completed through the support of prior APRISES funding include:

- Project planning and permitting;
- Baseline energy use data metering and collection;
- Developing a conceptual design of the DC microgrid architecture to be integrated with the existing AC building infrastructure;
- Energy use and economic modeling to appropriately size a new rooftop PV system for installation on the MMRP building and a stationary battery energy storage system;
- In collaboration with the Okinawa Institute of Science and Technology and the PUES Corporation (PUES), Japan, specifying, designing, and procuring an electric E-car and E-boat as well as emergency power source powered by swappable BESS units charged via a swap battery charging station to be fed by the DC microgrid;
- Developing and installing two PV systems on the E-boat, one system to charge the swappable batteries on the boat and the other system to power auxiliary loads such as an onboard radio;
- Testing and commissioning the E-Boat, including operational sea trials;
- Performing a due diligence assessment for potential partnering with Sion Electric Co., Ltd. (Sion Electric), a Japanese company with innovative DC microgrid controller technology that has been integrated with stationary BESS, DC powered lighting and air conditioning loads in the course of prior technology development work in Japan. Unfortunately, the collaboration with Sion Electric did not prove to be a feasible option for this project;
- Initiating competitive procurement of the materials and installation services for the MMRP building 6.16 kW DC rooftop PV system to serve as the primary source of renewable energy for the DC microgrid;
- Commissioning the 6.16 kW rooftop PV system on the MMRP building;
- Procuring an 8 kW/8 kWh stationary battery;
- Procuring an AC/DC powered air conditioner and AC/DC LED lighting;
- Developing and procuring the DC microgrid controller and associated enclosures for the control system;
- Developing detailed electrical design drawings of the system;
- Procuring contactors for engineering and electrical systems installation work;
- Installation of three University of Indonesia TREC 2.5 kW DC to DC converter devices that manage voltage and current to power the microgrid DC loads from the 48V DC bus;
- Installation and testing the Blue Ion Stationary Battery System;
- Installation of four Contactor boxes of the Microgrid Control System;
- Installation and programming of the Schneider XW-Pro Inverter and two Schneider charge controllers; and
- Completion of the DC bus wiring.

As noted above, HNEI Grid**START** collaborated closely with PUES, a crucial research partner on the project, to modify, enhance, and install their swappable battery charging station and associated E-car and E-boat. Figures 4.2.2 and Figure 4.2.3 show the installed battery charging station, portable swappable battery energy system (swappable BESS) units, and the E-Boat undergoing sea trials. The 6.16 kW DC rooftop photovoltaic (PV) system installed on the MMRP building is shown in Figure 4.2.4.



Figure 4.2.2. Swap battery charging station and portable BESS units.



Figure 4.2.3. E-Boat in operation in Kāneʻohe Bay, Hawaiʻi.



Figure 4.2.4. DC rooftop PV system installed on the MMRP building.

Under APRISES17 funding, HNEI Grid**START** accomplished the following activities:

- Completed the wiring for the entire system;
- Procured and installed a comprehensive metering system to monitor electrical power flow in the system under both AC and DC configurations (Figure 4.2.5 shows one of the meters and its accessories);
- Installed and tested a new DC to AC inverter for critical plug loads;
- Commissioned the Schneider XW-Pro inverter and two Schneider charge controllers; and
- Completed the commissioning of the electrical components of the microgrid system in a systematic step-by-step approach, with the installation of the microgrid controller being the last remaining step; this commissioning process is described in more detail below. (Figure 4.2.6 illustrates the overall microgrid conceptual design).



Figure 4.2.5. Installed meter to monitor AC and DC power flow.

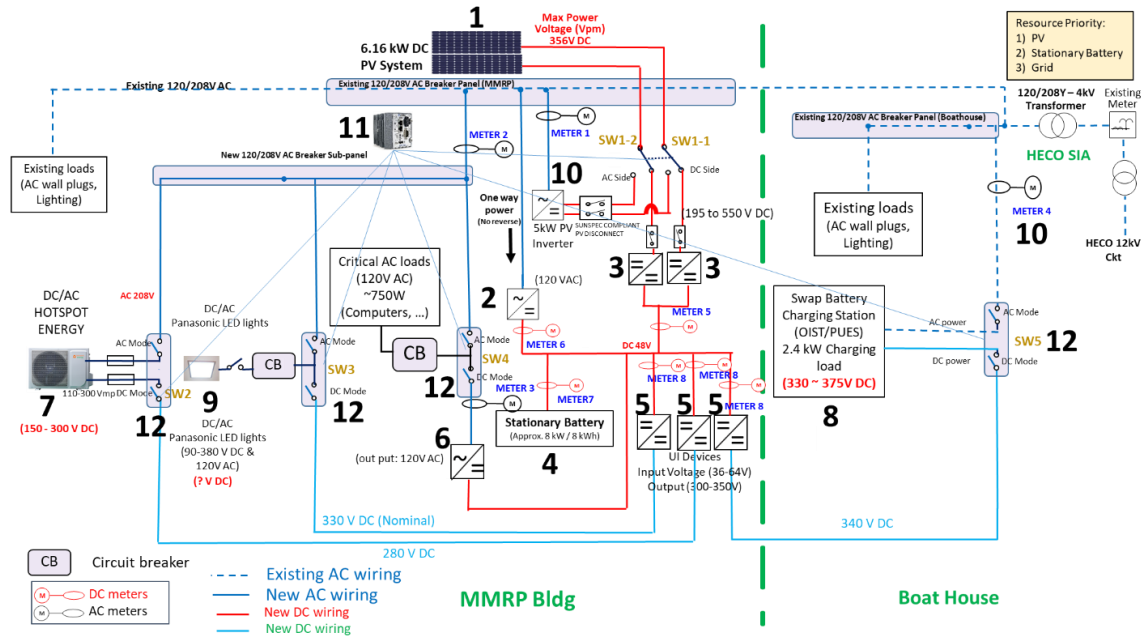


Figure 4.2.6. DC microgrid electrical diagram with the numbered elements described below:

- 1) PV modules installed on the MMRP rooftop as the primary source of renewable energy for the microgrid. The PV system capacity was sized at 6.16 kW DC, which will generate enough energy to support the buildings' targeted loads. PV panels were specified and designed to provide the necessary input DC voltage for effective integration with the DC microgrid controller;
- 2) Rectifier to manage the power provided to the DC bus from the grid;
- 3) Charge controller to manage power to the DC bus from the PV system;
- 4) An 8 kW/8 kWh stationary BESS used to store excess PV energy produced and export the excess energy to the DC microgrid when needed to minimize the use of utility supplied power during normal operation and to maintain service to the specified critical loads in the event of utility service disruption;
- 5) Three University of Indonesia TREC 2.5 kW "DCON" devices that manage voltage and current to power the DC loads of the microgrid from the 48V bus;
- 6) Inverter with a capacity appropriate to supply designated critical AC end-use loads within the MMRP building served by the DC microgrid (e.g., computers, Wi-Fi network, etc.);
- 7) An air conditioning unit that is able to operate with either a DC or AC power source. Its operating performance and efficiency under both DC and AC modes of operation will be assessed and compared;
- 8) A swap battery charging station, designed and manufactured by PUES, will charge the swappable BESS units used interchangeably in the E-boat, E-car and a portable power "suitcase battery" system. This station is capable of charging twelve (12) portable BESS units through the microgrid DC bus. The capacity of each BESS unit is rated at 1.4 kW and 1.4 kWh;
- 9) Interior LED lighting for the MMRP building that will be modified to allow operation with either a DC or AC power source;
- 10) AC and DC metering for performance data capture and analysis;
- 11) Microgrid controller that monitors and controls the operation of the microgrid; and
- 12) Contactor switches to control the mode of operation (AC or DC) of the microgrid.

Due to the complexity of both the power and control systems, a systematic approach was taken in commissioning the system to minimize potential damage to its components. The steps involved in the commissioning process are outlined below.

Step 1 - Commissioning XW-Pro Inverter, Battery, and DC air conditioner: The XW-Pro bidirectional inverter serves as a backup power source from the utility for the DC microgrid in the event that the power from the PV system and battery is insufficient to meet the load demand. The battery stores power from the PV system and provides power to the DC system and the DC air conditioner. Both the inverter and battery were installed and commissioned successfully, performing as expected with the DC air conditioner. The inverter was also utilized to charge the battery using power from the utility, since the PV system was not yet connected to the DC system. This inverter is shown in Figure 4.2.7a.

Step 2 - Commissioning Schneider MPPT Charge Controllers: To power the DC system, two Maximum Power Point Tracking (MPPT) charge controllers were utilized to manage the energy produced by the PV panels installed on the roof of the MMRP building. The configuration of the wires from the PV panels was altered to allow them to switch from providing power to the grid to powering the DC system through the MPPT charge controllers. After successful installation and commissioning, the MPPT charge controllers were programmed to work with the XW-Pro inverter and battery. The system is designed to first charge the battery from the PV system through the MPPT charger controllers if power is available, and then from the grid through the XW-Pro inverter. The MPPT charge controllers are shown in Figure 4.2.7b.

Step 3 - Commissioning LED Lights: The DC power lines and control wires for the LED lights were installed, and after the wiring was completed, the LED lights were tested to ensure that they were functioning properly. The LED lights are shown in Figure 4.2.8a.

Step 4 - Commissioning DC to AC Inverter: A new DC to AC inverter was installed and tested in conjunction with the battery and a plug load. The inverter performed as expected, providing stable power supply to the load. The DC to AC inverter is shown in Figure 4.2.8b.

Step 5 - Testing the Entire System without the Controller: Before integrating the system controller, the entire system was tested for several weeks with all of its components. The power flow monitoring indicated that all components were functioning as expected.

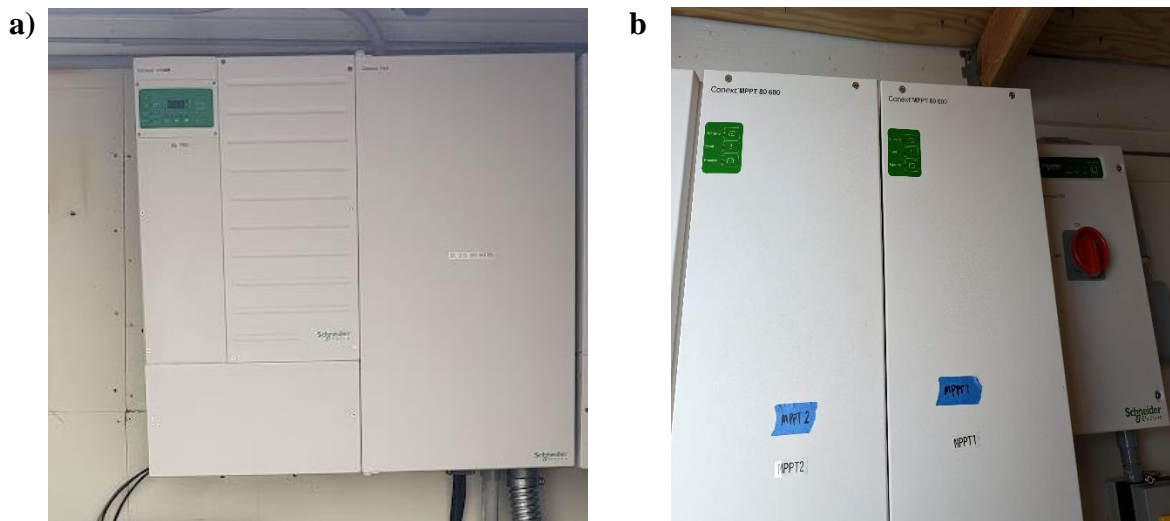


Figure 4.2.7. a) XW-Pro inverter and b) Schneider MPPT charge controllers.

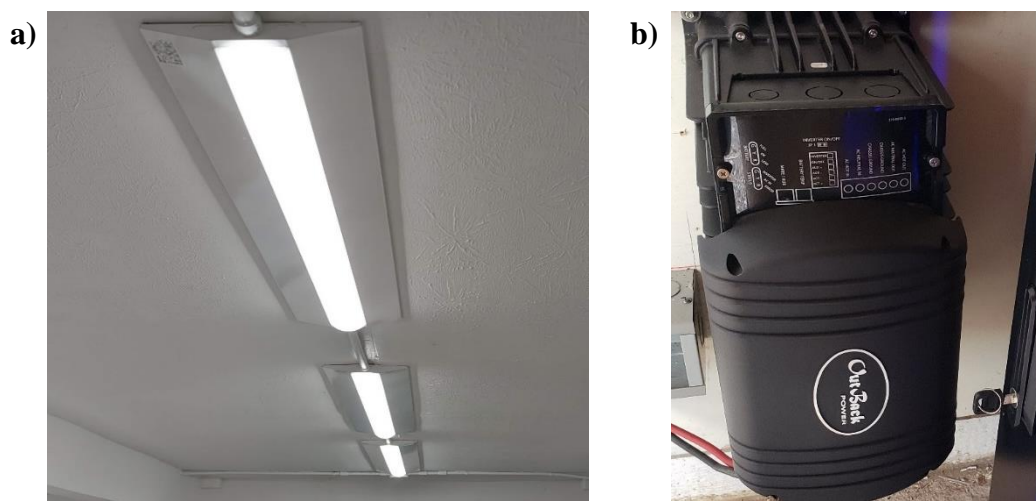


Figure 4.2.8. a) AC and DC LED lights and b) DC to AC inverter.

Under future funding from APRISES, HNEI Grid**START** will complete the system by programming and commissioning the system controller. This will pave the way to move on to the testing and evaluation phase of the research project. HNEI Grid**START** will monitor, characterize, and assess the performance of the DC system in comparison to legacy AC supply. The energy efficiency benefits and limitations of DC operation will be examined, and the sustainability and resiliency advantages of a renewable energy powered DC microgrid and its integration with electrified transportation solutions will be evaluated.

Power Grid Monitoring and Controls

Increasing use of renewable and distributed power generation creates opportunities for customer resources to support power system operations by adjusting power consumption and generation to

address grid needs, based on system-wide and local grid conditions. In particular, grid edge technology has the potential to relieve voltage constraints with local context-aware volt/var control, identify and help mitigate local thermal violations through energy and load shifting, provide data for more refined and readily updated photovoltaic (PV) hosting capacity analysis, identify power quality issues such as harmonic distortion from increasing amounts of power electronic devices, and assist in fault location and anomaly detection, such as pending transformer failure and unmetered loads.

Toward that end, the objective of the Advanced Real-Time Grid Energy Monitor System (ARGEMS) project is to develop a high-performance, low-cost, fully integrated and highly flexible platform for grid power monitoring, data analytics, and controls to provide enhanced situational awareness to utilities and distribution system operators (DSOs) near the edge of the grid; allow tighter, localized, real-time measurement, coordination and control of distributed energy resources (DER) such as PV; and ultimately support the reliable, resilient and sustainable integration of higher DER penetrations. ARGEMS encompasses custom board-level hardware, drivers, and application-level software; methods to gather, report, process, store, and respond to measurements from the built-in power quality meter or external meters and DER, as well as to control DERs; and web-enabled interfaces and application program interfaces (APIs) for real-time and historical data retrieval, visualization, and other interaction. As a result, ARGEMS has the potential to provide significant advancements in these areas beyond the commercial state of the art. APRISES17 was the final funding period for the project, and commercialization is now being pursued outside HNEI.

ARGEMS can be programmed to support a wide variety of use cases. It offers high-fidelity voltage and current measurement, numerous communications options, low-latency event-driven messaging, precise GPS-based timing, backup power supply, and powerful processing for real-time data analysis — all in a small weather-resistant enclosure. It provides high-fidelity, low-latency measurement by utilizing carefully selected technology at the intersection of Internet of Things (IoT), radio frequency (RF) mesh communications, open source software, single board computers, and off-the-shelf integrated circuits (ICs) for the power quality meter analog front end (AFE), field programmable gate array (FPGA), GPS, and power management.

ARGEMS development, initiated under prior APRISES funding, has continued for several years and has now transitioned from conceptualization and fundamental hardware and core software development, to use cases and applications of the system involving analytics, modeling, and/or controls for in-field deployment, test and evaluation. The project has enabled and fostered new collaborations, funded research, and outreach. Research has included distributed volt/var control, optimal electric vehicle (EV) scheduling and charging, and novel methods of fault location. Fourteen undergraduate students and eight international interns have been involved in the project. ARGEMS devices have been successfully deployed at the UH Mānoa campus, Arizona State University, Chulalongkorn University (Thailand), and in Okinawa, Japan. The platform has shown the flexibility to serve the objectives of multiple research projects among HNEI and its partners

while also gaining commercial interest for grid operations. In particular, ARGEMS has been used in the following projects of HNEI Grid**START** using APRISES funding:

- *Automated Distribution Circuit PV Hosting Capacity Estimation*: Work included use of the core computer and ultimately the power measurement capabilities to model and estimate distribution power flow for in-situ PV hosting capacity analysis.
- *Real-Time Health Assessment of Distribution Transformers*: The electrical/thermal transformer model has been implemented in real time, using power measurements, to estimate transformer core temperature as a stress indicator. Work included incorporating temperature and vibration sensors in an external module for additional insight into transformer health.
- *Conservation Voltage Reduction (CVR) Demonstration*: A device is installed in Okinawa, Japan to record power measurements and control two Fronius inverters for reactive power injection according to HNEI's CVR algorithm. This has also been an opportunity to validate its voltage readings against the well-established PQube3 commercial instrument.
- *Hawai'i BESS + PV Virtual Power Plant Demonstration*: Four power monitors have been installed in a larger data acquisition box to measure eleven channels of power flow and implement algorithms for economic optimization of battery energy storage for customer and grid services.
- *Coconut Island DC Microgrid*: The core computer (without power measurement circuitry) is retrieving and reporting DC and AC power metrics from an SMA inverter every four seconds for purposes of performance analytics.
- *Advanced Power Systems Laboratory*: The core computer (without power measurement circuitry) is retrieving and reporting AC power metrics from four Fronius inverters every four seconds.
- *Bi-Directional EV Charging Demonstration Project*: A device has been installed with capability to run charge optimization algorithms and also as a field test of the hardware reliability. This project uses some of the programs and functions for data messaging, storage, and web presentation.
- *Distributed PV Inverter Control for CVR*: ARGEMS was used for distributed PV inverter control for CVR under an Office of Naval Research (ONR) Defense University Research-to-Adoption (DURA) project led by Arizona State University (ASU), with HNEI as a sub-awardee.
- *PEA Internship*: Under HNEI's ONR-funded APRESA project, ARGEMS is a basis for research collaboration and field deployment with Chulalongkorn University (Thailand) and a Thai distribution utility, the Provincial Electricity Authority (PEA) of Thailand. In particular, six engineers from PEA visited HNEI for an eight-week internship in 2020 and studied three different use cases that could be implemented on the platform.

The project background, original motivation, several rounds of prototype development, and web interfaces were covered in the APRISES14 report. The project achieved its original goal of establishing a low-cost, high-fidelity power monitor. Key specifications were provided in that report and remain unchanged, but a relatively minor hardware redesign was performed under APRISES15 funding to fix issues with the backup power supply and LTE modem, as well as to add an interface for a Landis+Gyr wireless mesh node and migrate to a graphic LCD display to show more information in the field. After additional improvements primarily for manufacturability, 25 devices were produced. Ten of these were funded by and delivered to ASU's DURA project (described above). Most of the printed circuit board (PCB) manufacturing and assembly was performed by MacroFab, Inc. (Houston, TX); this was the first time the production was outsourced to industry.

Under APRISES15 funding, ARGEMS software modules were added to gather data from SMA inverters and the Tesla Energy Gateway 2. Also, under APRISES15 funding, the device was featured in ThinkTech Hawai'i, at the SOEST Open House, and UH Sea Grant's Voices of the Sea.

A U.S. patent was awarded to the University of Hawai'i on the system in October 2021. Discussions regarding potential use cases and demonstrations have been held with utilities in Hawai'i, Alaska, and Thailand. The software stack is now well-documented and tested. Onboard power flow simulation capabilities have been established. The printed circuit board (PCB) design is well-refined. Commercial assembly indicated that costs are competitive with traditional distribution service transformer monitors.

During this funding period, HNEI Grid**START** added and deployed software interfaces on the ARGEMS to monitor and control additional devices, improved the volt/var control algorithms, and improved the reliability and command line interface of the system. Documentation and training content were also developed and improved.

The ARGEMS hardware and software were designed to serve specific research needs and opportunities in renewable energy integration at HNEI, while also considering that the technology could be commercialized in the future. The device and system will be maintained for use on other projects, but no further active development by HNEI is expected. Dr. Kevin Davies, the lead developer of ARGEMS, left HNEI in June 2022 to explore the commercialization of ARGEMS, among other opportunities. The commercialization effort is under Renewable Edge LLC, a limited liability company registered in Hawai'i. The company has engaged in several business incubation, customer discovery, and pre-SBIR development programs. Of note is that a report by RTI International (www.rti.org) identified strong commercial potential in the area of advanced distribution transformer power monitoring.

Solar Forecasting

Solar technologies provided much of the newest capacity to the United States' grid in recent years. According to the Solar Energy Industries Association (SEIA) Solar Market Insight Report 2022 Q3, the U.S. solar market installed 4.6 GW_{dc} of solar capacity in the second quarter of 2022, which is a 12% decrease from the same period in 2021, but a 12% increase from the first quarter of 2022. Despite the decrease, solar accounted for 39% of all new electricity-generating capacity added to the U.S. grid in the first half of 2022. The solar industry is presently facing supply chain constraints and trade policy issues, which have suppressed growth. The Inflation Reduction Act, passed in August 2022 is expected to be a growth catalyst for the solar industry, with total solar deployment expected to increase by 62 GW_{dc}, or 40%, over the next five years [1].

Continued solar capacity growth is especially important for the State of Hawai'i. Hawai'i is the most petroleum-dependent state with the highest average electricity retail price. However, plentiful solar insolation and high electricity cost have also made Hawai'i an ideal solar market, and it was the first state to reach grid parity for PV systems.

Power output from PV systems is directly related to the power of the radiation striking the panel or irradiance, defined as the radiant flux per square meter. At high penetrations, irradiance variability causes fluctuations in PV production, increasing the difficulty of balancing power and regulating grid stability, while the uncertainty of upcoming PV production complicates reserve management and can lead to inefficient grid operations. PV interconnection issues in Hawai'i are particularly problematic, as each island maintains its own isolated electric grid.

Irradiance variability is driven by both extraterrestrial and atmospheric effects. Top of the atmosphere (TOA) irradiance varies with sun-earth geometry and changes in solar output that occur on the nearly periodic 11-year solar cycle. As downwelling radiation passes through the atmosphere, it is attenuated through a complex series of reflections, absorptions, and reemissions due to interactions with air molecules, and atmospheric particles and particulates [2]. The key step in solar resource prediction is assessing the state of the atmosphere [3].

The goal of this project is to develop methods and technologies that reduce the uncertainty of solar power generation. Project activities include research to capture and characterize solar resource variability and the development of solar forecasting methods and technologies.

Under previous APRISES funding, HNEI developed an operational solar forecasting system for the Hawaiian region. The system generates probabilistic forecasts using ensemble techniques that combine overlapping forecasts from separate forecasting components, such as sky images, satellite images, and numerical weather prediction (NWP). This approach allows for predictions of irradiance or PV power output over a range of timescales, from minutes to days ahead. The approach also allows flexibility in the generation frequency and temporal resolution of output

products. The system was also designed to forecast distributed solar systems. The system can quickly generate forecasts for numerous PV systems that vary in size, type, and orientation.

The HNEI solar forecasting system is fully automated, producing operational forecasts without human intervention. The automation is controlled by the Forecast Management and Visualization System (FMVS), which is responsible for monitoring the state of the forecasting system, sending email alerts if problems are detected, transferring data to internal and external sources, and displaying real-time predictions and observations using web-based tools. The FMVS also monitors computational resources (tasks are run on three rackmount servers) and controls the timing of new processes using a queue system. Development and testing of the operational forecasting system was completed in the fall of 2020 and has generated operational forecasts without interruption since.

Under APRISES17 funding, HNEI has developed new methodology to allow for improved modeling and prediction of irradiance under clear-sky conditions. Modeling irradiance under clear-sky conditions is a crucial first step in solar resource prediction.

The definition of clear-sky conditions varies. The more common definition is a state in which there is an absence of clouds in the sky dome [4], but under this work, a more appropriate definition is a state in which clouds are not affecting the solar resource or resulting PV power production. Under clear-sky conditions, the attenuation of downwelling irradiance is primarily modulated by the state of aerosols, particulates suspended in the atmosphere ranging in size from 1 nm to 5 nm, and atmospheric water vapor [5-6]. Aerosols originate from both natural and anthropogenic processes. Common aerosols include salts from air-sea interaction, smoke and soot emitted from fires, ash and dust erupting from volcanoes, sulfates from burning of coal and oil, and black carbon released during combustion of heavy petroleum. The state of aerosols and atmospheric water vapor is influenced by photo-chemical activity, local emissions, mesoscale circulation, wind ventilation, and atmospheric temperature [7]. Clear-sky attenuation can be quantified using broadband turbidity indices, such as the Linke turbidity factor (TL), a unitless index that incorporates the optical depth of aerosols, combined with the optical depth of water vapor [8].

Numerous methods have been developed to quantify local atmospheric turbidity conditions for use in clear-sky models. These methods require observations of atmospheric conditions which capture clear-sky conditions, be it from remote sensing or in situ instrumentation. Current satellite-based methods rely on data from polar orbiting platforms, which severely limits temporal sampling. Ground-based methods can provide increased temporal sampling, with current methods requiring instrumentation that directly measure the direct or diffuse component of irradiance [6, 8-9]. Such instruments are relatively expensive (\$30,000) and contain moving parts to either track or block the sun, which require routine maintenance, cleaning, and calibration and limit the lifetime of the instrument. Because of this, operational instruments producing real-time are rare, and HNEI is not aware of any instruments currently operational in Hawai‘i.

These factors motivated the development of a new method to estimate turbidity conditions from pyranometer measurements, or directly from PV power output data. Pyranometers have become a standard radiation measurement instrument, providing the most readily available type of standardized solar radiation data globally. Also, near-real-time data from distributed PV systems is becoming increasingly available through sharing services such as pvoutput.org. However, quantifying atmospheric turbidity from pyranometer measurements is problematic. A few methods have been proposed using archived pyranometer observations, but with limited application. Pyranometers measure global irradiance, which has a dampened turbidity signal due to an exchange between the diffuse and direct components of irradiance; diffuse irradiance varies with turbidity, while direct irradiance varies inversely with turbidity.

The turbidity estimation method is computationally inexpensive and designed to provide near-real-time information for operational solar nowcasting and forecasting applications. The method utilizes a long short-term memory (LSTM) recurrent deep neural network (DNN) to model the complex non-linear relationship and extract the dampened signal. The DNN acts as a separation model, extracting diffuse and direct components of irradiance. The DNN ingests clearness index and clear-sky index values derived from pyranometer or PV power data using a clear-sky irradiance model combined with a PV simulation tool. Periods of clear-sky conditions are identified using a clear-sky classification algorithm which can ingest either pyranometer or PV power data. Turbidity is then estimated using an inversion of the Ineichen and Perez direct irradiance model.

Figure 4.2.9 shows sample day of method input (A) and method output (B through E). DNN feature inputs are shown in Figure 4.2.9B. DNN-derived diffuse and direct components of irradiance are shown in Figure 4.2.9C and D, respectively. DNN-derived turbidity estimates (occurring during clear-sky conditions) are shown in Figure 4.2.9E. Data used to validate the method is also shown in Figures 4.2.9C through E.

The method, and validation of the method, is discussed further in: Matthews, 2023 (see the Publications and Presentations section at the end of this subtask).

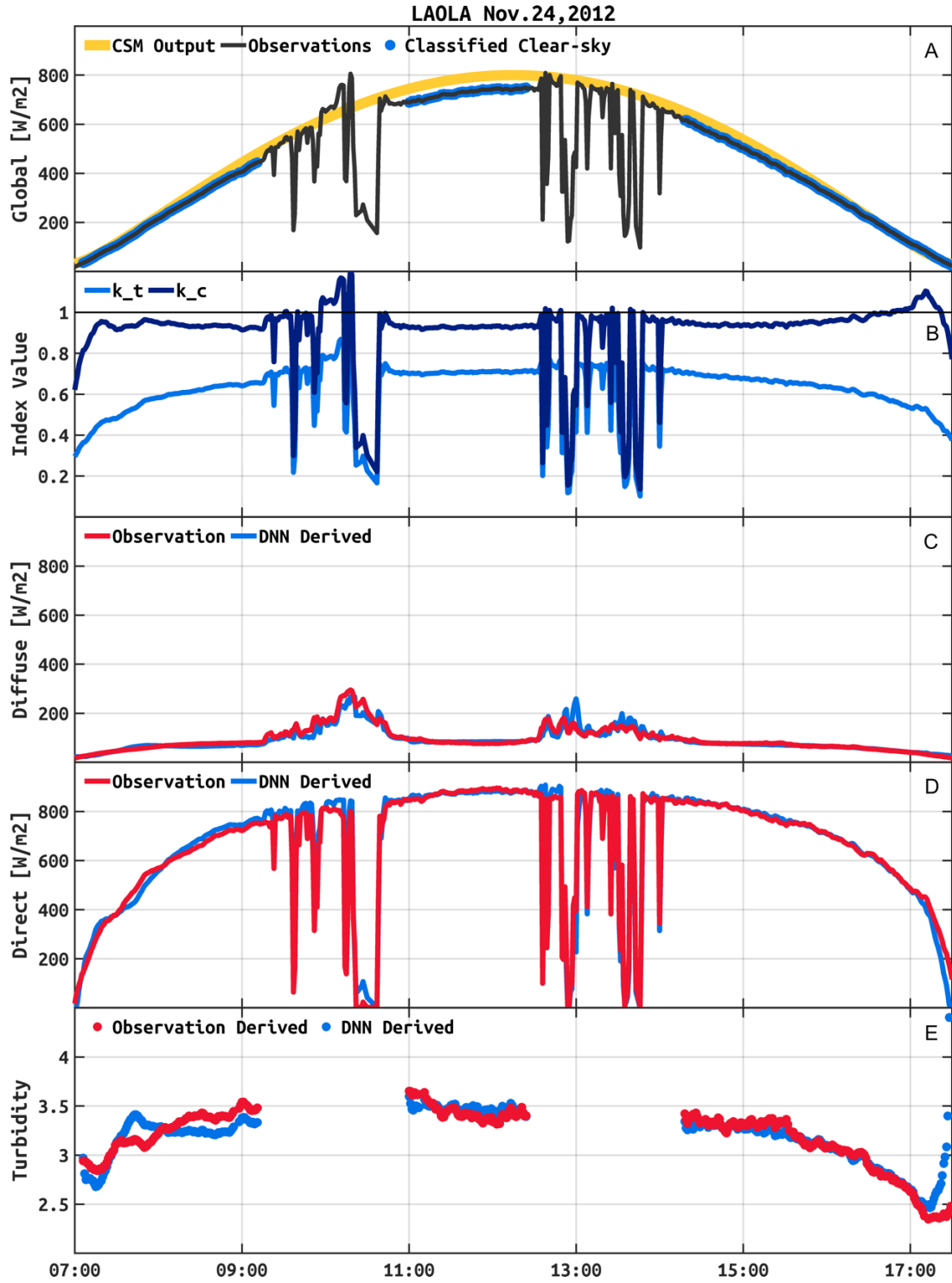


Figure 4.2.9. A sample day of method input, method output, and validation data from the La Ola Solar Farm on the island of Lānaʻi.

In this work, we apply and validate the method using horizontal pyranometer data from the island of Oʻahu (spanning 1.5 year), horizontal pyranometer data from the island of Lānaʻi (spanning 3

years), and plane of array (POA) pyranometer data and PV power output data from the island Maui (spanning 2.5 years). Key results of the validation include:

- DNN-derived diffuse irradiance replicated Rotating Shadowband Radiometer (RSR) measurements with errors of: 43.2 W/m² RMSE (5.3% nRMSE) and 2.9 W/m² MBE (0.35% nMBE) when ingesting horizontal pyranometer data, 45.2 W/m² RMSE (6.06% nRMSE) and 2.07 W/m² MBE (0.28% nMBE) when ingesting POA pyranometer data, and 50.87 W/m² RMSE (6.8% nRMSE) and -0.35 W/m² MBE (-0.05% nMBE) when ingesting PV power data;
- DNN-derived direct irradiance replicated RSR-derived measurements with errors of: 71.2 W/m² RMSE (6.5% nRMSE) and -1.93 W/m² MBE (-0.17% nMBE) when ingesting horizontal pyranometer data, 66.7 W/m² RMSE (5.69% nRMSE) and -5.2 W/m² MBE (-0.44% nMBE) when ingesting POA pyranometer data, and 119.7 W/m² RMSE (10.2% nRMSE) and 11.9 W/m² MBE (1.01% nMBE) when ingesting PV power data;
- The DNN performance was compared against six standard separation models and demonstrated RMSE reductions of 43% to 60% for diffuse irradiance and 39% to 54% for direct irradiance; and
- DNN-derived turbidity estimates replicated RSR-derived turbidity estimates with errors of 0.33 RMSE (6.89% nRMSE) when ingesting horizontal pyranometer data, 0.39 RMSE (8.33% nRMSE) when ingesting POA pyranometer data, and 0.46 RMSE (8.51% nRMSE) when ingesting PV power data.

Conservation Voltage Reduction Demonstration

The primary goal of the project is to demonstrate energy efficiency through advanced Conservation Voltage Reduction (CVR) on a section of the distribution circuit that supplies the Plaza Housing complex at U.S. Marine Corps (USMC) Camp Foster in Okinawa, Japan. This project involves the development of technology, field implementation, testing, and evaluation of grid improvement technologies.

Working in close collaboration with USMC Facilities personnel in Okinawa, a 13.8 kV distribution circuit called “Feeder F6A” was selected for the CVR demonstration. This single feeder has approximately 56 distribution service transformers and is fed by a large substation transformer that provides power to a total of ten feeders. To achieve the project objectives while keeping the project within its research scope, budget, and implementation scale, a section of the Feeder F6A that serves the Plaza Housing complex was identified for the CVR control. The CVR-controlled feeder section was isolated with a voltage regulator (VR) to manage and control the voltage at “downstream” service transformers, essentially behaving as the load tap changer on a substation transformer for the limited section of the feeder under test.

Specifically, seven distribution service transformers located at a branch end of Feeder F6A were identified for the CVR demonstration. Five out of the seven distribution service transformers already had existing advanced metering infrastructure (AMI) meters and communications installed. A new distribution pad-mounted VR, in conjunction with near real-time voltage recordings taken at the transformers and communicated back to the VR controller, regulates the primary voltage of these seven service transformers. In turn, the VR will manage the customer service voltages to the lower limit of the $\pm 5\%$ acceptable ANSI voltage range. A reduction in energy consumption in the range of 0.7% to 0.9% for every 1% reduction in voltage is expected. This reduction in energy consumption is the primary value proposition of effective CVR implementation — reduced energy use by more effective management of customer service voltage.

Figure 4.2.10 below shows an electrical one-line schematic of the project area. The existing electrical infrastructure integrated with new technology deployed under this project includes the new VR and its HNEI Grid**START** developed controls (with associated bypass switch) located at GS 32, seven distribution service transformers powering an array of loads representative of those normally found on a military base (e.g., Officer's club commercial load, troop barracks, and residential housing), metering at service transformers and AMI radio network communications, an HNEI developed reactive power voltage management source and controller installed at TH 415, and a 5 kW rooftop PV system located on a building served from TH 415.

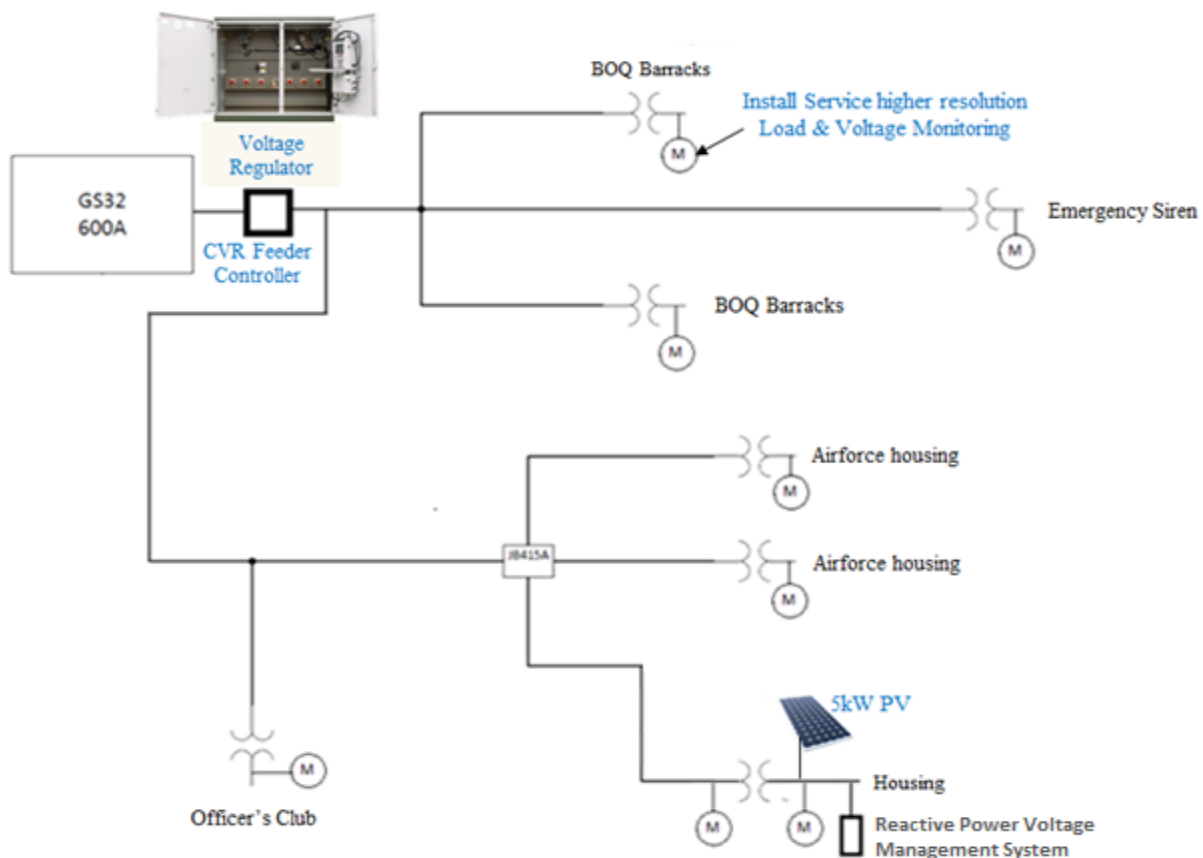


Figure 4.2.10. Project demonstration area electrical one-line schematic.

Under APRISES14 funding, the proposed CVR control algorithm and the associated communications between the field meters and the CVR controller were validated utilizing the hardware-in-the-loop (HIL) test platform in HNEI's Advanced Power System Laboratory. In addition, a user-interface was developed to provide USMC Okinawa personnel with information about the status of the VR and HNEI controller. Webpages hosted on the HNEI controller allow for remote monitoring of the system. The HIL testing and user interface were discussed in more detail in the APRISES14 Final Technical Report.

Working closely with USMC Okinawa base personnel, HNEI also completed the electrical installation drawings and developed the bid package for the final construction and field installation work for the VR and bypass switch installation and all associated electrical ties. The bid package was issued, and a construction contract was awarded. To ensure that the VR installation, site acceptance testing, and equipment commissioning would be performed properly, HNEI carefully defined the scope of work for this element of the project execution in close collaboration with Eaton, the manufacturer of the VR and bypass switch.

The construction services that were initially scoped and procured under APRISES14 were essentially completed under APRISES15, except for the final commissioning work due to COVID-19 travel restriction delays, as discussed further below. Fortunately, with the strong support of USMC GF Facilities Engineering Division of Camp Butler, HNEI was able to obtain the services of Seabees companies deployed to Okinawa. Field construction work on our project was utilized as a part of their training on building electrical infrastructure. HNEI obtained all the required building materials, and the Seabees provided the labor to install the underground electrical conduits and concrete pad required for the installation of the VR and bypass switch (Figure 4.2.11). The installation required the coordination of multiple system power outages, with each outage required to be on a Monday unless it conflicted with a holiday or an Officer's Club event. Furthermore, consecutive outages had to be scheduled at least two weeks apart. These limitations, along with a rotation of Seabee companies during the work, resulted in some scheduling challenges; notwithstanding, the infrastructure work was completed by the Seabees in February 2020.



Figure 4.2.11. Seabees working to install the conduits and concrete pad.

Once the electrical infrastructure was installed, HNEI's electrical contractor was able to reconfigure the distribution circuits coming from GS 32 to incorporate the VR and bypass switch into the distribution system serving the seven transformers (Figure 4.2.12).



Figure 4.2.12. HNEI's electrical contractor installing the electrical cables and terminations.

The electrical contractor's work, which overlapped slightly with the Seabees' fieldwork in February 2020, was completed in March 2020 with the installation of the VR and bypass switch

(Figure 4.2.13). Unfortunately, as the electrical work was being completed, the global COVID-19 pandemic was accelerating, resulting in severe restrictions or prohibitions on international travel. Due to the extended travel restrictions, HNEI Grid**START** was unable to travel to Okinawa to commission the VR and place it into service until March 2022 when travel restrictions were finally eased.



Figure 4.2.13. Installed VR and bypass switch.

During and after the installation of the VR, HNEI Grid**START** continued its research partnership with USMC GF Facilities Engineering Division, addressing issues related to the USMC's existing AMI mesh communication system that will be used for data transfer and control by the CVR system. The communication issues were suspected to stem from salt air corrosion of the antennas at some of the existing AMI meter sites. HNEI Grid**START** contracted with another important partner on this project, Okinawa Enetech, to replace and weatherize the problematic antennas. These repairs (Figure 4.2.14) were successful in fixing the communication issues.

TS 4029

- ✓ Replacement of Antenna and Coax Cable
- ✓ Weatherproofing



Figure 4.2.14. Example of the antenna replacement work.

The project faced several challenges due to failures of the pQube meters that were installed to measure the voltage at each transformer. The pQube manufacturer suspected that the failures were due to condensation-induced moisture build-up in the meter enclosure (a function of the humid tropical environment in Okinawa), which caused supercapacitors in the pQube meter to corrode and fail. The pQube meters were tested to see if they could operate without supercapacitors to eliminate the mode of failure. It was determined that the pQubes would operate sufficiently without the supercapacitors, and the pQube manufacturer agreed to remove the supercapacitor from spare meters that HNEI Grid**START** had in its inventory. In addition, a small adhesive strip heater was installed in the meter enclosures to drive out condensate in the box and reduce the likelihood of further pQube failures.

Under APRISES17 funding, HNEI Grid**START** engaged Okinawa Enetech to implement the pQube meter exchange and heater installation (Figure 4.2.15). Once the COVID-19 travel restrictions were eased, HNEI Grid**START** was able to travel to Okinawa, utilizing the Status of Forces Agreement (SOFA), to commission the VR and place it into service (Figure 4.2.16).



Figure 4.2.15. PQube enclosure with modified PQube and heater element installed.



Figure 4.2.16. VR Commissioning.

HNEI Grid**START** personnel also field installed and operationalized the CVR system controls, enabled all system communications, and initiated full operation, testing, and initial evaluation of the CVR system (Figure 4.2.17).



Figure 4.2.17. VR control cabinet with HNEI Grid**START**'s embedded communication and control systems.

Finally, under APPRISES17, HNEI commissioned, tested, and operationalized the reactive power voltage management hardware and control systems installed at the TH-415 transformer connected to the 5 kW PV system. Figure 4.2.18 shows reactive power being dispatched from one of the inverters that comprise the voltage management system.



Figure 4.2.18. Advanced CVR Device Dispatching Reactive Power.

Now that the VR and reactive power voltage management systems have been commissioned and the control systems for both operationalized, the performance evaluation portion of the project can proceed. Under future APRISES funding, the operation of the advanced CVR system will be evaluated, and its energy conservation benefits will be determined and presented to the USMC command for decision-making on broader CVR implementations.

Advanced Power Systems Laboratory

HNEI's Grid**START** is nearing construction completion of its new Advanced Power System Laboratory (APSL), a state-of-the-art facility for conducting hands-on research on renewable energy integration in a real-time simulated grid environment. The APSL is located within the University of Hawai'i Marine Center (UHMC) at Pier 35 in Honolulu Harbor. Once operational, the APSL will be a highly flexible and unique power system research facility in Hawai'i, capable of testing AC and DC equipment, systems and microgrid technologies, in a field representative and precisely controlled electrical environment.

In addition to locally supplied grid power feeding the lab, the lab architecture also includes a 35.3 kW rooftop photovoltaic (PV) system directly tied into the lab room and connected to four advanced PV inverters with grid support functions, all serving three AC/DC equipment test bays. The architecture also features a real-time grid simulator connected to a 30 kVA power amplifier, known as a power hardware-in-the-loop (PHIL) configuration. The PHIL configuration enables evaluation of electrical power equipment as units under test (UUTs) in a simulated grid environment. Figure 4.2.19 below illustrates the main components of the APSL architecture.

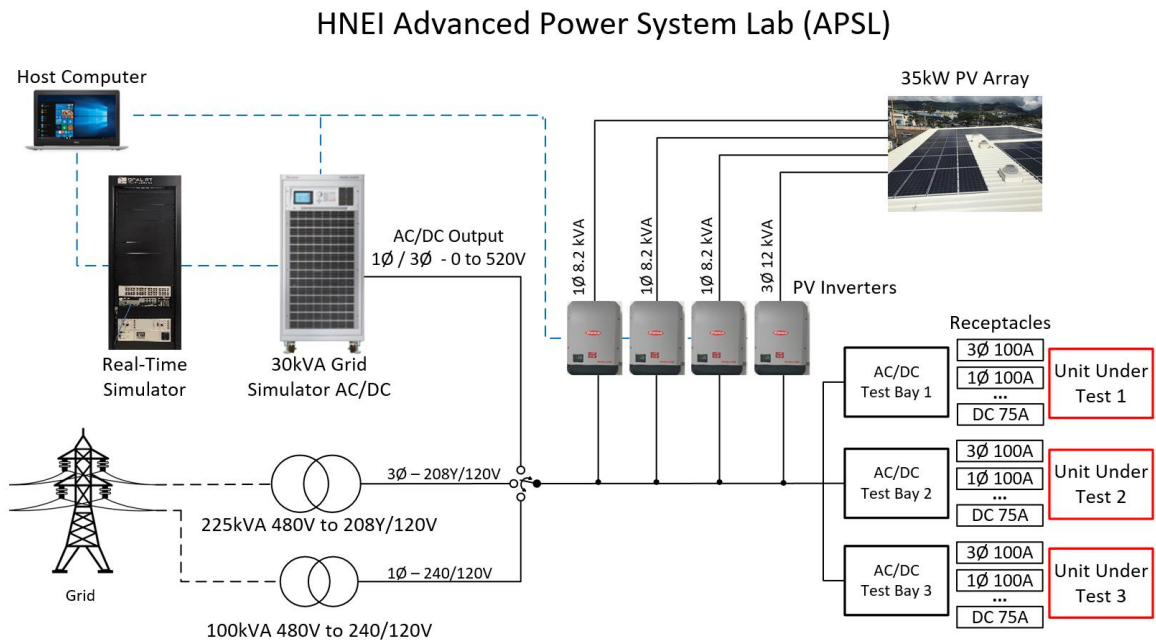


Figure 4.2.19. HNEI Grid**START** Advanced Power System Lab architecture.

The lab architecture includes three modular test bays for evaluating advanced functions, communications, and controls of various UUTs such as, but not limited to:

- advanced function PV inverters;
- electric vehicle (EV) chargers, including vehicle-to-grid (V2G) and vehicle-to-home (V2H) enabled chargers;

- battery energy storage systems (BESS);
- power monitoring and edge computing devices;
- AC or DC loads/appliances and load control devices; and
- voltage management devices.

Each test bay in the APSL will be equipped with outlets of different voltages and currents (Figure 4.2.20), including 3 Φ 208Y/120 V grid-tied, 1 Φ 240/120 V grid-tied, 3 Φ 0~520 VLL Grid Simulator, and 600 V_{DC} off-grid.

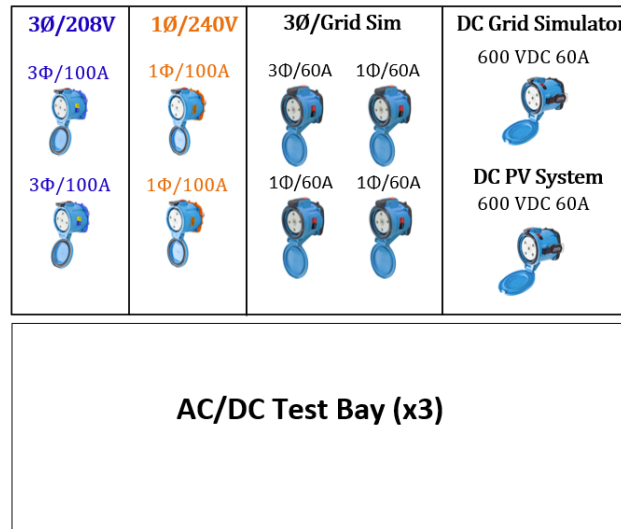


Figure 4.2.20. AC/DC Test Bay conceptual design.

The lab architecture features an off-grid DC test bed rated at 600 V_{DC} that can be accessed in all three test bays. The test beds include two 600 V_{DC} buses — one powered by the lab’s PV system, and the second by a Chroma 61830 grid simulator in DC mode. There is also an AC test bed consisting of the following three AC test buses:

- 1) 1 Φ /3 Φ 0~520 VLL_{AC} grid simulator bus served by the Chroma 61830 grid simulator (Figure 4.2.21);
- 2) 3 Φ 208Y/120 V_{AC} bus served by a 225kVA transformer (Figure 4.2.22); and
- 3) 1 Φ 240/120 V_{AC} bus served by a 100kVA transformer (Figure 4.2.23).

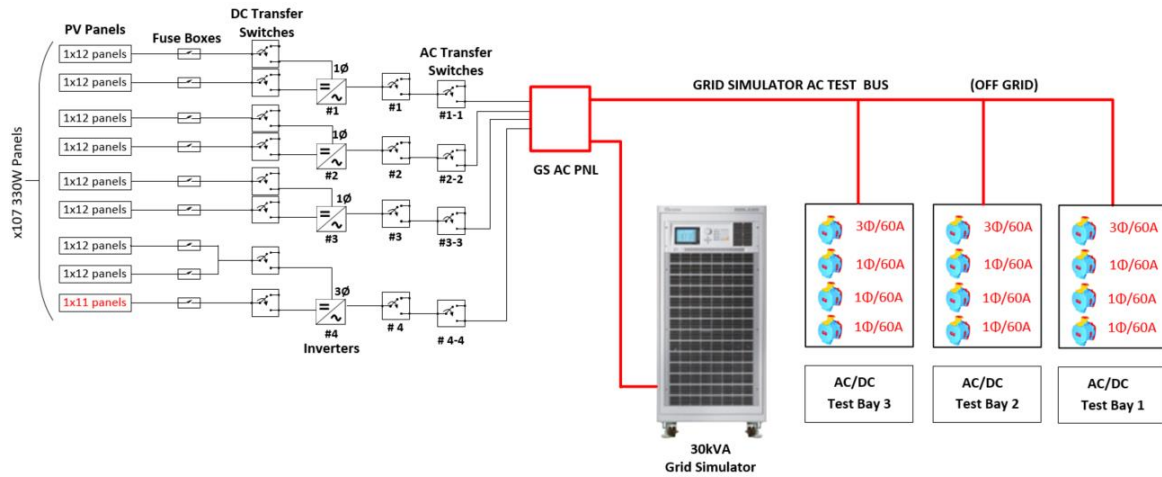


Figure 4.2.21. AC Test Bed – Grid Simulator (off-grid).

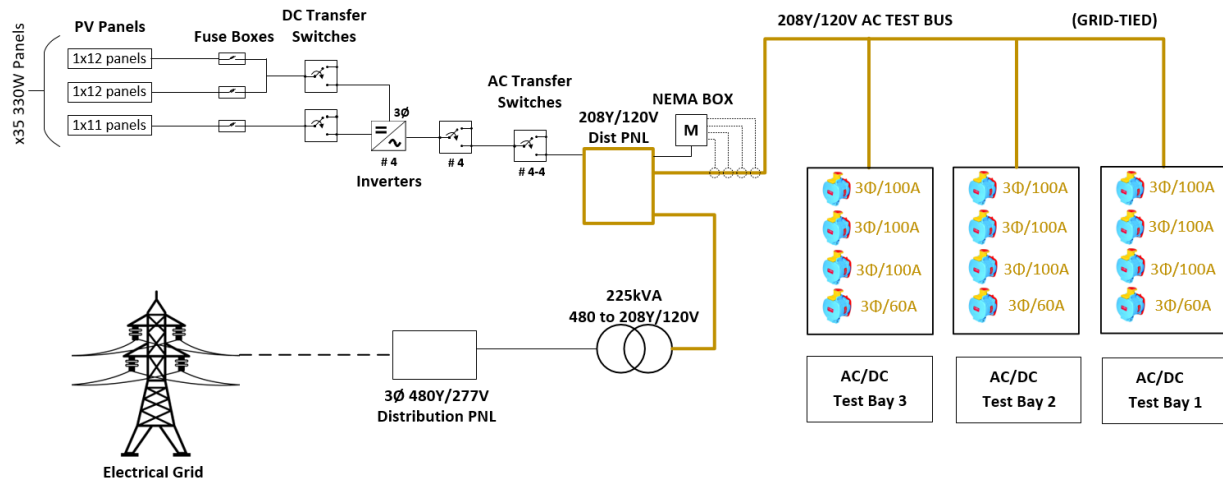


Figure 4.2.22. AC Test Bed – 208V (grid-tied).

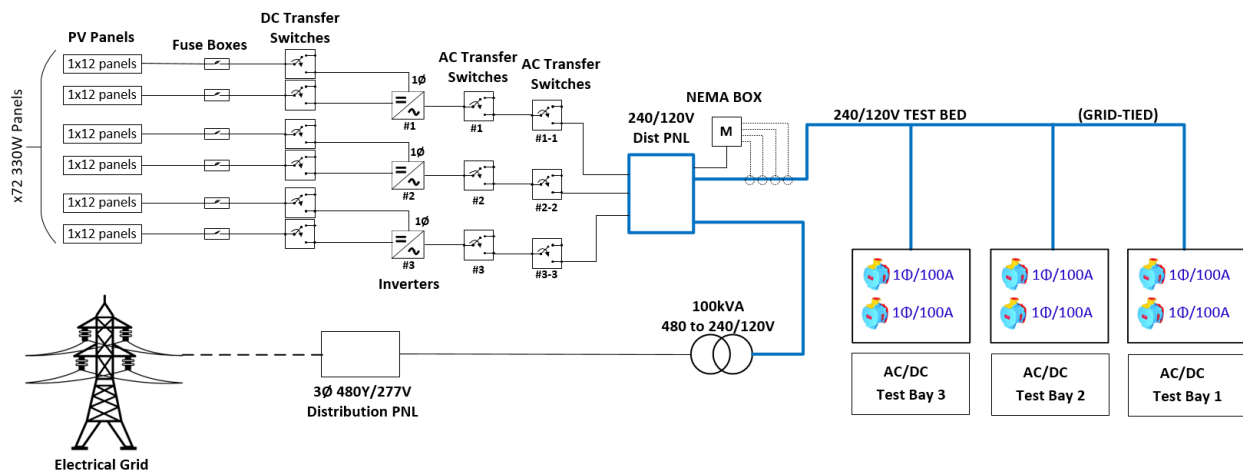


Figure 4.2.23. AC Test Bed – 240V (grid-tied).

HNEI acquired the APSL's laboratory equipment using previous APRISES funding. Prior APRISES funding also supported HNEI's collaboration with a local electrical engineering firm to create design drawings for the laboratory construction. Using current APRISES funding, HNEI hired a highly experienced electrical lab safety consultant who conducted a thorough safety design review of the design drawings. The consultant identified potential safety risks and proposed design changes for hazard mitigation, all of which have been integrated into the final construction drawings and ultimate lab space buildout.

The safety consultant also worked in close collaboration with HNEI to identify the following six safety operating procedures (SOPs):

- 1) Primary SOP – Lab Operations and Safe Work Rules;
- 2) Low Voltage Devices Testing;
- 3) AC & DC Test Beds and Test Benches Set Up and Operation;
- 4) Battery, Capacitor and Electrical Storage Device Use;
- 5) Parts, Equipment and Switchgear Cleaning Operations; and
- 6) Energy Isolation – Lockout Tagout (LOTO).

The SOPs will be completed after the lab construction and will be part of the operational safety program for the APSL.

In addition, the safety consultant reviewed and highly recommended the use of Meltric wire plug receptacles selected by HNEI for the test bays. These receptacles feature a disconnect push button and additional safety features such as arc-flash protection, UL listing, and compatibility with lock-out tag-out (LOTO) devices. They also have a specific design for different voltages and current levels to prevent incorrect connections. HNEI collaborated closely with Meltric to design and obtain the receptacle enclosures for the three AC/DC equipment test bays. The finished product of the Meltric receptacle enclosures is shown in Figure 4.2.24.



Figure 4.2.24. Receptacles Used on the AC/DC Test Bay.

A significant recommendation by the safety consultant that was incorporated into the lab design is the addition of an emergency stop (e-STOP) button. The e-STOP button is located near the laboratory room exit and serves as a last resort for instantly cutting power in case of emergencies.

Activating it instantly de-energizes all test bays by tripping the circuit breakers that feed them. Figure 4.2.25 below shows the circuit breakers controlled by the e-STOP button.

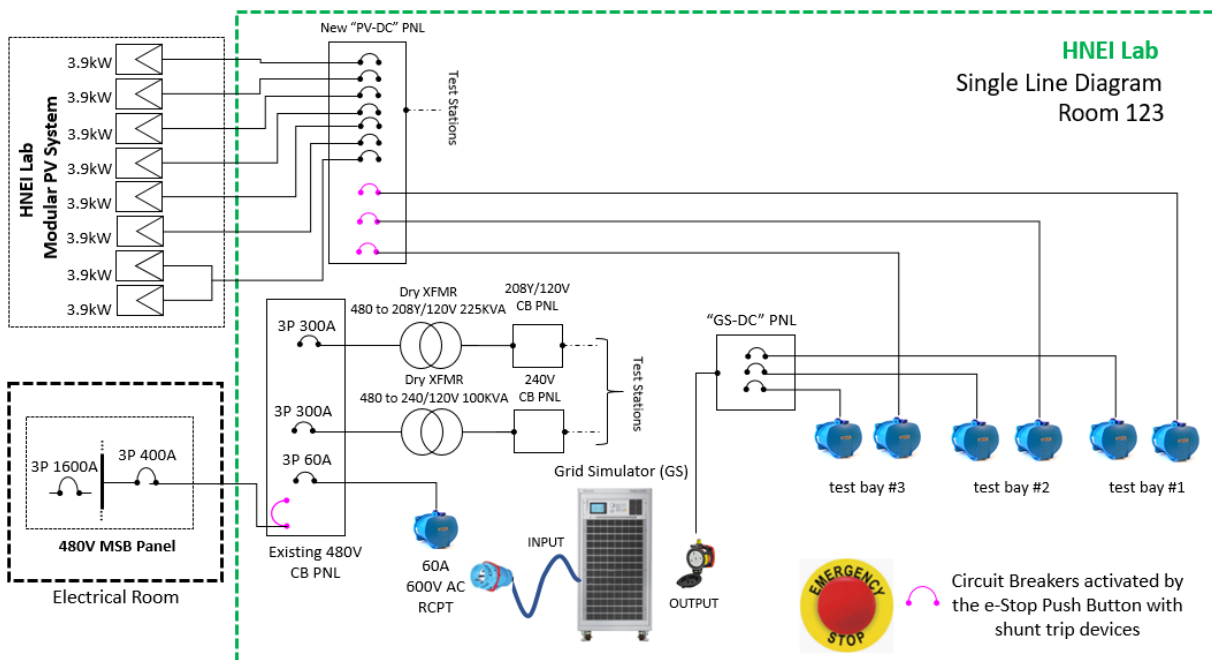


Figure 4.2.25. E-STOP Push Button-Controlled Circuit Breakers.

The electrical lab safety consultant reviewed the DC test bed design and proposed changes which have been incorporated into the lab design. One of the recommendations was to provide separate wiring for each DC bus instead of using the same receptacles for both. The revised DC test bed design is shown in Figure 4.2.26 below.

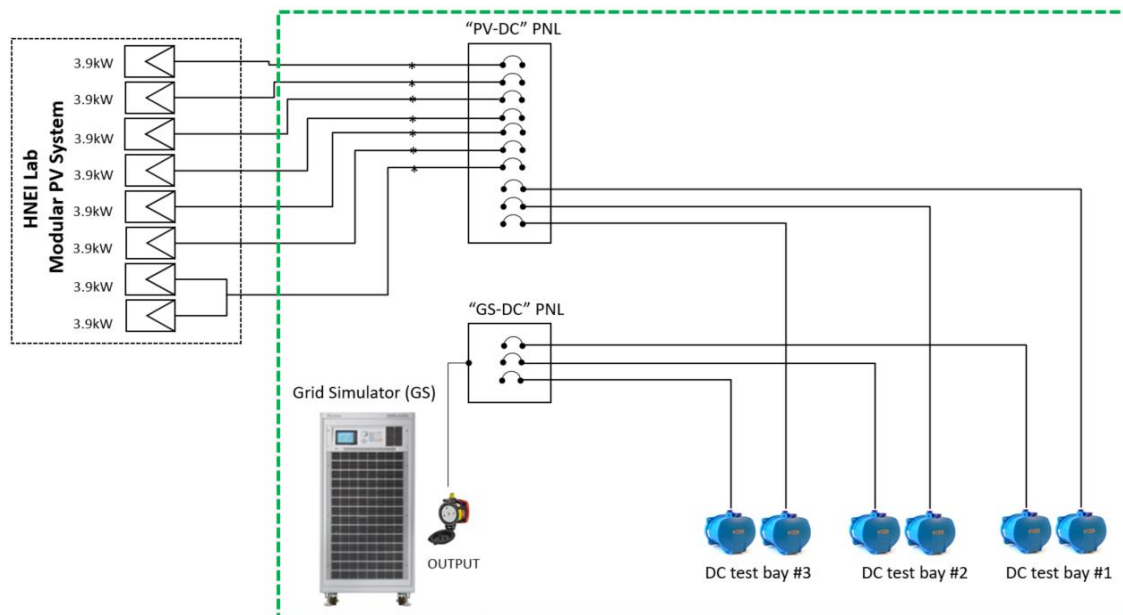


Figure 4.2.26. DC Test Bed (off-grid).

Upon completion of the design drawings, HNEI initiated the building permit application process with the Honolulu Department of Planning and Permitting (DPP). Due to well-publicized backlogs and delays in the building permit review process in Honolulu (many cases more than one year), HNEI elected to accelerate the process by retaining the services of a DPP approved Third-Party Reviewer (TPR) to review and approve the construction drawings on behalf of the DPP. Working in close collaboration with the engineering firm that designed APSL, HNEI addressed comments and questions from the TPR in the DPP permitting approval process. After several iterations that in some cases resulted in minor changes to the design drawings, the TPR approved the construction drawings. Soon after, DPP approved and issued the building permit for the APSL construction work.

Concurrent with the permitting process, HNEI issued an Invitation for Bids (IFB) package for the procurement of the electrical wiring, associated equipment and labor for the lab build-out. After a successful procurement process that received multiple valid bids from O‘ahu-based construction companies, HNEI awarded the construction contract to American Electric Company, LLC. At year-end 2022, construction of the APSL stood at 90% complete. HNEI will complete the lab construction using future APRISES funding in 2023.

Patents

1. Davies, K. L, Tran, T., Sepasi, S., & Roose, L. Distribution grid monitoring, United States patent 11,146,103, October 12, 2021.

Publications and Presentations

Peer-Reviewed Publications

1. Matthews, D. K. (2023). Determination of broadband atmospheric turbidity from global irradiance or photovoltaic power data using deep neural nets. *Energy and AI*, 14, 100252.

References

- [1] Davis, M., Martinez, S. L., Gaston, Z., Chopra, S., Connelly, C., Sahd, M., & Seiple, C. (2022). Wood Mackenzie/SEIA U.S. solar market insight®. [WWW Document] URL <https://seia.org/research-resources/solar-market-insight-report-2022-q3> (accessed 2.12.23).
- [2] Goody, R., & Yang, Y. (1995). Atmospheric radiation: Theoretical Basis. Second Ed. Oxford University Press, New York.
- [3] Gueymard, C. A., & Myers, D. R. (2008). Validation and Ranking Methodologies for Solar Radiation Models. In: Badescu, V. (eds) Modeling Solar Radiation at the Earth’s Surface. Springer, Berlin, Heidelberg. https://doi.org/10.1007/978-3-540-77455-6_20

- [4] Younes, S., & Muneer, T. (2007). Clear-sky classification procedures and models using a world-wide data-base. *Applied Energy*, 84, 623-645.
- [5] Gueymard, C. A. (2012). Temporal variability in direct and global irradiance at various time scales as affected by aerosols. *Solar Energy*, 86, 3544-3553.
- [6] Eltbaakh, Y., Ruslan, M., Alghoul, M., Othman, M., & Sopian, K. (2012). Issues concerning atmospheric turbidity indices. *Renew. Sust. Energ.*, 16(8), 6285-62941.
- [7] Bilbao, J., Román, R., & Miguel, A. (2014). Turbidity coefficients from normal direct irradiance in central Spain. *Atmos. Res.*, 143, 73-84.
- [8] Gueymard, C., & Vignola, F. (1998). Determination of atmospheric turbidity from the diffuse-beam broadband irradiance ratio. *Sol. Energy*, 63(3), 135-146.
- [9] Louche, A., & Peri, G. (2012). An analysis of linke turbidity factor. *Sol. Energy*, 37(6), 393-396.

TASK 5: ADVANCED HEAT EXCHANGER DEVELOPMENT

Under Task 5, HNEI subcontracted Makai Ocean Engineering to continue efforts to develop Thin Foil Heat Exchangers (TFHX) applicable to Ocean Thermal Energy Conversion (OTEC) and other U.S. Department of Defense (DOD) applications. Makai has been developing TFHX for use in seawater-refrigerant, air-water, and water-water applications at its test site located within the Natural Energy Lab of Hawai‘i Authority (NELHA) in Kailua-Kona, Hawai‘i. In the period between August 2021 and July 2022, Makai’s work focused on: 1) advancing TFHX design, 2) reducing TFHX fabrication time/cost, and 3) adding empirical performance data (thermal, hydraulic, and structural/mechanical) to the TFHX database.

A brief summary of progress made during this period follows. Additional detail is provided in Makai Ocean Engineering’s technical report to HNEI, which can be found at <https://www.hnei.hawaii.edu/publications/project-reports/apprises-17/>.

TFHX Design: Makai’s design work in this period expanded TFHX capabilities by using new materials and demonstrating a new “all-welded” sealing method. Makai developed a welding analysis tool to guide weld parameter selection based on material and foil properties. The tool was used while demonstrating the TFHX fabrication process was compatible with two new materials (nickel-based alloys and stainless steel). These new TFHX-compatible materials enable TFHX designs targeting higher pressure ratings, higher operating temperatures, and different channel sizes.

Makai also provided proof-of-concept demonstration of a new technique to seal a stack of TFHX plates (without gaskets). Makai was able demonstrate the individual successful welds, but was not

able to complete a sealed stack of plates. This was paused to focus on improving fabrication success rate.

TFHX Fabrication: Makai's on-going priority has been to improve fabrication success rate. In this period, Makai focused on implementing quality control processes. Makai started to develop automated real-time weld quality control methods using imaging and other monitoring tools to identify and repair weld defects after the welding step. Additionally, a High Speed Pressure Tester (HSPT) was commissioned to streamline leak checks on completed plates, reducing the time over previous methods by a factor of 10. These plate quality control processes also improve the overall success rate by identifying issues prior to heat exchanger assembly.

Test Results: Makai conducted geometric characterization, pressure capacity testing, durability testing, and thermos-hydraulic performance testing. With new materials and designs, Makai demonstrated TFHX pressure capacity can exceed 5,000 psig with a 0.25mm internal channel. With respect to durability test, preliminary results indicate a new processing step could lead to a 3X increase in cycles to failure.

Makai tested three ammonia-seawater (OTEC) TFHXs and three seawater-seawater (SWAC) TFHXs. Between the three FL units tested, larger ammonia-side channels and larger seawater channels were favored in condenser mode, whereas smaller ammonia channels and larger seawater channels were favored in evaporator mode. Larger internal channels were found to be better for SWAC applications.

Makai has learned that existing heating/cooling systems operate at conditions that accommodate the limitations of existing heat exchangers and those conditions are typically not favorable for a drop-in replacement TFHX. However, if operating conditions (i.e., flow rates, outlet temperatures) can be changed, TFHX designs can provide the required duty with overall savings in parasitic power.

TASK 6: ENERGY EFFICIENCY

Task 6 comprises additional data collection and analysis from on the University of Hawai'i at Mānoa FROG classrooms funded by the Office of Naval Research under previous APRISES funding. The COVID-19 pandemic reinforced the importance of indoor air quality (IAQ). This effort had three primary objectives that evaluate energy and indoor air quality with respect to natural and mechanical ventilation mechanisms:

1. Evaluate the energy consumption for operating heating, ventilation, and air conditioning (HVAC) systems "on-demand", that is, limiting the run time via a thermostat override

setting from a 1 hour run time, to 4 and 8 hour run times, as a substitute for a traditional set-point driven thermostat;

2. Determine the impact on CO₂ concentrations in the FROGs from HVAC operating hours, on-demand settings, natural ventilation and users' operation; and
3. Evaluate the impact of building users' post-pandemic awareness of natural ventilation mechanisms, as compared to pre-pandemic conditions.

The buildings investigated during this study were part of previous research focusing on the energy consumption of net zero energy, mixed mode classrooms [1-2]. University of Hawai'i at Mānoa (UHM) researchers monitored the two classrooms over six years, from 2017 through 2022 to evaluate the energy savings associated with a unique "on-demand" HVAC thermostat while monitoring CO₂ levels and other indoor variables. The analyses and conclusions in this report reflect 2022 interpretations of the data, focusing on the importance of fresh outside air in mitigating the spread of airborne vectors such as the coronavirus. An overview summary of this work is below and additional detail is provided in the technical report "*The Impact of an On-Demand Thermostat on Energy Consumption and Carbon Dioxide Levels in a Hawai'i Classroom*," which can be found at <https://www.hnei.hawaii.edu/publications/project-reports/apprises-17/>.

Several studies have investigated the energy performance [3], thermal comfort [4], as well as indoor air quality, ventilation, and occupant health symptoms [5] of school buildings, but the majority of the studies were located in temperate climates rather than tropical ones. Thus, this study compares how user choices with respect to engaging natural ventilation options, as well as the runtime settings of an on-demand thermostat (1 hour, 4 hour, and 8 hour) can affect energy consumption and CO₂ levels within the classrooms.

On-Demand Thermostat: The UHM FROGs were designed with a unique "on-demand" control that limits the operation of an HVAC system to be used upon user request, rather than automatically scheduled to run during normal operating hours regardless of whether the room is occupied or not. The on demand thermostat requires users to manually turn the air conditioning (AC) ON, which then allows the unit to run for a fixed number of hours then turn OFF automatically. When the interior comfort conditions require that it be restarted, the ON button is pressed once again to reenergize for another defined period. An on-demand control reduces the HVAC run time when there are no occupants in the buildings [2]. In classroom situations where there may be long intervals between the use of the room, the on-demand control results in significant energy savings because the AC will spend less time cooling an unoccupied space. A previous study showed an 84% reduction in energy consumption beyond a conventional thermostat scheduled for 7 am to 7 pm operation [2] when on a 1 hour demand override setting.

Impact of On-Demand HVAC Setup on Energy: HVAC systems are the most energy intensive system of the building and they determine the amount of outside fresh air that is introduced into the building. This section summarizes impact of the on-demand HVAC settings on energy

consumption when set for a 1 hour, a 4 hour, and an 8 hour runtime interval.

Figure 6.1 shows the HVAC power usage (kW) by on-demand settings over the investigated period. The data show the values over 24 hour periods of time and did not filter out the dates when the HVAC was down for repairs (see data for 2019 as an example). From 2017 to April 5, 2021, the on-demand setting was for 1 hour. In April 2021, with heightened pandemic awareness, the setting was then changed to an 8 hour runtime to maximize the amount of outside fresh air that was being introduced into the classroom. On December 12, 2021, since it was recognized that the classrooms were not being used in full 8 hour blocks, the setting was modified to a 4 hour setting runtime, where it remained for the balance of the data collection period.

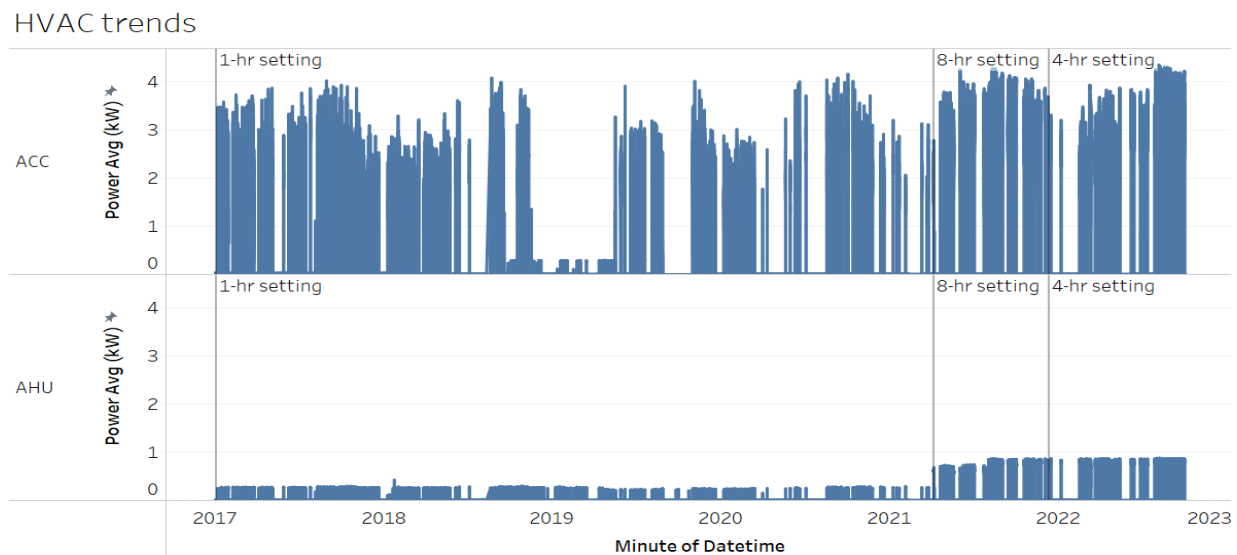


Figure 6.1. HVAC power demand (kW) and “on-demand” HVAC settings over the investigated period.

When the HVAC setting changed from 1 hour to 8 hours, the air handler fan speed was also increased to introduce more fresh air into the classrooms, increasing air handler power use. Figure 6.2 shows that the average power demand changed from 2.4 kW and 0.4 kW for the compressor and air handling units respectively to 3 kW and 0.70 to 0.75 kW after the fan speed was increased.

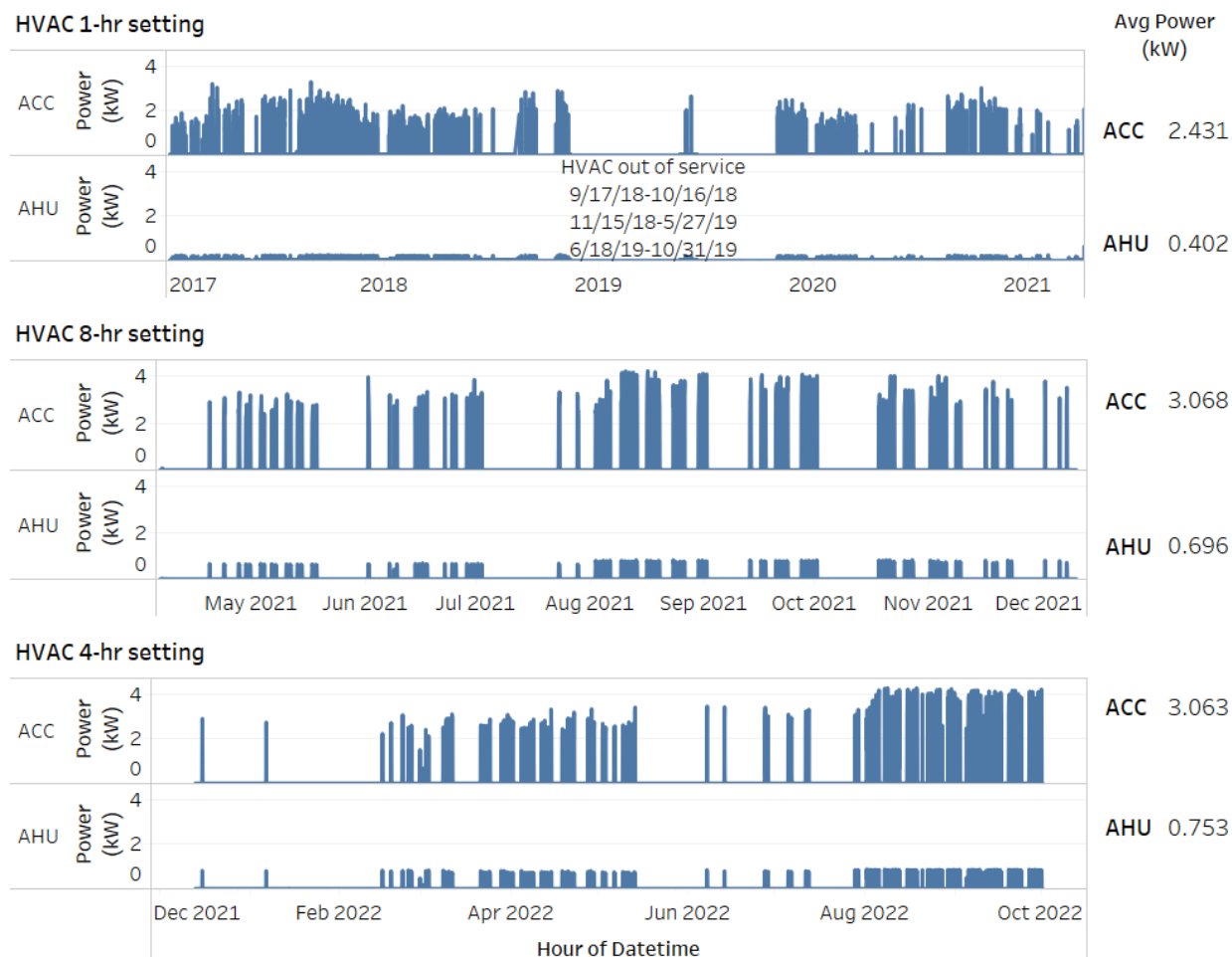


Figure 6.2. Power demand (kW) of HVAC for each “on-demand” setting (not filtered for schooldays; days the HVAC was not functioning have been filtered out).

Table 6.1 presents the percentage of time HVAC was used when the building was occupied and unoccupied. With the 1 hour on-demand setting, the HVAC system operated 28% of the time while occupied. When set at 4 hours, the HVAC operated 37% of the time and 54% for the 8 hour setting. The on-demand control is intended to reduce HVAC energy use when the classroom is unoccupied. The HVAC system ran only 9% of unoccupied hours at the 1 hour setting. With on-demand set to an 8 hour setting, the HVAC ran 41% of unoccupied hours because it was periodically activated late in the day, but continued to run after users left the building.

Table 6.1. Percentage of time HVAC on when occupied or unoccupied.

“On-demand” HVAC setting	Percent of Time HVAC on When Occupied	Percent of Time HVAC on When <u>Un</u>occupied
1 hour	28%	9%
4 hour	37%	30%
8 hour	54%	41%

While Table 6.1 shows HVAC operation during occupied and unoccupied hours, Table 6.2 below shows the energy consumption associated with the on-demand settings. The increase in daily energy consumption is greater due to both the longer operating hours, but also the increase in air handler fan speed.

Table 6.2. Average daily energy (kWh/day) consumption comparisons of the different HVAC settings evaluated for 7 am to 7 pm on schooldays. Dates when HVAC was not functioning or when classroom was not fully utilized during COVID-19 were filtered out.

“On-demand” HVAC setting	N=Sample Days	Average Daily Energy Consumption (kWh/day)	Average Power of HVAC when on	Air handler fan speed setting
1 hour	157	9.3	1.964	medium
4 hour	121	15.9	3.801	high
8 hour	78	18.9	4.003	high

Impact of On-Demand Settings and COVID-19 Pandemic Awareness on Indoor CO₂: This study also evaluated the impact of on-demand settings on classroom CO₂ concentration. The 1 hour setting was in place up to the beginning of the pandemic in Hawai‘i. During that period, indoor CO₂ levels periodically elevated beyond the ASHRAE recommendations [6] due to the intermittence of HVAC use, and that some users did not take advantage of the natural ventilation options. After instructor training was offered at the beginning of 2019, the CO₂ levels improved up to the end of 2019 when again values higher than 1,000 ppm were measured. CO₂ levels remained relatively low after the settings were modified to 8 and 4 hours, largely because ventilation awareness was likely increased due to the recommendations made by the CDC and the State for fighting the COVID-19 pandemic. However, a trend of increasing CO₂ appeared during the last three months of the 2022 investigation period. The August and September 2022 data showed that CO₂ values increased, although well within an acceptable range, as clearly shown in Figure 6.3. This was due to a new fall-quarter cohort of instructors using the classrooms for the first time, who had not yet been trained in the optimal use of natural ventilation in the classroom.

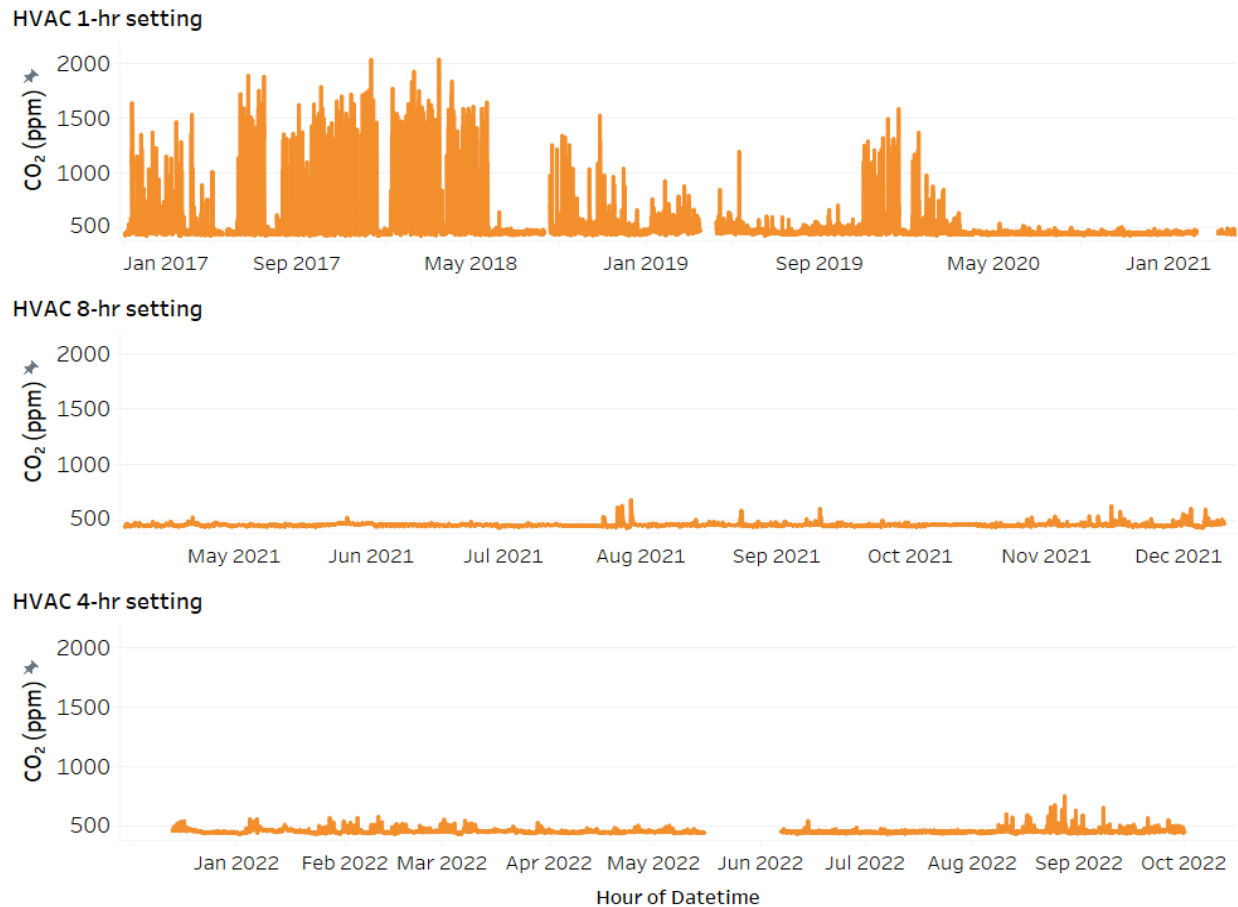


Figure 6.3. CO₂ values by on-demand settings.

Summary and Conclusions: As a response to environmental and indoor public health challenges, mixed-mode buildings provide an opportunity for users in tropical, cooling-only climates to control their indoor environment at a lower energy cost. On one hand, mixed-mode allows users to choose to open windows, doors and clerestories to increase ventilation rates. Conversely, mixed-mode can provide a false sense of well-being when the user feels that the choice between natural ventilation and air-conditioning is a binary decision and that either one will provide adequate ventilation. In many cases, because air-conditioning may not provide adequate fresh air, CO₂ concentrations are likely to increase without the user recognizing it.

With the 1 hour on-demand setting, the HVAC system was energized 28% of the time when the building was occupied. When set at 4 hours, the HVAC was on 37% of the time; and 54% for the 8-hr setting. Energy savings is realized when the HVAC system does not waste energy by running when the building is unoccupied. With the 1 hour setting, the HVAC system was energized only 9% of time when unoccupied. With on-demand set to an 8 hour setting, the HVAC ran 41% of unoccupied hours. With the 4 hour setting, the HVAC ran 30% of unoccupied hours.

The 1 hour on-demand setting was in place up to the beginning of the pandemic in Hawai‘i. Because of the heightened awareness of the need for the circulation of fresh air indoors, HVAC

runtime and fan speed was increased to facilitate the introduction of fresh outside air while the HVAC system was energized. After the return to classroom operation following a 17-month closure due to COVID-19, the increased awareness changed the behavior of experienced classroom users who had been using the room for several quarters. Not only did they take advantage of natural ventilation features such as operable windows, they also defied the conventional practice of *closing* windows while the HVAC was running. By running in *concurrent mode*, they opened windows while running the HVAC, and CO₂ levels remained low after returning to school following the pandemic closures. New users of the classroom were not familiar with the natural ventilation features of the classroom, and frequently ran the HVAC system without additional fresh air. While not rising to dangerous levels, CO₂ did rise with a new cohort of teachers in Fall 2022.

A balance exists between HVAC energy use and indoor air quality (CO₂ concentration) that relies on natural ventilation (window operation) and HVAC use to maintain comfort as well as a healthy indoor environment. During early FROG operation in 2017-2018, prior to instructor training, the HVAC was used regularly and CO₂ levels were among the highest observed during the entire study, with daily averages regularly exceeding 1,000 ppm. Natural ventilation features of the classrooms were not initially being used because traditionally windows are closed when HVAC is operating. After user training in 2018, which informed the instructors how to appropriately use natural ventilation rather than mechanical cooling, the CO₂ levels dropped significantly. (It should be noted here, that window sensors were installed Q4 2018-2019 in order to monitor window position. Prior to this, natural ventilation was only inferred using the observed levels of CO₂. Data shows that from Q1 2019-2020, natural ventilation became more embraced by the users, and windows were opened more routinely. Prior to Q1 2021, the windows had been generally closed when the HVAC system was on.

Further detail of this study is available in the technical report "*The Impact of an On-Demand Thermostat on Energy Consumption and Carbon Dioxide Levels in a Hawai'i Classroom*" available on the HNEI website at <https://www.hnei.hawaii.edu/publications/project-reports/aprises-17/>.

References

- [1] Maskrey, A. J., Cerri, S., Peppard, E., Miller, M., & Uddenberg, S. (2016, August 21-26). *Positively net zero: case study of performance simulation and hitting the targets*. Proceedings of the American Council for an Energy-Efficient Economy (ACEEE) Summer Study Conference, Pacific Grove, CA, United States.
- [2] Maskrey, A. J., Cerri, S., & Peppard, E. (2018, August 12-17). *Second generation ZNE: inheriting the good genes*. Proceedings of the American Council for an Energy-

Efficient Economy (ACEEE) Summer Study Conference, Pacific Grove, CA, United States.

- [3] Dias Pereira, L., Raimondo, D., Corngati, S. P., & Gameiro da Silva, M. (2014). Energy consumption in schools – a review paper. *Renewable and Sustainable Energy Reviews*, 40, 911-922. <https://doi.org/10.1016/j.rser.2014.08.010>
- [4] Zomorodian, Z. S., Tahsildoost, M., & Hafezi, M. (2016). Thermal comfort in educational buildings: A review article. *Renewable and Sustainable Energy Reviews*, 59, 895-906. <https://doi.org/10.1016/j.rser.2016.01.033>.
- [5] Daisey, J. M., Angell, W. J., & Apte, M. G. (2003). Indoor air quality, ventilation and health symptoms in schools: An analysis of existing information. *Indoor Air*, 13(1), 53–64. <https://doi.org/10.1034/j.1600-0668.2003.00153.x>
- [6] ASHRAE. 2022. ASHRAE position document on indoor carbon dioxide. Retrieved January 8, 2023, from https://www.ashrae.org/file%20library/about/position%20documents/pd_indoorcarbondioxide_2022.pdf.